POLITECNICO DI TORINO

Collegio di Ingegneria Biomedica

Corso di Laurea Magistrale in Ingegneria Biomedica

-Indirizzo Biomeccanica-

Tesi di Laurea Magistrale

Exploring the impact of through-plane velocity in Fontan hemodynamics using computational fluid dynamics

Relatore

Prof. Diego Gallo

Correlatori

Prof. Umberto Morbiducci

Dott. Maurizio Lodi Rizzini

Ing. Paola Tasso

Candidato

Lucia Magaton

Anno Accademico 2018/2019

Conoscere è il primo passo verso una soluzione

[Vittorio Arrigoni]

Summary

ABSTRACT

Fontan is the most common procedure for single ventricle heart disease patients: it is a complex cardiothoracic surgery composed by three steps that must be carried out in the first years of life of children suffering from this congenital malformation. However, it is a palliative surgery which does not ensure a physiological circulation. Its success allows the patient to survive (especially in the first years of life), but its low efficiency can have bad consequences on future life. Because of its unique flow distribution, Fontan-treated patients are interesting cases to study from a haemodynamic point of view.

In particular, computational models of Fontan procedure are powerful tools because they can provide an insight into complex flow phenomena, helpful to understand and improve this technique which is still imperfect.

This computational study aims to provide an insight into total cavopulmonary connection. A patient-specific model was studied thanks to software like VMTK and SimVascular. Then, 5 different velocity profiles were imposed as boundary conditions at the inlets. The objective is to understand if the presence of secondary flow in orthogonal plane respect to the vessel longitudinal axis could improve Fontan efficiency, without worsen the atherogenic or thrombogenic situation. To study the different behaviours of these velocity profiles, 5 unsteady simulations were performed on SimVascular for two cardiac cycles, hypothesized with the duration of 1 second each.

Different metrics were studied to understand if secondary flow at boundaries have an impact on haemodynamics. Wall shear stress-based descriptors allow to understand if the conditions that cause generation and proliferation of atherosclerotic plaques, thrombosis or hyperplasia are present at luminal surface. Bulk-flow descriptors give us information about flow distribution, visualizing helical patterns and quantifying helical flow. At last, the analysis focused on energy dissipation metrics, allowing to study the efficiency of the patient-specific Fontan connection.

Interesting results come from these data: the presence of an in-plane velocity component at the inlets seems to decrease energy dissipation, increasing the cavo-pulmonary connection efficiency. Moreover, secondary flows have good effects even from an atherogenic point of view.

Univentricular heart is a mortal defect without surgical treatment. Fontan is a helpful but still imperfect procedure. Surely, computational fluid dynamic is a useful tool to improve its efficiency, getting close as much as possible to the physiological circulation. This topic needs to be studied much more than in the past because the improvement is possible, and the technology can do it.

This study is an attempt to help this imperfect surgery to improve: maybe, in future, the procedure will be modified imposing at the venae cavae flows some in-plane velocity patterns, with the aim of increasing the non-physiological connection efficiency and reducing the long terms problem associated with energy dissipation in heamodynamics.

Chapter 1 – Introduction

The cardiovascular system has the great function to feed all the body organs and to collect from them the waste substances (in particular CO_2), that it has to bring to the lungs. Any type of disease that involve heart or blood vessels is extremely dangerous: the Single Ventricle Heart Disease (SVHD) or univentricular heart is one of them, so it requires a lot of attention.

In this chapter, firstly a general overview of heart and its functions is reported; then, we deal with the pathological situation of univentricular heart and the surgical procedure that it requires to allow the patients survival. Finally, the effects of Fontan surgery in haemodynamic and in children daily life.

1.1 - ANATOMY AND PHYSIOLOGY

Human heart is a hollow muscle organ whose function is pumping oxygenated blood in all the body, receiving and allow the removal of carbon dioxide and other cellular waste sending them to the lungs (United Medical Education, 2012-2013).

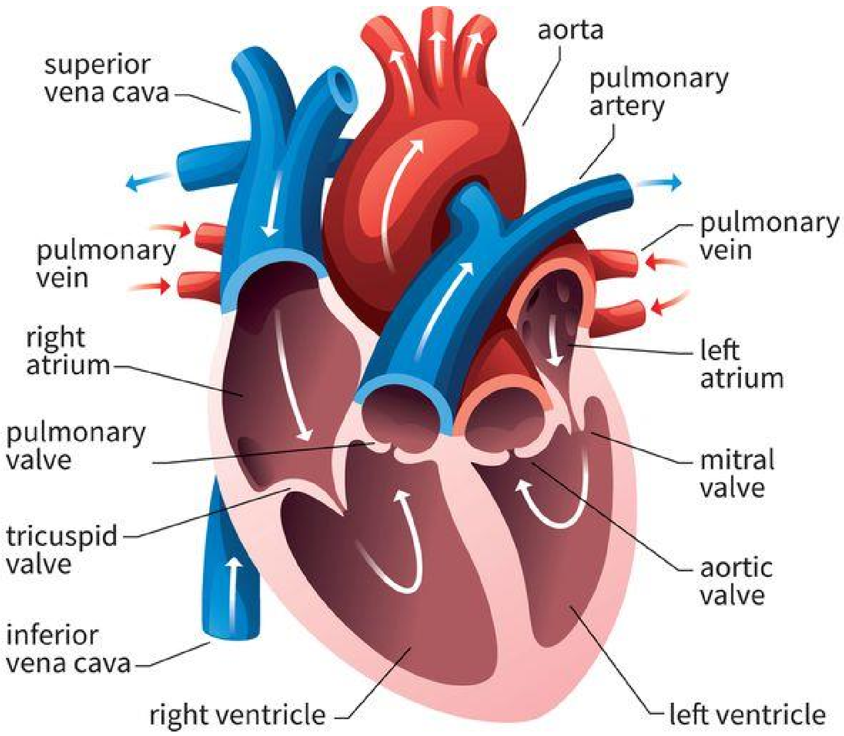

Figure 1 - Human heart (Scoville, 2019)

Anatomically, human heart is composed by 4 chambers with different dimensions and 4 valves, as it is possible to see in Figure 1: two atria and two ventricles, separated by interatrial and interventricular septum. Atria collect blood and then feed the ventricles, while ventricles act as true muscle pumps that support circulation (Girola, 2003).

An anatomical and functional separation concerns right and left side of the heart: both the sections are composed by an atrium and a ventricle. The right-side deals with deoxygenated blood and the two relative chambers are separated by the atrioventricular or tricuspid valve, while the semi-lunar or pulmonary valve separates the right ventricle from the pulmonary arteries in the pulmonary circuit (United Medical Education, 2012). Right atrium receives blood from above thanks to the superior vena cava (SVC), and from the bottom thanks to the inferior vena cava: both venae cavae collect deoxygenated blood from all the body and bring it to the right atrium (Girola, 2003). Blood passes to right ventricle with the contraction of right atrium and then it is pumped to the pulmonary arteries (the unique arteries that transport venous blood), in the pulmonary circulation: pulmonary arteries (PAs) bring venous blood to the lungs where it is re-oxygenated.

The whole circulatory system is reported in Figure 2.

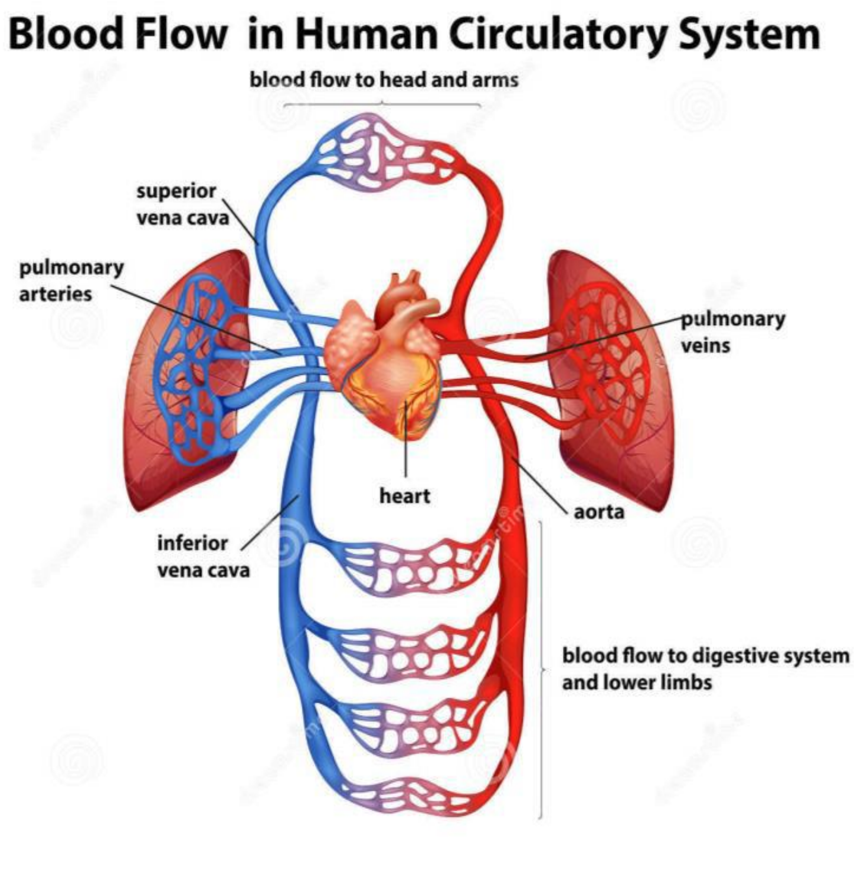

Figure 2 - Blood flow in circulatory system (Giunta, 2016)

Left side of the heart is composed by left atrium and left ventricle which are separated by the atrioventricular valve called mitral valve. Another valve is present, and it separates the left ventricle from the systemic circuit: it is the aortic valve. The left side deals with oxygenated blood because it receives in the atrium the pulmonary veins after the re-oxygenation; then, blood goes into the left ventricle where it is pumped in the systemic circulation through aorta (United Medical Education, 2012).

Heart wall is composed by three layers: the inner is the endocardium, which goes in direct contact with blood cells; the middle layer is the myocardium and it is composed by cardiac muscle that allows the contraction; the outer is the epicardium and it makes up the inner wall of pericardium (United Medical Education, 2012). Pericardium has a bilayer composition and it protects, lubricates and supports the outside of the heart.

The cardiac cycle is composed by the alternation of the two main state under which each chamber passes: systole and diastole. Systole is the contraction that pull the blood out of the involved chamber; diastole is the relaxing moment through which the chamber is filled with received blood (Girola, 2003; Giunta, 2016). When blood arriving from the venae cavae enters in the heart (right atrium), all the chambers are in diastolic phase: at the same time, the oxygenated blood come from lungs to the left atrium. After atria contraction, blood flows in the ventricles: the increasing of ventricular volume at the end of the diastolic phase causes the AV valves closing and the beginning of systolic phase. At this point, all the valves are closed, but when the ventricular pressure exceeds the aortic one, aortic and semi-lunar valves open and the ventricles contract allowing the blood to go in aorta and in pulmonary arteries respectively. Then, ventricular pressures decrease and the semi-lunar and aortic valves close: in the meantime, atria are collecting new blood from veins and the next cycle is starting (Girola, 2003).

1.2 - PATHOLOGICAL CONDITION: Single Ventricle Heart Disease (SVHD)

Univentricular heart is a congenital heart disease with an incidence of about 1.5-2% in new-born with cardiac problems (Bravo-valenzuela, Peixoto, & Araujo Júnior, 2018). This pathological condition is present when there is only a ventricular chamber (the left one in 80% of cases (Gatzoulis, Swan, Therrien, & Pantely, 2007)) that is connected to both atria with the AV valves and this ventricle supplies both systemic and pulmonary circles. The other ventricle is present in a rudimental form, it suffers from hypoplasia: generally, it is connected to the principal ventricle through an interventricular defect, but it can't be used surgically to correct this malformation (Calabrò, Pacileo, & Russo, 2012).

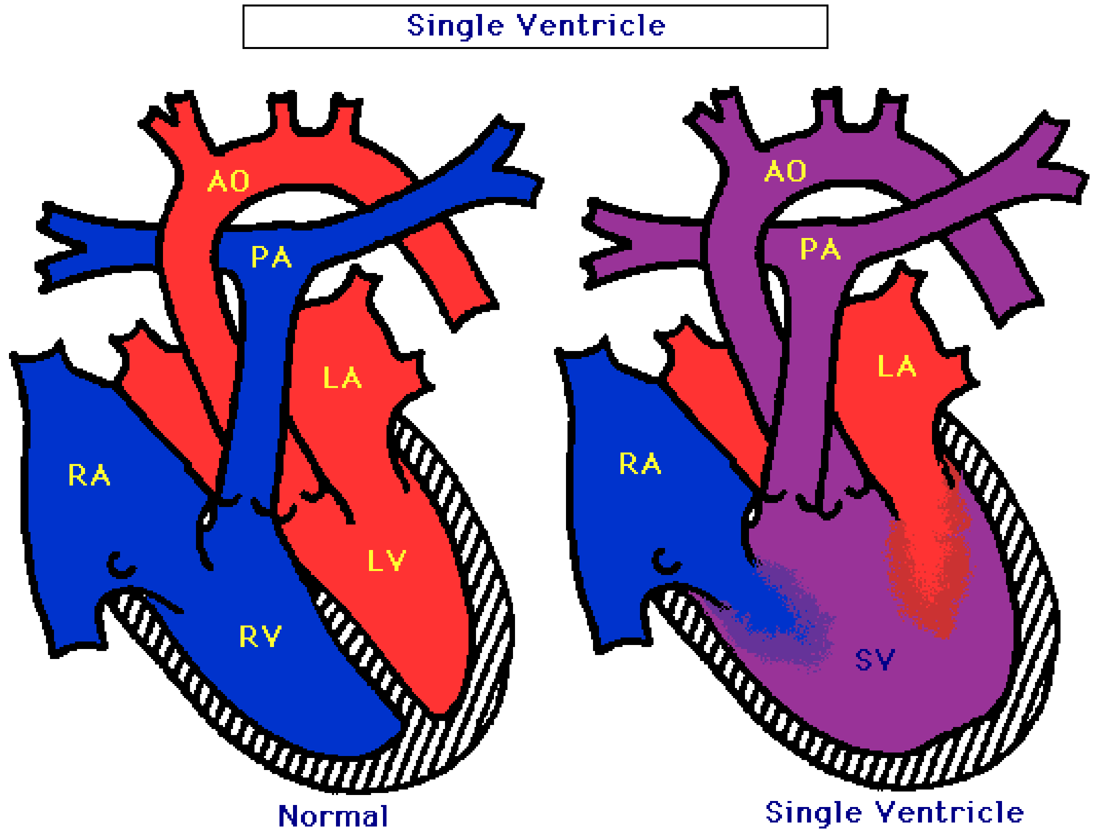

Figure 3 - Comparison between health and univentricular hearts (Lily's heart warriors, n.d.)

The pathological cases that are included in this congenital heart disease class are double inlet ventricle and absent connection, due to absence of one of the AV valves; however, also the "functional" univentricular heart are considered, such as pulmonary/aortic atresia and hypoplastic left-heart syndrome (D'Andrea, 2013; Frescura & Thiene, 2014): they have two normal chambers anatomically, but functionally they can use only one of them.

Diagnosis can be carried out by cardiac echography in the prenatal era where it is possible to see the absence of interventricular septum, the hypoplastic ventricle or the two AV valves that open into a unique chamber (Bravo-valenzuela et al., 2018; D'Andrea, 2013; Gatzoulis et al., 2007). However, before birth, this condition has no relevant haemodynamic effect on fetus (Bravo-valenzuela et al., 2018).

After birth, the baby is cyanotic because of the oxygenated and deoxygenated blood mixing and the single ventricle pressure and volumetric overload (D'Andrea, 2013): the cyanosis can be media or severe, depending on pulmonary flows (Gatzoulis et al., 2007).

In patient with univentricular heart the presence of two parallel circuits sustained by the single ventricular chamber shows negative long-time effects, like chronic volumetric overload that can turn to a progressive heart failure, or like chronic cyanosis with its consequent systemic risks (D'Andrea, 2013). For these reasons, the surgical procedure is necessary with the objective of decreasing the ventricular volumetric overload and increasing blood saturation.

1.3 - FONTAN PROCEDURE

Univentricular heart condition without surgical treatment brings to death in 95% of cases (Giunta, 2016); for this reason, Fontan surgery is the usual procedure for this type of patients. The surgical procedure in SVHD is a palliative one; in fact, both normal anatomy and physiology aren't respected, but an "in series" haemodynamic system is created (D'Andrea, 2013). The idea of bypassing right ventricle appears the first time in 1971, form an intuition of Fontan and Baudet (Fontan F, 1971; Giunta, 2016): this is a first attempt of separating oxygenated and deoxygenated blood with a non-anatomical connection that involved venae cavae, right atrium and pulmonary arteries; in this way, the ventricle receive blood only from pulmonary veins (Fontan F, 1971).

Nowadays, the so-called Fontan procedure is a series of planned (in different period of time) surgical interventions in order to gradually separate systemic and pulmonary circulations, gradually decrease the volumetric overload on the ventricle, allowing at the end a gradual ventricular remodelling (D'Andrea, 2013). The three main surgery required to obtain a total right ventricle bypass are Norwood, Glenn and Fontan procedures.

1.3.1 - *FIRST PALLIATIVE STEP: NORWOOD PROCEDURE*

The main goal for doctors in the patient first days of life is to find a balance between pulmonary and systemic flows: if pulmonary flow is higher than the systemic one, there is a congestion that requires a bandaging of pulmonary arteries; if systemic flow overcomes the pulmonary one, there is cyanosis and the surgical procedure needed is a systemic-pulmonary shunt (D'Andrea, 2013). This last case is the Norwood procedure and it is an important step for improving circulation after birth.

The main surgical steps are: firstly, a pulmonary artery resection is made and its distal edge is closed with a patch; then, the systemic-pulmonary shunt (between subclavian and right pulmonary arteries) is created which allow the pulmonary flow; finally, the proximal pulmonary artery is connected to the aortic arch. On the basis of patient pathology, this process can change.

An example of hearth after Norwood stage is reported in Figure 4, where a hypoplastic left heart syndrome (HLHS) is represented.

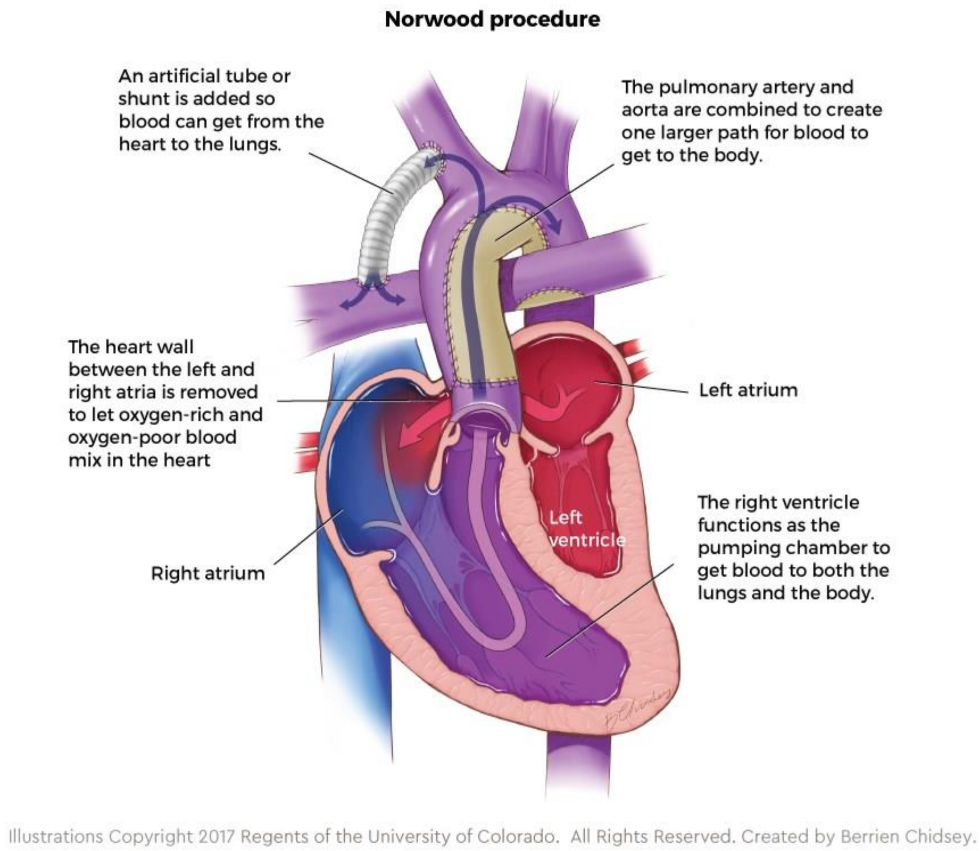

Figure 4 - Norwood procedure in HLHS case (Children's Hospital Colorado, n.d.)

However, Norwood procedure isn't enough to guarantee a good haemodynamic condition, mainly because there is still present mixing of oxygenated and deoxygenated blood. So, next steps are necessary.

1.3.2 - *SECOND PALLIATIVE STEP: BIDIRECTIONAL GLENN PROCEDURE*

The Glenn procedure, also called bidirectional Glenn or hemi-Fontan procedure, is done at four/six month of age because it is important to wait the pulmonary resistances decreasing and to avoid ventricular overload for an excessive long time (Shah, Rychik, Fogel, Murphy, & Jacobs, 1997). Its goal is to create a partial separation between the two circulations, in order to reduce the volumetric overload of the single ventricle, creating a direct connection between superior vena cava and pulmonary circuit (D'Andrea, 2013). To do this, firstly, the previous created shunt is disconnected, then a bidirectional cavo-pulmonary anastomosis is surgically created; in fact, systemic venous flow can reach pulmonary circuit even without a ventricular output, while heart works better.

At the end of this procedure, blood arriving from superior vena cava (SVC) goes into the pulmonary circuit bypassing the heart, while blood arriving from inferior vena cava (IVC) flows into arterial systemic blood. In Figure 5 is shown a heart after Glenn procedure (with HLHS).

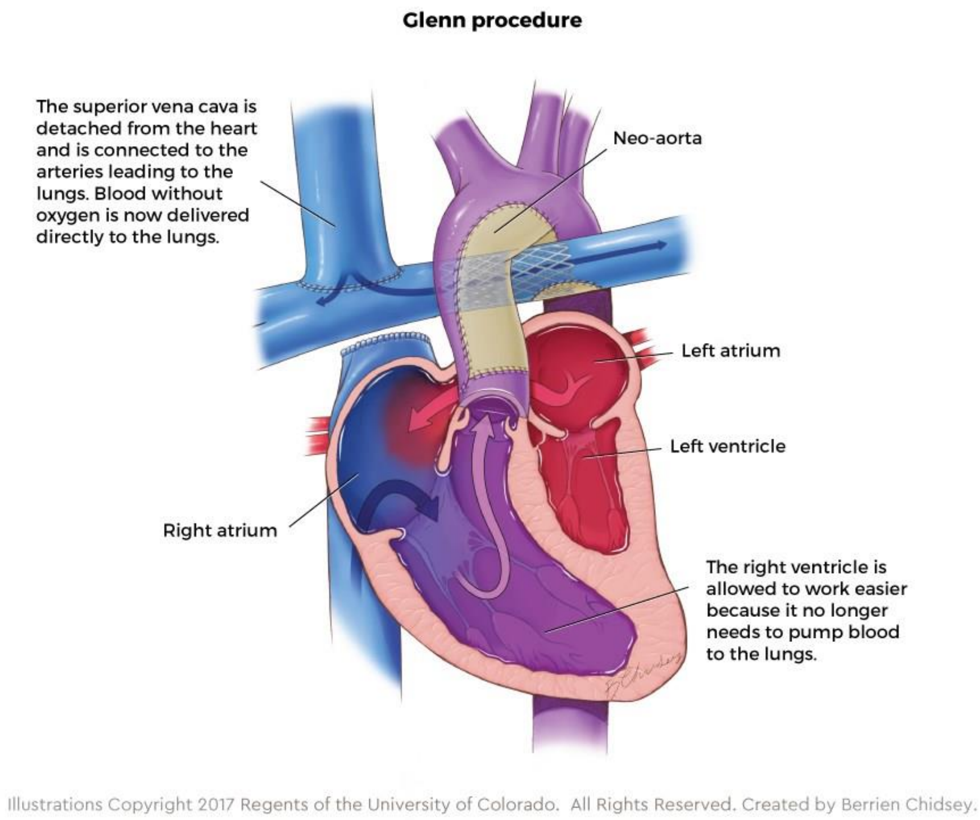

Figure 5 - Glenn procedure in HLHS heart (Children's Hospital Colorado, n.d.)

After Glenn procedure, the patient is more stable, with minor risks than after the Norwood surgery (Children's Hospital Colorado, n.d.).

However, there are different problems that can develop over time, if the patient doesn't undergo to the next palliative step. These problems are the comparison of (pulmonary or systemic) fistulas, an asymmetric distribution of pulmonary flow, decreasing of central pulmonary arteries growth and progressive de-saturation (D'Andrea, 2013).

1.3.3 - *THIRD PALLIATIVE STEP: FONTAN PROCEDURE*

The last palliative step is made after the patient is 18-month-old. Only after Fontan procedure the two circulations are separated and there is no more blood mixing; the load on the ventricle is normalized and arterial saturation is near to normal value. With Fontan operation the whole contractile force is exerted by the ventricle, while systemic and pulmonary resistances are in series (D'Andrea, 2013).

Through the total cavo-pulmonary anastomosis, the inferior vena cava (IVC) too is connected to the pulmonary arteries with the creation of a channel through or just outside the heart to direct blood into pulmonary circuit: in this way, deoxygenated blood flows passively to the lungs (University of California San Francisco, 2018), while the heart receives only oxygenated blood by the pulmonary veins and pumps it into the aorta (as Figure 6 shows).

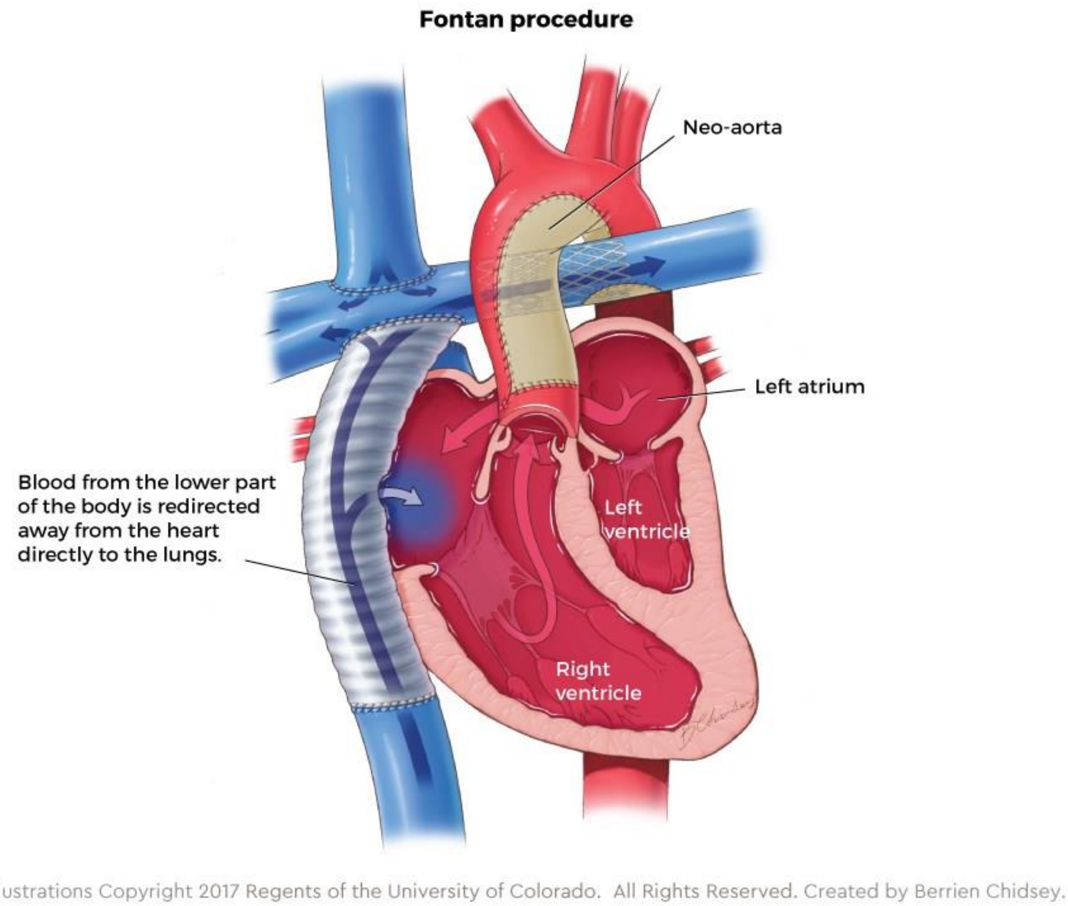

Figure 6 - Fontan procedure in HLHS heart (Children's Hospital Colorado, n.d.)

The total cavo-pulmonary connection (TCPC) in its years of life has been made with different execution methodologies. The first (in time) classic Fontan surgery consisted of a direct anastomosis between right pulmonary artery and right atrium (Figure 7 (a)): the right atrium was included in order to exploit even a minimal pumping function (Fontan F, 1971). However, this intervention was overcome because it had different complications caused by a progressive atrial expansion; next purpose is the intracardiac or intra-atrial TCPC (Kuroczynski, Senft, Elsaesser, & Kampmann, 2014) which consists of the construction of an intra-atrial tunnel between IVC and SVC, with this one anastomosed with right pulmonary artery (Figure 7 (b)). Today, another type of Fontan surgery is used (Figure 7 (c)), which has decrease the post-operative mortality rate: an extracardiac channel is anastomosed between IVC and pulmonary arteries (Lardo, Webber, Friehs, Del Nido, & Cape, 1999); the different surgical steps are shown in Figure 8. The main advantages are that suture points and the whole intervention are made outside the heart, decreasing arrhythmic problems, and there is no more possible thrombogenic material inside the atrium; moreover the extracardiac channel has a fixed calibre, that helps to reduce power losses with its geometrical regularity, increasing connection haemodynamic efficiency. For these reasons, nowadays the total extracardiac cavo-pulmonary connection (TECPC) is the most used technique for Fontan procedure (Figure 8).

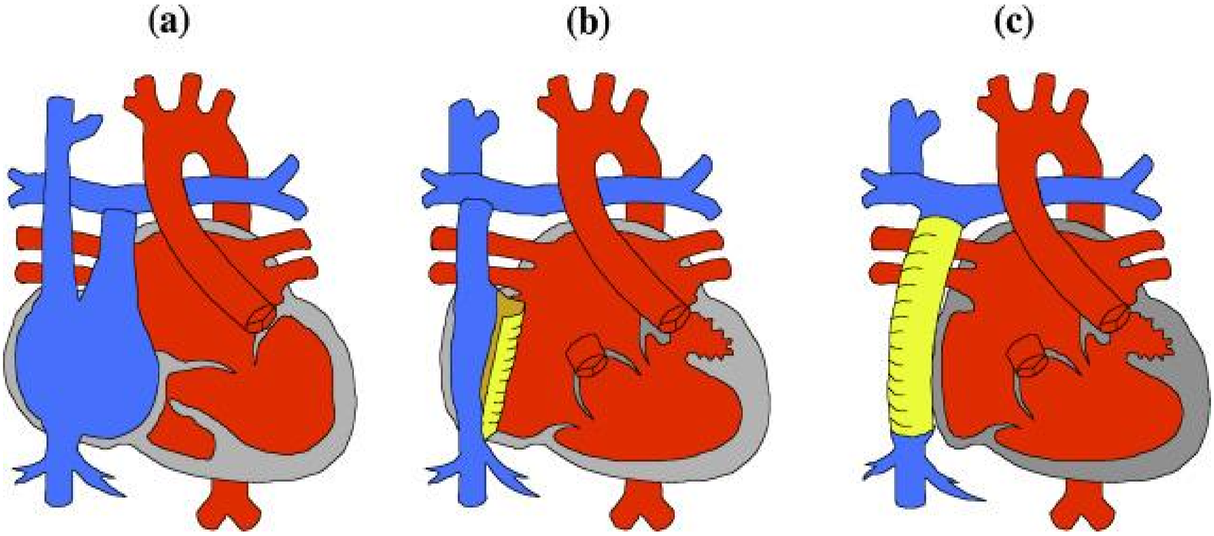

Figure 7 - Different methodologies of Fontan intervention: (a) classical Fontan; (b) intra-cardiac Fontan; (c) extracardiac Fontan (Ohuchi, 2016)

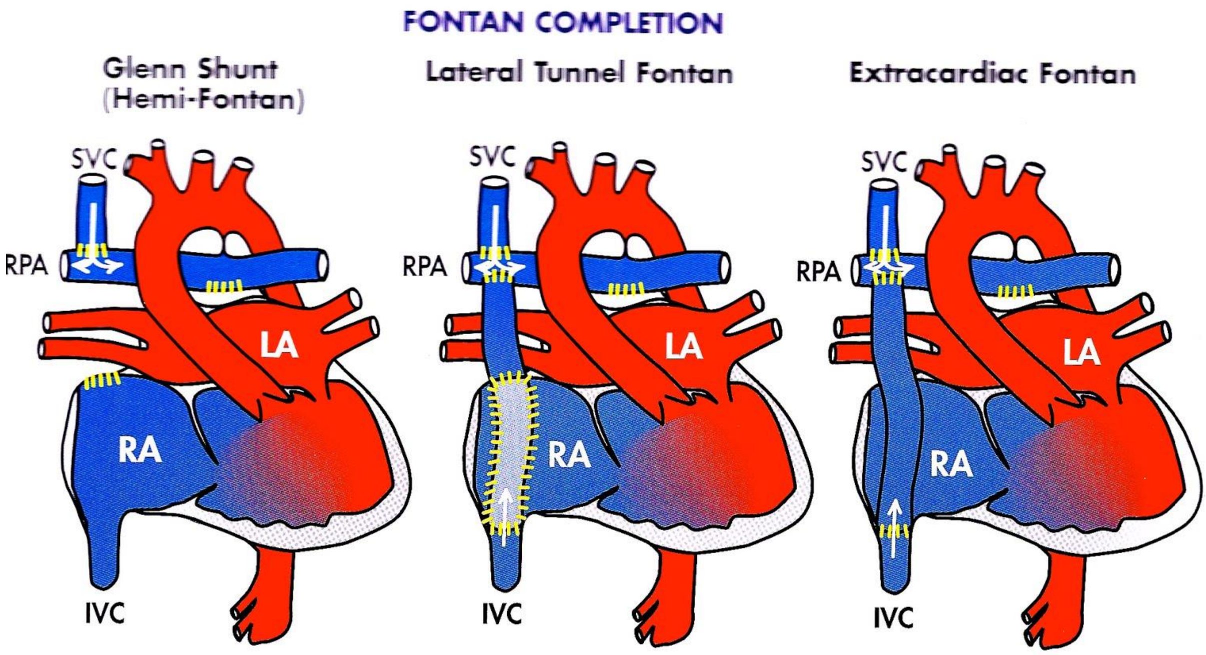

Figure 8 - Main surgical steps of TECPC

1.3.4 - *PATIENT-SPECIFIC MODEL*

Our patient-specific model is an example of TECPC: its orientation near the heart is shown in Figure 9. Here it is possible to see how the different vessels were connected during the surgical intervention. Starting from the top SVC is present, the vena cava that collect all the deoxygenated blood from the head and the superior part of the body; then, on the right it is possible to see the LPA (left pulmonary artery), a vessel that brings to the lungs the blood coming from the venae cavae. On the left it is possible to see the RPAs, the right pulmonary arteries that in this type of connection are two: they have the same job of LPA, allowing the deoxygenated blood to reach the lungs. On the bottom of the model we find IVC, the inferior vena cava which brings the deoxygenated blood coming from the whole inferior part of the body.

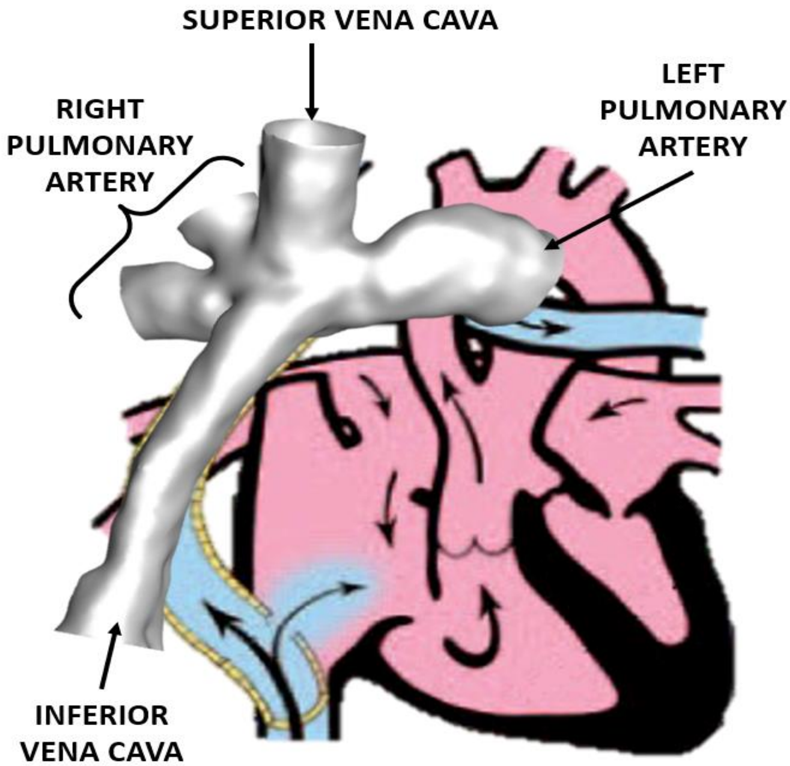

Figure 9 - Model's position and orientation

From a haemodynamic point of view, SVC and IVC are considered the inlets and LPA and RPAs the outlets of the model. In this way the two flows coming from the rest of the body arrive in this "crossroads" instead of the right atrium, while the PAs start form the centre of the model instead of the right ventricle and go to the lungs. This study is focused on the vessels' connection because it is interesting to study how the fluxes coming from the venae cavae mix and collide and divide their flow into the three PAs and which can be the energetic consequences of this non-physiological connection.

1.4 - HEMODYNAMIC EFFECTS AFTER SURGICAL PROCEDURE

The success of Fontan procedure depends on various factors, the first of which is the choice of the patient. Not all the children born with univentricular congenital disease are optimal candidates for this operation; they have to be strong enough to support all the surgeries and they must have some requirements as mean pressure of PAs and pulmonary resistances values under a certain threshold, absence of stenosis in PAs, etc. Patients that satisfy all these criteria have 81% survival possibilities till 10 years. However, if one of these requirements is not satisfied, the same percentage reduces at 60-70% (Gatzoulis et al., 2007).

In any case, univentricular disease is a severe condition and Fontan procedure is a surgical procedure that presents several critical issues: long-time complications can occur in each patient and they are a long list. The most common are: arrythmias, systemic and pulmonary thrombi formation, atrioventricular valve regurgitation, pulmonary arteriovenous malformations (PAVMs), protein losing enteropathy (PLE), low exercise tolerance, cyanosis or hypoxemia, ventricular failure (Gatzoulis et al., 2007; Giunta, 2016). The cause is the non-physiology of the connection which causes an increased ventricular afterload (systemic and pulmonary resistances), a decreased ventricular preload (ventricular filling) and a major central venous pressure due to the absence of right ventricle work (Rychik & Cohen, 2002).

There are also some mechanisms that bring Fontan procedure to failure. The first one is vascular resistance: because of the absence of a right pumping chamber, pressure difference between IVC and left atrium is the only driving force for blood flow from vessels' connection to the lungs and so, the higher the downstream resistance is, the higher pressure difference is required to achieve a given cardiac output. Another complication is related to the PAVMs: these malformations are spontaneous shunt connecting pulmonary arteries with pulmonary veins that cause a sort of lungs bypass. This situation leads to a decreasing oxygen saturation and an increasing in pulmonary vascular resistances that brings to a hypoxia state (Giunta, 2016).

Even connection efficiency needs to be studied: main energy dissipation factors identified in literature are flow pulsatility, exercise condition and increase of cardiac output, connection geometry, flow split in the PAs and variations in pulmonary resistances (that brings to failure as said before).

Because of heart pumping function, some studies focused their attention on power losses due to flow pulsatility: in general, the results showed that "when the flow pulsatility is high, there are larger fluctuations in the flow, which can cause discrepancy between the results from pulsatile and steady simulations" (Khiabani et al., 2012). However, because of the non-physiologic condition of univentricular heart, the inflows in TCPC comes from the venous return which has a low pulsatility: in literature, the largest number of articles doesn't consider the flow as pulsatile. Khiabani underlines that the error in calculating power losses due to time-averaged boundary conditions, is less than 10%, when flow pulsatility is low and that this error increases with the increasing in cardiac output.

When cardiac output increases, also the velocity of blood flowing in venae cavae increases: this condition causes a non-linear increment in power losses (Whitehead et al., 2007). At the same time, during exercise, if velocity increases, Reynold's number increases too: the risk in this case is to have an increment even in energy dissipation (Liu, Pekkan, Jones, & Yoganathan, 2004). To this condition, patient with SVHD reacts with a reduction of sportive performance because the oxygen distribution in the body decreases.

From an energy dissipation point of view, there are no relevant differences between intra-atrial and extra-cardiac total cavo-pulmonary connections (Haggerty et al., 2014). But connection geometry influences power losses very much: the main factors are diameter and cross-section of the vessels. When venae cavae are narrow, blood flow is faster, causing elevate stress on the PAs walls: this condition can bring dissipation (Migliavacca, Dubini, Bove, & de Leval, 2003; Ryu et al., 2001). Even the PAs dimensions are important because a little section or a stenosis causes an unbalanced pulmonary flow spit (Haggerty et al., 2014). Moreover, a non-planar connection can have the consequence of a slight increase in power losses (Ryu et al., 2001).

Connection efficiency depends on many factors: one of these is the percentage of flow split in the LPA and RPA branches. There is no present in literature the ideal split, but several attempts were made to describe an energy dissipation trend based on the flow division: the results seem to underline that the lower power losses coincide with a similar split between LPA and RPA (40-60% split percentage), while an higher unbalance of the fluxes causes a worst dissipation condition (Ryu et al., 2001).

In any case, flow subdivision in TCPT depends a lot on pulmonary vascular resistances, because if they are unbalanced, even the flow will divide itself in a not similar way. Moreover, the unbalance of PAs resistances causes an increase of hydraulic and kinetic losses (M Grigioni et al., 2003).

Chapter 2 – Pre-processing

2.1 - CASE OF STUDY

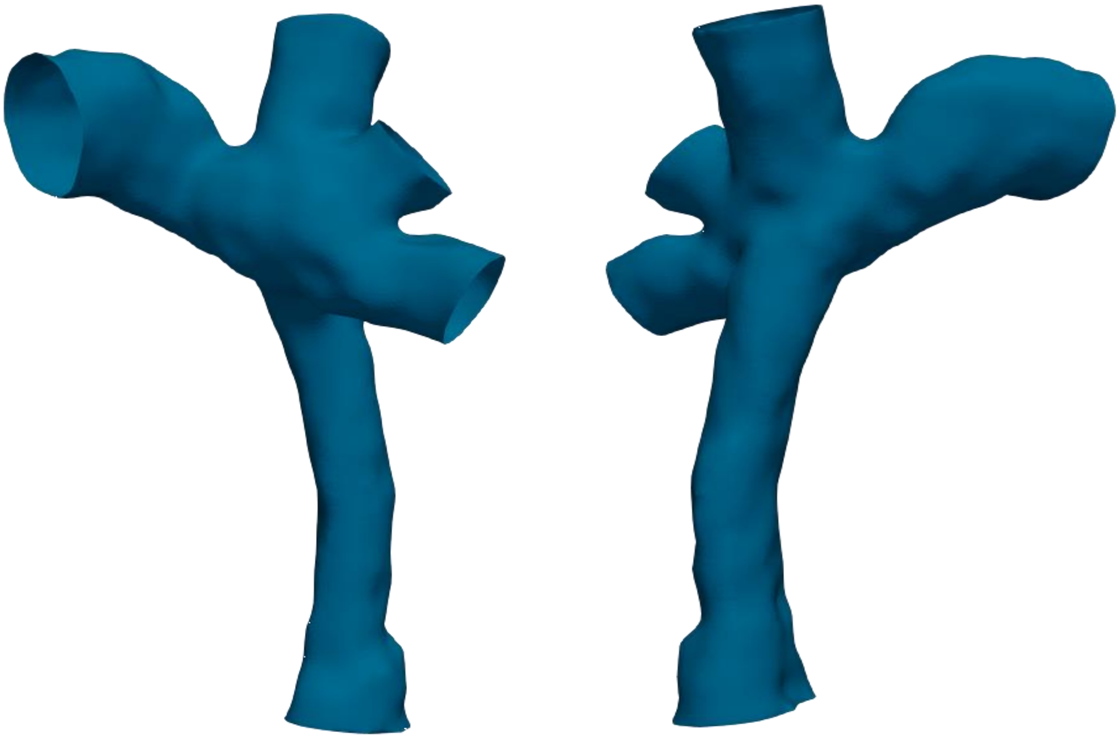

Figure 10 – front and back view of the analysed model

The patient-specific model analysed in this study (Figure 10) it was segmented from a patient at Bambino Gesù Hospital of Rome. The 3D geometry was obtained from a TC scan of child's heart. In literature there aren't many examples of numerical studies and simulations on patient specific Fontan's models, so this study started with a sensitivity analysis for different parameters.

This model has great complexity because of its irregular and realistic geometry and because of the altered flows that differ from the physiological ones: the model's analysis, study and preparation are complex too.

It is necessary to do preliminary steps in order to prepare the model for the fluid dynamics simulations. For the fluid dynamic simulation was used an open source finite element software: SimVascular. This software works in centimeters so the model had to be rescaled; to allow this it was used another open source software: VMTK, the Vascular Modeling Toolkit and in particular *vmtksurfacescaling* script.

After that, it was computed model's centerlines, defined as the place where the centres of maximal inscribed spheres are defined (vmtk, s.d.). They are necessary to compute the real area of each surface of the model and are fundamental to build the flow extensions (as explained later).

Once these things were done, it is possible to go ahead with the geometrical pre-study.

2.2 - GEOMETRIC ANALYSIS AND CHOICE OF VELOCITY INPUTS

It is necessary to start with a geometry study that helps to know vessels' cross-sectional areas and diameters and obtain from them velocities and flows values.

SimVascular was used to compute the inlets and outlets areas because it is more accurate and precise than VMTK and, also, it gives a direct file output with the areas. The only reference values for areas, velocities and flow rates were taken from literature literature: Figure 11 shows a table by Whitehead et al. in which several Fontan patients' data are compared (Kevin K. Whitehead, 2007).

Summary of Demographic, Flow, and Pulmonary Artery Cross-Sectional Area for Each Patient in the Study*

						EVLR			Cross-Sectional Area	
Patient	Age, y	Body Surface Area, m^2	SVC, L/min	IVC, L/min	Percent to LPA	(% to LPA) Rest	Ex3	CI, L/min/m^2	LPA, cm^2	RPA, cm^2
CHOP18	11.3	1.23	0.93	2.17	41	31	27	2.52	0.58	1.64
CHOP20	12.7	1.22	0.38	2.57	42	56	61	2.42	2.61	1.72
CHOP22	9.9	1.01	1.20	1.75	58	45	42	2.92	1.20	1.24
CHOP25	18.1	1.58	0.91	2.83	36	37	31	2.37	1.47	2.94
CHOP30	11.0	1.32	1.52	2.28	55	49	50	2.87	1.86	1.76
CHOP31	14.5	1.89	0.89	4.15	43	42	37	2.67	2.43	2.55
CHOP32	18.3	2.01	2.00	4.97	28	47	45	3.47	4.13	4.67
CHOP33	8.8	0.69	1.23	2.29	62	44	33	5.10	1.79	2.31
CHOP34	11.3	1.19	1.93	3.31	55	43	35	4.40	2.67	1.78
CHOP37	17.7	1.49	1.04	3.06	56	64	69	2.75	2.89	1.51

*Patients are referred to by their code in the Fontan database throughout the article.
Ex3 indicates 3x exercise condition; CI, Cardiac Index.

Figure 11 - Data from different patient (Kevin K. Whitehead, 2007)

The cross-sectional area comparable with our model is LPA because in our model two RPAs are present. Because LPA cross-sectional area of the analysed model is 3,01 cm^2, in Figure 11 patient CHOP37 was selected. This patient has the IVC flow with acceptable value: about three times the IVC flow, but lower than the standard aorta flow (about 4-5 L/min).

These data are useful to compute the diameter of all the vessels, approximating the cross-sectional area as circles. Then, it is necessary to convert SVC and IVC flows from L/min to cm^3/sec: these two values (that correspond to 17.3 and 51.0 cm^3/sec respectively) will be the flow input given to the pre-processing simulations that will be discuss later. Once the flow rates and areas are known, the SVC and IVC velocities are calculated.

From Whitehead's table we know the split percentage between RPA and LPA: 56% of the blood goes toward LPA, but the remaining 44% in our model has to be divided into the two RPAs. This further split is based on the RPAs' areas ratio: in the upper RPA (called also RPA1) goes the 48% of the blood that split in the RPA branch. Starting from the split percentage, it is possible to calculate PAs flows and velocities, but with a strong approximation, because it is hypothesized that the total caval flow is preserved: 4.1 L/min (SVC + IVC flow) would be divided between LPA, RPA1 and RPA2.

The first and the last point of this list are essential to calculate the entrance length and the Reynold's number.

Entrance length is the distance beyond which the flow is completely developed: it begins with the vessel entrance and it lasts until the velocity profile become parabolic. It is a sort of transition zone because at the entrance the velocity profile is flat and during this length it varies in (at least) two dimensions, one axial and one radial, while at the end of entrance length the velocity profile depends on the radial component only. All these facts are due to a non-equilibrium of the inner forces acting in the flow (viscous and pressure forces): once a balance is found, the velocity profile is parabolic and it remains unchanged in flow direction and the flow is fully developed as explained well in Figure 12. Another important condition that it is possible to see in Figure 12 is the no slip condition: because the wall is fixed (has velocity = 0 m/s), the parts of flow in contact with the wall have zero velocity too (Morbiducci, 2017a).

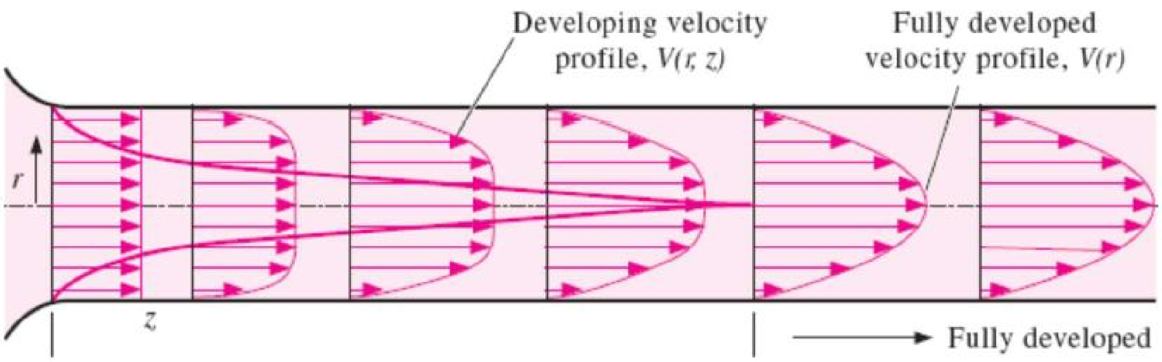

Figure 12 - Entrance length (Morbiducci, 2017a)

The formula to compute the entrance length is the following (Morbiducci, 2017a):

$$z_0 = kD^2 \frac{U\rho}{\mu}$$

with

- z_0 = entrance length
- k = proportionality constant derived from experiments, approximately 0,06
- D = diameter of the vessel
- U = velocity stream mean value
- ϱ = liquid density
- μ = liquid viscosity.

D and U are known thanks to the previous calculation and k is approximately equal to 0.06; ϱ and μ are properties of the fluid and depend on the rheological model of the blood considered. In this master thesis the blood is always considered a Newtonian fluid according to which viscosity is always independent from the velocity gradient and the shear stress is directly proportional to the velocity gradient through dynamic viscosity (μ).

Blood is a tissue consisting of a suspension of different elements in an aqueous solution: the aqueous solution is called plasma, is 90% made of water and the substances dissolved in it are organic and minerals. On the other hand, in the blood there are different corpuscular elements (platelets, erythrocytes and leukocytes): red blood cells (rbc) are the most present in the blood and are the component that most influences the haematocrit. More correctly, haematocrit (Ht) corresponds to the percentage volume of blood occupied by erythrocytes and has value between 38 and 52% (in general it is considered equal to 45%). Each one of these blood components has a different density and in normal conditions the values are: ϱ_{plasma} = 1035 Kg/m^3 and ϱ_{rbc} = 1090 Kg/m^3. Total blood density is function of the haematocrit and the calculation is $\rho_{blood} = (1 - Ht)\rho_{plasma} + Ht\rho_{rbc}$ (Morbiducci, 2017c). If Ht = 45%, ϱ_{blood} = 1060 Kg/m^3; this value is been used in all the calculation involving blood density.

As it was said before, shear stress is directly proportional to deformation velocity with a proportionality constant that corresponds to dynamic viscosity: mathematically, $\tau = \mu\dot{\gamma}$ (Morbiducci, 2017c). μ is a fluid thermophysical characteristic that depends on the temperature, but not on the flow field (in case of Newtonian model). Since there are a lots of cell components, it can seem a strong imposition considering blood a homogeneous fluid with a Newtonian behaviour. However, if the vessels have a diameter greater than 0,3 mm, this approximation is unanimously considered valid: the corpuscular elements have a diameter lower than two orders of magnitude and they don't influence total blood behaviour. At the end, it is possible to conclude that, in terms of viscosity, blood con be considered a Newtonian fluid. The value range acceptable for μ is 3÷4 cP (1 cP = 10^{-3} Pa*sec) and in this thesis' calculation μ = 4 cP.

Now, all terms of z_0 equation are known and it is possible to calculate all PAs' entrance lengths. Entrance lengths indicate how much the PAs should be extended in order to have completely developed flow at the outputs and the aim is to build some flow extensions of that length. Unfortunately, the results in the calculation of PA's entrance lengths are not acceptable: both RPAs would require a 30 cm entrance length and LPA even longer. However, it is not possible to make flow extension of these length because they should require an exaggerated computational time during meshing and simulation steps. For these reason others entrance lengths were used as we will describe in the following sections.

Reynold's number (Re) is a dimensionless physical quantity and it allows to know if the flow in a cylindrical and rigid conduct is laminar or turbulent: this number represents the ratio between inertial and viscous forces. It depends on mean flow velocity (U), vessel diameter (D) and cinematic viscosity ($\nu = \mu/\varrho$) and its formula is

$$Re = \frac{UD}{\nu} = \frac{U\rho D}{\mu}.$$

Different Re values describes different flow regimes (Morbiducci, 2017b):

- if Re < 2000, the flow is considered laminar: flux remains stationary and it behave as if rectilinear sheets slide one on the other interacting only through tangential stresses;
- if Re > 2000, the flow is considered turbulent: it is characterized by a completely three-dimensional motion, by non-stationarity and by velocity fluctuations.

In general, in circulatory system flow is laminar, with some exception at the heart valves and in aorta during systole; diseased condition (as vessel narrowing at atherosclerosis or weakening of the wall) can result in turbulent flow too.

In this thesis calculation all the Re equation terms are known: the results of PAs' Reynold's number confirm that flow is laminar, with Re values below 1000.

2.3 - ANALYSIS AND COMPARISON OF DIFFERENT FLOW EXTENSIONS

As mentioned before, even if entrance lengths give the certainty of having fully developed flow at the outputs, they are too big to be reproduced in this thesis model because they should require an extremely long computational time. For this reason, another method has been found in order to choose the best flow extensions (FE) from computational and results' reliability points of view. FE are artificial cylindrical extensions of the fluid domain in order to minimize the dependence from the imposed boundary condition. The method adopted consists of making several attempts with different FE lengths: the global model quality is analysed during post processing comparing the values of different significant hemodynamic descriptors (pressure, WSS magnitude and velocity), their percentage differences and doing a statistical analysis.

The FE creation was done by *vmtkflowextensions,* a VMTK script that exploit the centerlines computation. Figure 13 shows an example of the model after FE addiction.

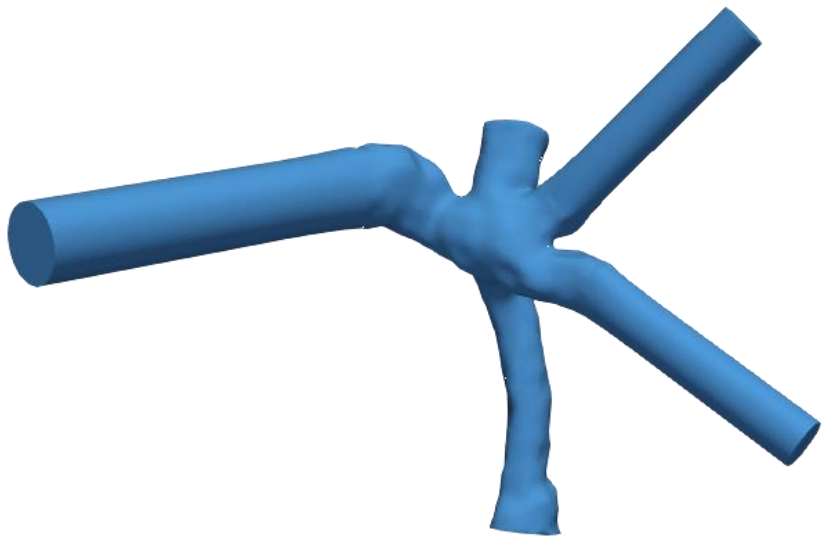

Figure 13 - 10x model (reference model)

The maximum flow extension allowed for this work is 10 times the radius of the vessel to which it is connected: this model is reported by Figure 13. It represents the most accurate case analysed in this work, so it is considered the reference model: several simulation and mesh parameters have been tried on it, in order to find the best solution, and the different FE are compared respect to it. It is possible to notice that the vessels' ends aren't hollow anymore: these holes have been filled thanks to a SimVascular command in order to make outlets and inlets' surfaces visible. Let's see in detail the work on SimVascular.

2.3.1 - *BEST MESH AND SIMULATION PARAMETERS ON SIMVASCULAR*

At this point, the first step to do with the solid model (obtained thanks to VMTK) is meshing.

"Discretization, also known as grid or mesh generation, is defined as the process of breaking up a physical domain into smaller sub-domains (usually called elements)". Discretization is necessary in order to facilitate the numerical solution of partial differential equations. The three fundamental challenges of this method are: robustness, mesh quality, and computational efficiency in generating the mesh. The elements can have different shape, but in this moment the tetrahedral ones are the most used: this current dominance of tetrahedral meshing can be attributed most notably to its ability to robustly mesh arbitrary, complex geometries. "In addition, the use of tetrahedral elements often simplifies the process of adapting the mesh during simulation" (SimVascular, 2017).

Mesh generation consists of a discretization of the flow domain into little pieces (the elements) for simulation, once the solid model of the object of interest is obtained. For the reasons mentioned above, SimVascular uses tetrahedral elements for meshing, with TetGen as the open source mesh generation software: then, the user can choice to implement boundary layers, mesh refinement and isotropic adaptive mesh.

On the reference model (the 10x case), different meshing options are tested, but Table 1 shows the best combination of these parameters for reference model mesh: we decided to impose two boundary layers because they make the discretization finer in surface edges, where normal meshing can distort elements; in addition, final GMES value is a compromise between computational time and accuracy.

	PARAMETERS	VALUE
	Global Max Edge Size (GMES)	0.1
Boundary Layers	Portion of Edge size	0.5
	# of Layers	2
	Decreasing Ratio	0.5

Table 1 - Meshing parameters in flow extension cases

This set of parameters will remain the same for all the models with different FE: in this way, the only thing that change will be the number of mesh elements (that will decrease with the decrease of FE dimensions), as it possible to see in Table 2. In 10x case, the total number of elements result in 1.54 million.

FE case	# of elements
10x	1.545 million
8x	1.361 million
7x	1.270 million
5x	1.097 million
3x	0.904 million
2x	0.815 million

Table 2 - Number of elements for each FE case

Next step, after mesh generation, is model preparation for the simulation: this process consists of setting inlets and outlets boundary conditions, wall properties and solver parameters. However, before starting to explain the whole pre-processing method, it is necessary to explain how do the SimVascular simulations (and solver) work.

The three-dimensional incompressible Navier-Stokes equations are the basis of the simulations: the solver in use can solve them in a vascular model domain constructed from image data. Here it is possible to see (Boivin, Cayré, & Hérard, 2000) Navier-Stokes equation for a Newtonian and incompressible fluid (with constant μ and ϱ and $\nabla \cdot \boldsymbol{v} = 0$, from conservation of mass equation):

$$\rho \frac{D\boldsymbol{v}}{Dt} = -\nabla p + \mu \nabla^2 \boldsymbol{v} - \rho \boldsymbol{g}.$$

svSolver is a finite element program and derives from the academic finite element code PHASTA, but with some additions and modifications (for example in Boundary Conditions and Fluid-Solid Interaction coupling) that allow to represent blood flow with a high level of realism. However, the added key functionalities that permit to have efficient and stable solutions are backflow stabilization (a large vessels problem that can cause divergence of numerical scheme), custom and efficient linear solver (that efficiently handle large cardiovascular simulations with arbitrary boundary conditions and reduced solution times) and multiscale coupling for closed loop boundary conditions.

Figure 14 contains a scheme of the processes involved in running a simulation using SimVascular. Starting from solid model and meshing files, it is possible to begin with the real pre-processing.

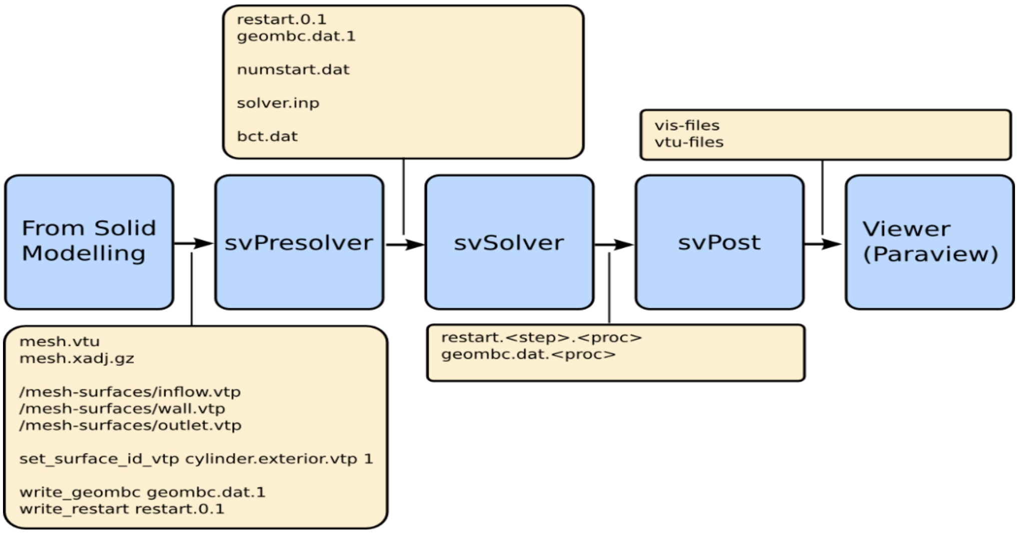

Figure 14 - SimVascular simulation flowchart (SimVascular, 2017)

The files belonging to the svPresolver section contain instructions about boundary and initial conditions and geometrical configuration. Units of measure have to be known before imposing these conditions: viscosity (μ) will have the value of 0.04 poise, ϱ is in gr/cm^3 and it will correspond to 1.06 gr/cm^3, from the values mentioned in the previous section. From these data it can be easily understood that blood in all this thesis' simulations is considered as a Newtonian incompressible fluid (M Grigioni et al., 2003; Khiabani et al., 2012; Liu et al., 2004; Migliavacca et al., 2003; Ryu et al., 2001; University of California San Francisco, 2018; Whitehead et al., 2007; Yoganathan, Dasi, & Pekkan, 2012). The μ and ϱ values together with initial pressure and initial velocities correspond to the SimVascular simulation "Basic Parameters": they are maintained as suggested by default with Initial Pressure = 0 dynes/cm^2 and Initial Velocities = 0.0001 cm/sec in all directions.

To perform our CFD simulations we set different boundary conditions: at the inlets (SVC and IVC) we imposed a constant flat velocity profile of, respectively, -17.33 cm^3/sec for SVC and -51 cm^3/sec for IVC (they have negative sign because of a SimVascular convention according to which forward flow coming into the model should have negative sign); concerning the vessel wall it was assumed rigid and it was set a no-slip condition (zero-velocity) (Grigioni et al., 2003; Liu et al., 2004; Migliavacca et al., 2003; Ryu et al., 2001); finally for the outlets in was set a 0D model composed from a resistance, the solid model is connected to the downstream vasculature through a multiscale coupling: the region of interest is isolated and studied with accurate local model, while the rest of circulatory system is described in a summary form (Chugunova, Doyle, Keener, & Taranets, 2019; Laganà et al., 2002; Pekkan et al., 2005; Quarteroni, Ragni, & Veneziani, 2001). In this case the downstream vasculature is represented by a resistance lumped parameter electric model.

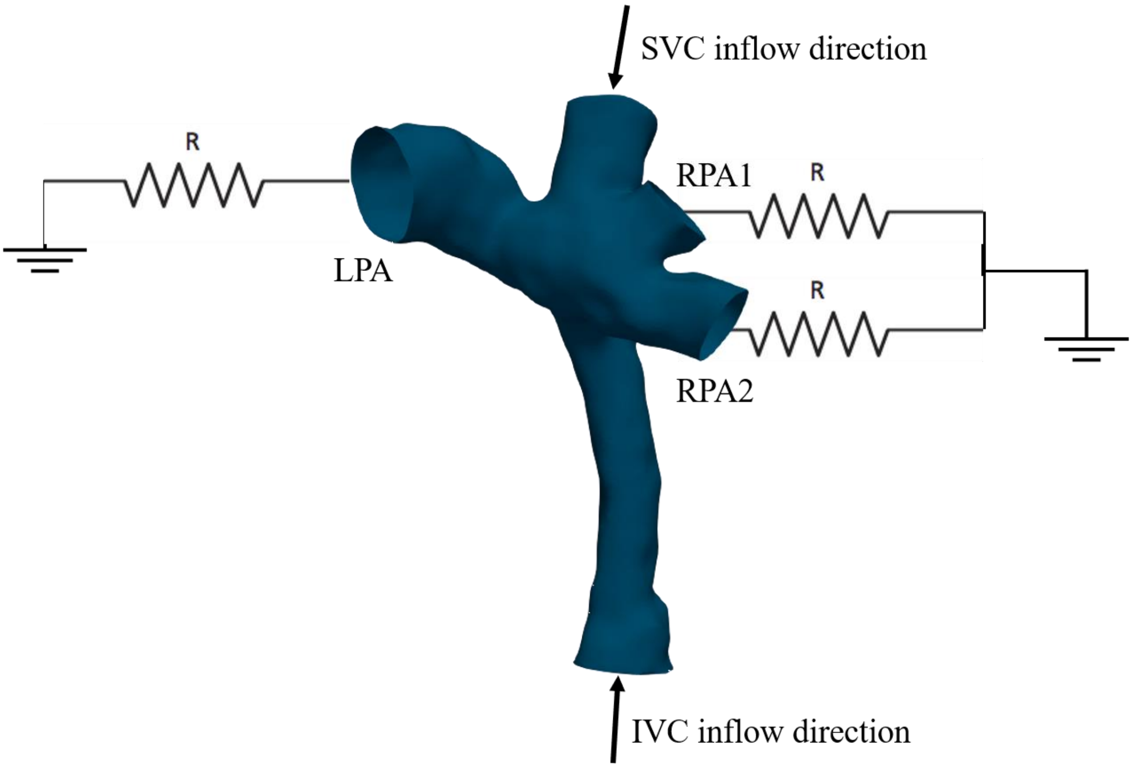

Figure 15 - 3D-0D coupling

In Figure 15 are presented the set-up of the simulations. The values of resistances used in our simulation are: R_{LPA} = 1000 dynes·sec/cm^5 and $R_{RPA\_equivalent}$ = 1000 dynes·sec/cm^5, which is composed by R_{RPA1} = 2042.85 dynes·sec/cm^5 and R_{RPA2} = 1958.92 dynes·sec/cm^5.

Before running simulation, the SimVascular user should choose the best combination of solver parameters: many attempts have been done in order to find the best compromise between the duration and the number of timesteps, the quantity of repetitions ("Step Constructions"), the residual criteria and the tolerance on equations. These are the most important parameters that have been changed and analysed: the goal is to obtain a simulation work that doesn't have an excessive duration and with stable results. The best solution for the most important simulation parameter is reported in Table 3.

PARAMETER	VALUE
Number of Timesteps	100
Time Step Size	0.1
Number of Timesteps between Restarts	10
Step Construction	30
Residual Criteria	0.0001
Tolerance on Momentum Equations	0.0001
Tolerance on Continuity Equations	0.001
Tolerance on svLS NS Solver	0.001
Time Integration Rule	First Order

Table 3 - Best set of solver parameters

To be sure of the results' quality, it is necessary to verify that the flow values in the outlets from a time step to the next one do not change more than 5%. In 10x case, the output flow values enter in the acceptable range, so it is possible to conclude that the simulation parameters are good.

2.3.2 - *COMPARISON BETWEEN FLOW EXTENSIONS*

The discretization and solver's parameters found before remain the same for all the several attempts with different flow extensions: in particular, Global Max Edge Size is maintained 0.1, condition that fixes the dimension of every element of the meshes and that implies that, with the FE length decreasing, the total number mesh elements will decrease too.

In order to reduce the computational time requested for the simulation resolution, other five trials were made: FE length corresponds to 8, 7, 5, 3 and 2 times the vessels radius. Figure 16 reported below represent all the model studied in this work.

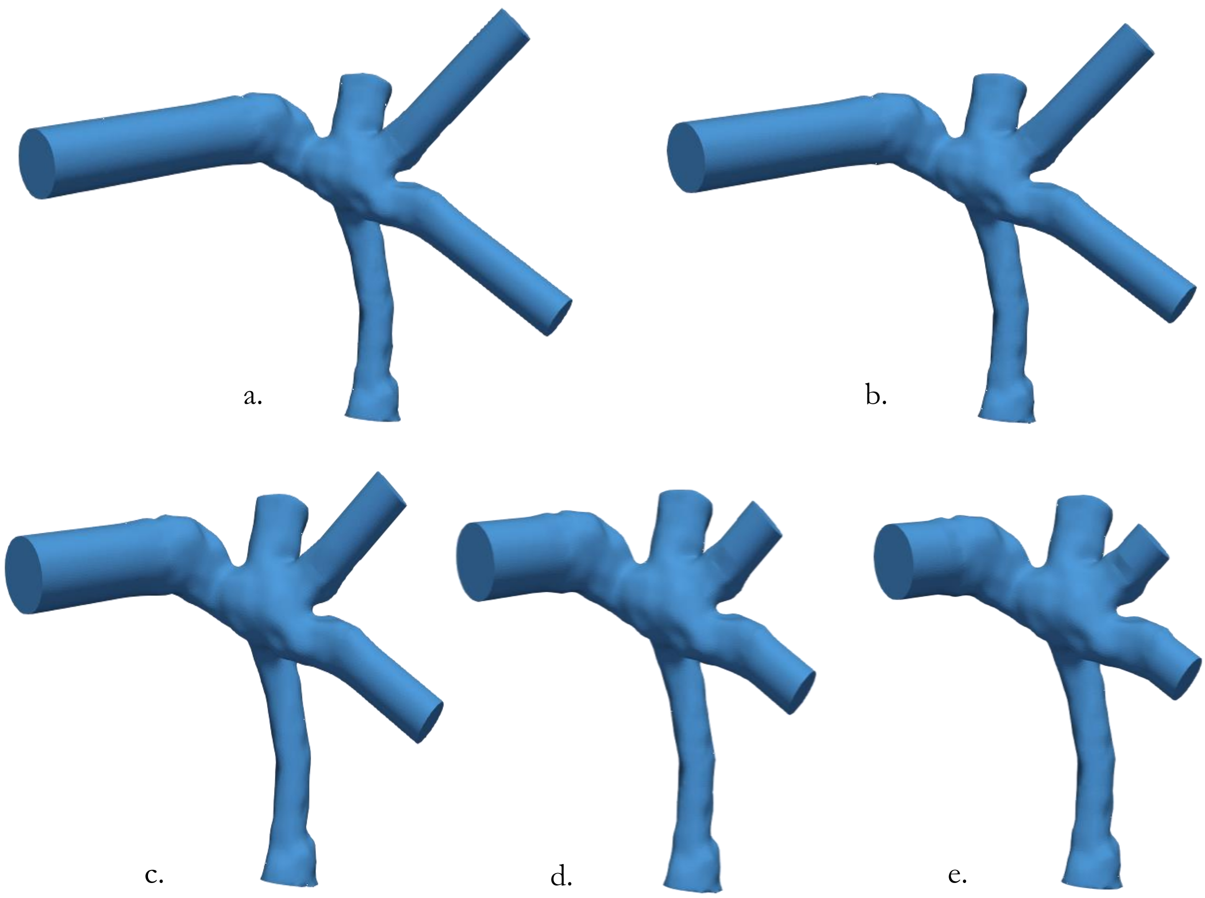

Figure 16 - All FE models: a. 8x model; b. 7x model; c. 5x model; d. 3x model; e. 2x model

A model without flow extension (like Figure 10) was used and discretized with the same parameters analysed before, without running any simulation on it (a sort of empty model): the data of each FE case mentioned above "are projected" on it in order to make the different models comparable. This process is been realized through VMTK software thanks to *vmtksurfaceprojection/ vmtkmeshprojection* script.

It is important to say that any visualization and figure of this work, through which a qualitative comparison is made, derive from the post-processing software used, Paraview: it is possible, thanks to this software, to rescale, to visualize all the distribution of all the parameters important during post-processing, and to observe the mesh too. It allows to put thresholds in order to improve results visualization (as it is possible to see next, in the distribution of percentage differences).

The post-processing analysis involves three key parameters for this study: pressure, WSS magnitude and velocity distribution.

The pressure is the force that the circulating blood gives to the wall. So, pressure is the inner force acting on each element of the surface, with a normal direction. Its unit of measure is dynes/cm^2 in SimVascular. The following figures report the pressure distribution on the whole model with values obtained from simulations of each FE case. The scale (Figure 17) is in dyne/cm^2.

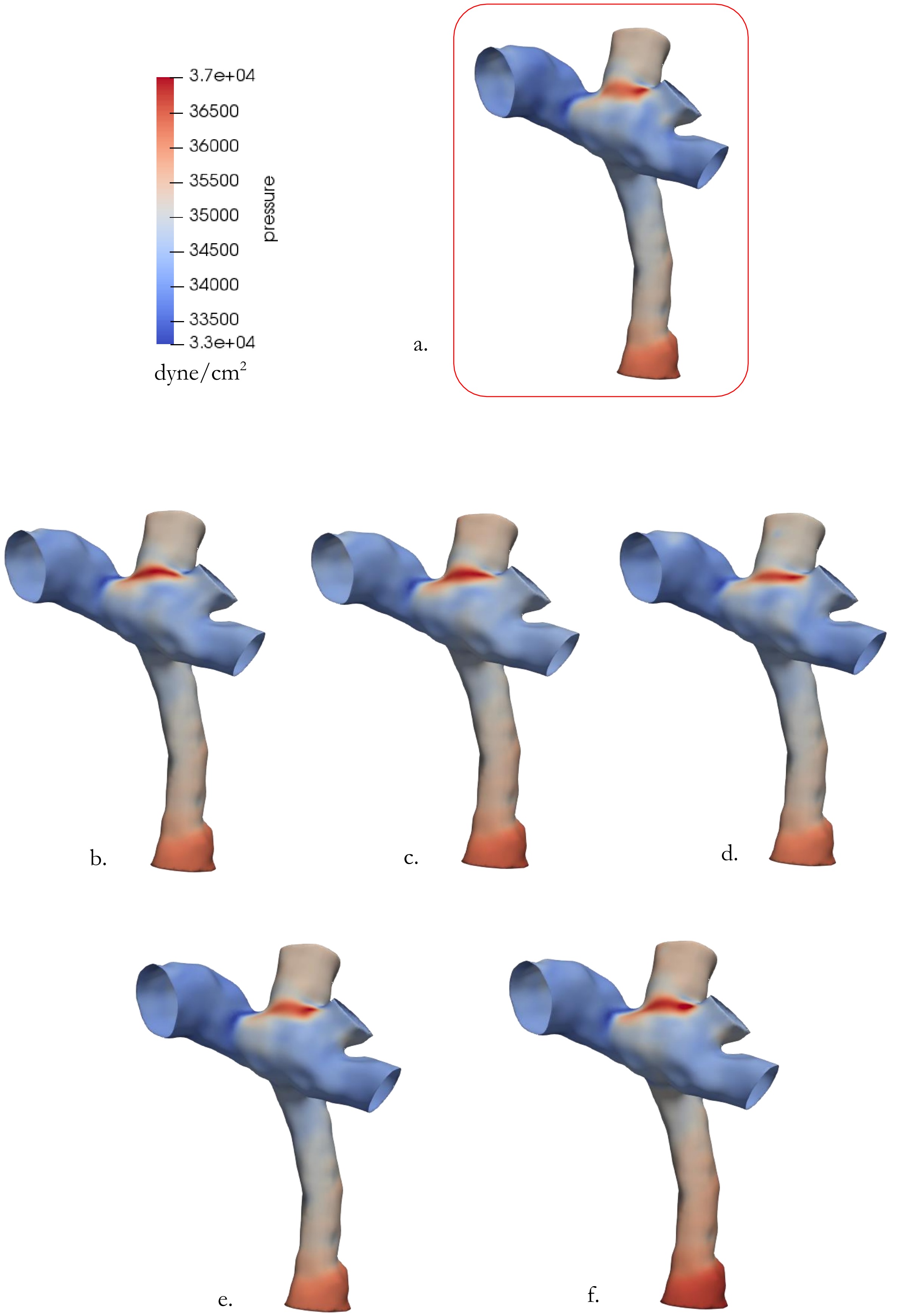

Figure 17 - pressure distribution: a. reference model (10x); b. 8x model; c. 7x model; d. 5x model; e. 3x model; f. 2x model

Maybe the most important parameter computable from the surface is WSS: this acronym represents the Wall Shear Stress that is a tangential force produced by a flowing viscous liquid (blood) on the conduct wall. This parameter depends on dynamic viscosity μ, on the velocity field parallel to the wall *u* and on the distance from the wall *y*. In fact, as it is possible to see in Figure 18, in laminar flow profile the velocities at the centre of the vessel are faster than the ones next to the wall: this pattern of velocity field is the result of friction between the fluid and the vessel wall and is related to the blood viscosity. This friction creates a tangential force exerted by the flowing fluid and is referred to as the "wall shear stress". The magnitude of wall shear stress depends on how fast the fluid velocity increases when moving from the vessel wall toward the centre of the vessel: this velocity gradient near the wall is called the "wall shear rate" (Corrosionpedia, n.d.).

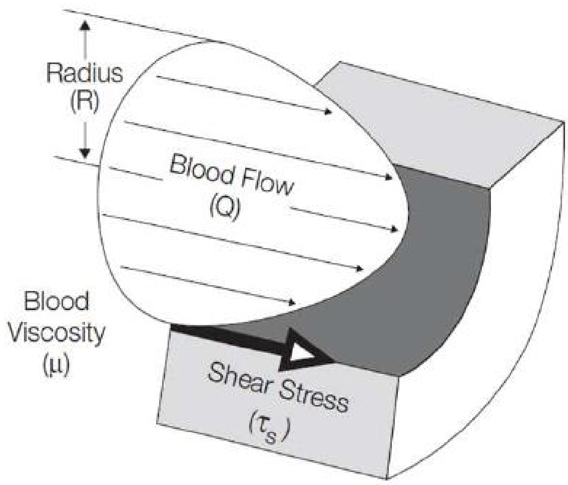

Figure 18 - Definition WSS (Morbiducci, 2017b)

The definition in terms of formula corresponds to $\tau_w = \mu \left(\frac{\partial u}{\partial y}\right)_{y=0}$ (Morbiducci, 2017b). This force is fundamental in any hemodynamic study because low and oscillating WSS has been proposed several times as a localizing factor of the development of atherosclerotic plaques, recirculation region in complex geometries and disturbed flow. Figure 19 below represents the WSS amplitude distribution in the model for every case studied.

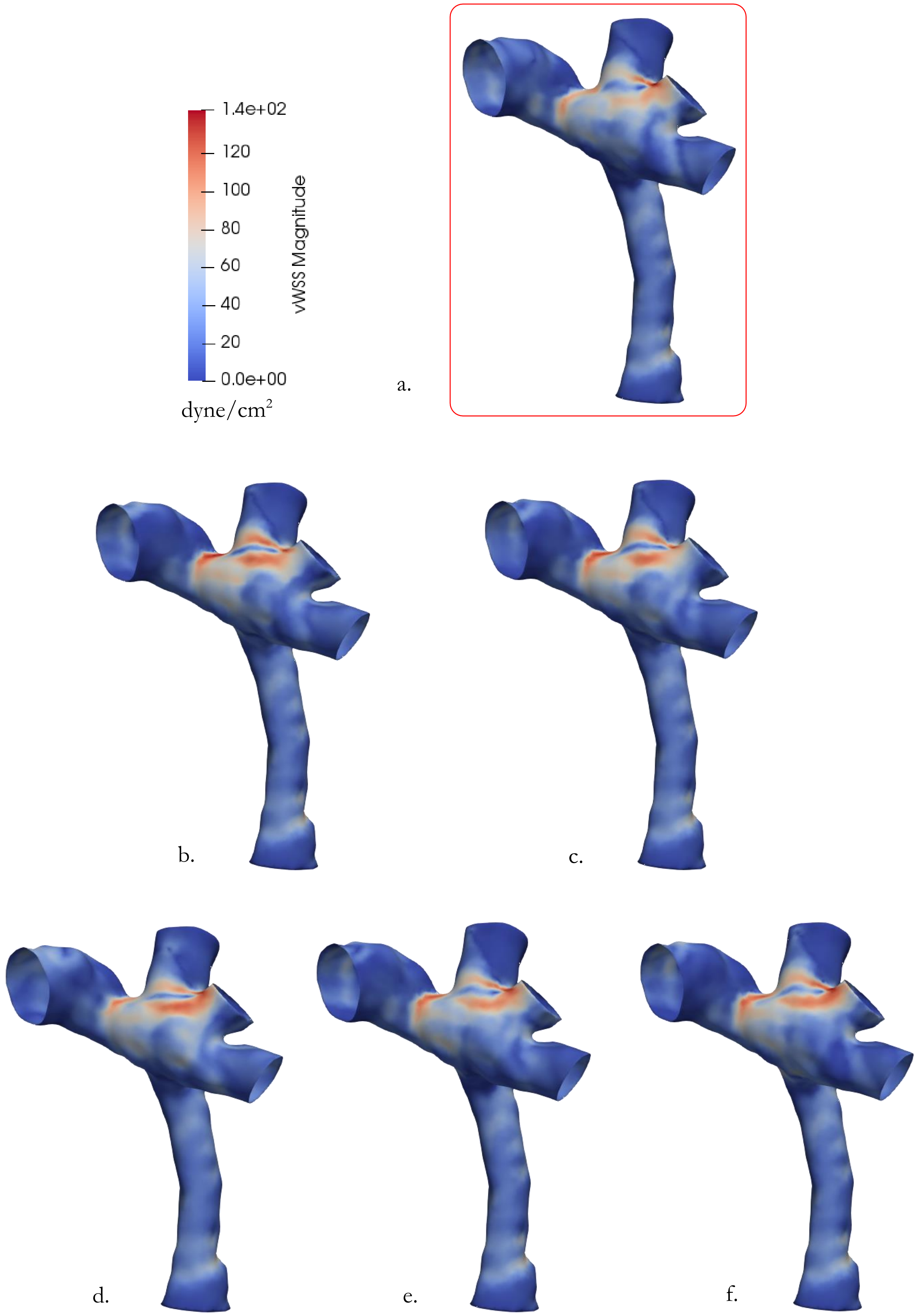

Figure 19 - WSS distributions: a. reference model (10x), b. 8x model, c. 7x model, d. 5x model, e. 3x model; f. 2x model

The last post-processing quantity is velocity, a volume parameter calculated on all the mesh elements: its unit of measure is cm/sec in SimVascular, and it is calculated on the direction of vessel axis.

For each one of these parameters in every model maximum, minimum and mean values are evaluated. This calculation is done by the mean of a Python script. Mean is the most useful and significant value: the mean values of pressure, WSS and velocity of each tested model are compared to the equivalent values of reference model. In order to quantify this difference, the attention has been focused on the different percentage calculation obtained thanks to Excel: the maximum acceptable tolerance is 5% respect to the 10x model. The different percentage formula is the following:

$$\%difference = \frac{model\ of\ interest\ mean\ value - reference\ mean\ value}{reference\ mean\ value} * 100.$$

We know that reference mean values are 34830.341 dyne/cm^2 for pressure, 23.144 dyne/cm^2 for WSS magnitude and 27.111 cm/sec for velocity; while Table 4 shows all the values in the different cases.

MODEL		**WSS (dyne/cm^2)**	**PRESSURE (dyne/cm^2)**	**VELOCITY (cm/s)**
2x	mean value	24.200	34961.191	27.209
	percentage difference	4.562%	0.376%	0.362%
3x	mean value	22.983	34858.915	26.850
	percentage difference	-0.697%	0.082%	-0.962%
5x	mean value	23.734	34853.291	27.270
	percentage difference	2.549%	0.066%	0.589%
7x	mean value	23.374	34856.805	27.259
	percentage difference	0.991%	0.076%	0.549%
8x	mean value	23.755	34884.134	27.219
	percentage difference	2.640%	0.154%	0.399%

Table 4 - Mean values and percentage differences

As it is possible to see in Table 4, the 5% tolerance is respected for all the model in all the parameters considered, so it is difficult to choose a model.

Another comparison has been done: the data projected to the no-FE model allow to build through a Python script a percentage difference punctual map of each model respect to the reference model for pressure, WSS magnitude and velocity. The input files of the script are the reference one and the interested model one both without flow extensions (created before), because in this way they are completely and punctually comparable, and both .vtp for pressure and WSS or both .vtu in case of velocity.

At this point we have all the punctual values in order to achieve the difference percentage map visualized and processed in Paraview software. In addition, through the Python script the mean value of the difference percentage distribution is calculated for each parameter. In this comparison the tolerance value isn't fixed: obviously, in punctual cases the percentage differences values will be much higher than the mediated ones and, as it is possible to see in the following, the considered parameters have very variable and different values. Figure 20, Figure 21 and Figure 22 represent the difference percentage maps of the most interesting region (the centre of the model) in order to allow a qualitative and a visual comparison.

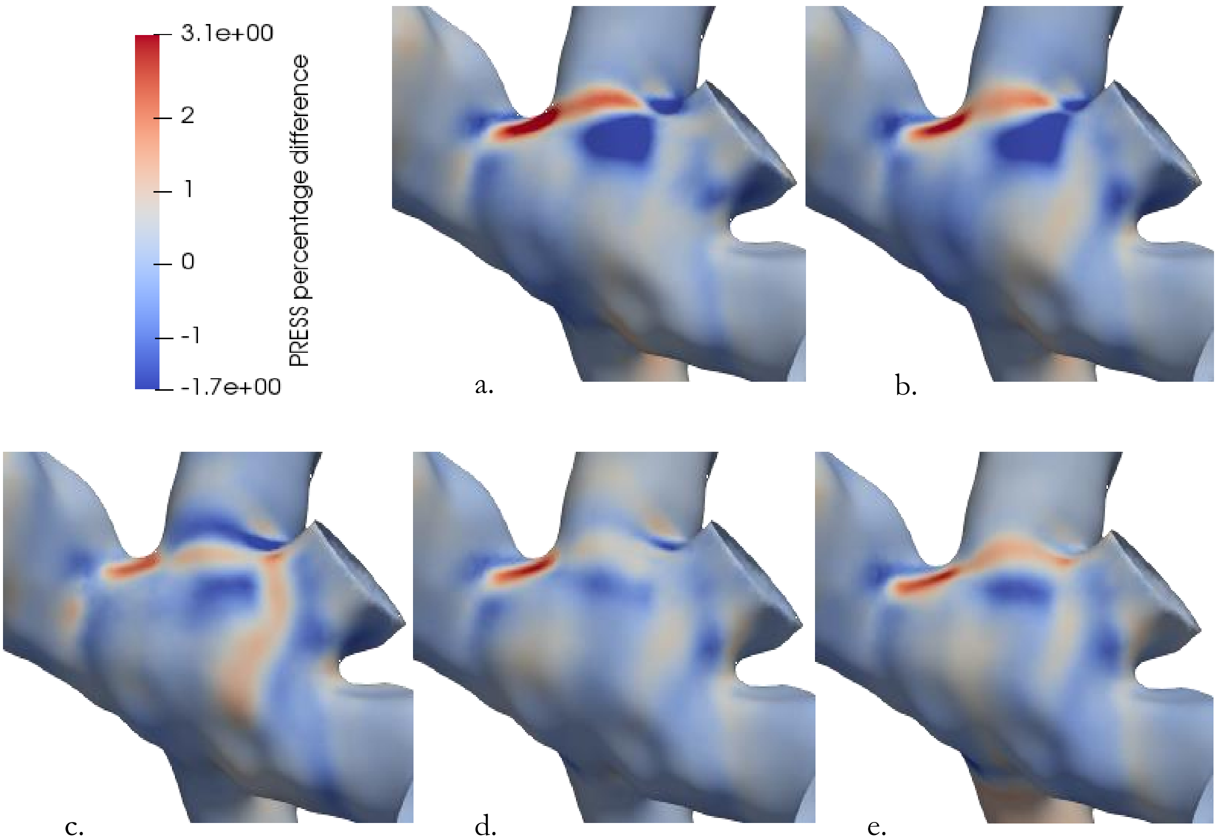

Figure 20 - Pressure percentage differences maps: a. 8x model; b. 7x model; c. 5x model; d. 3x model; e. 2x model

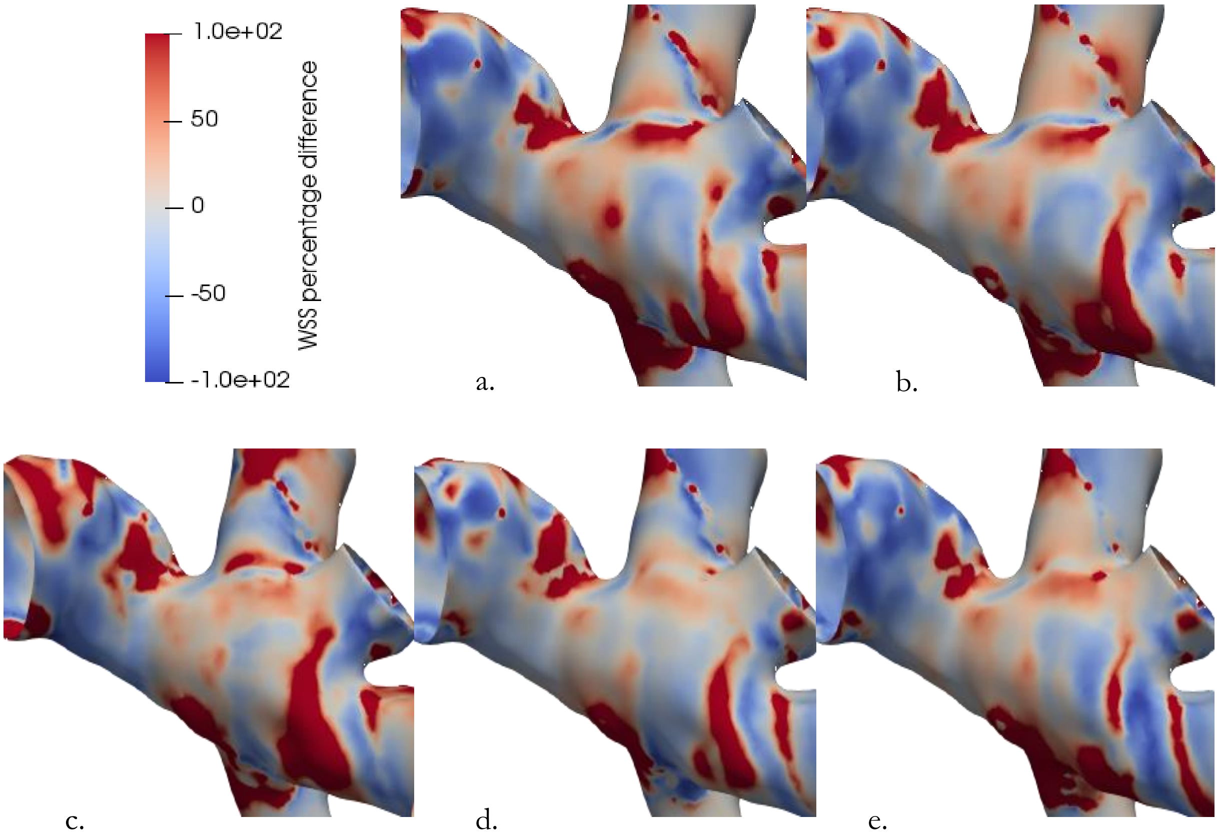

Figure 21 - WSS magnitude percentage differences maps: a. 8x model; b. 7x model; c. 5x model; d. 3x model; e. 2x model

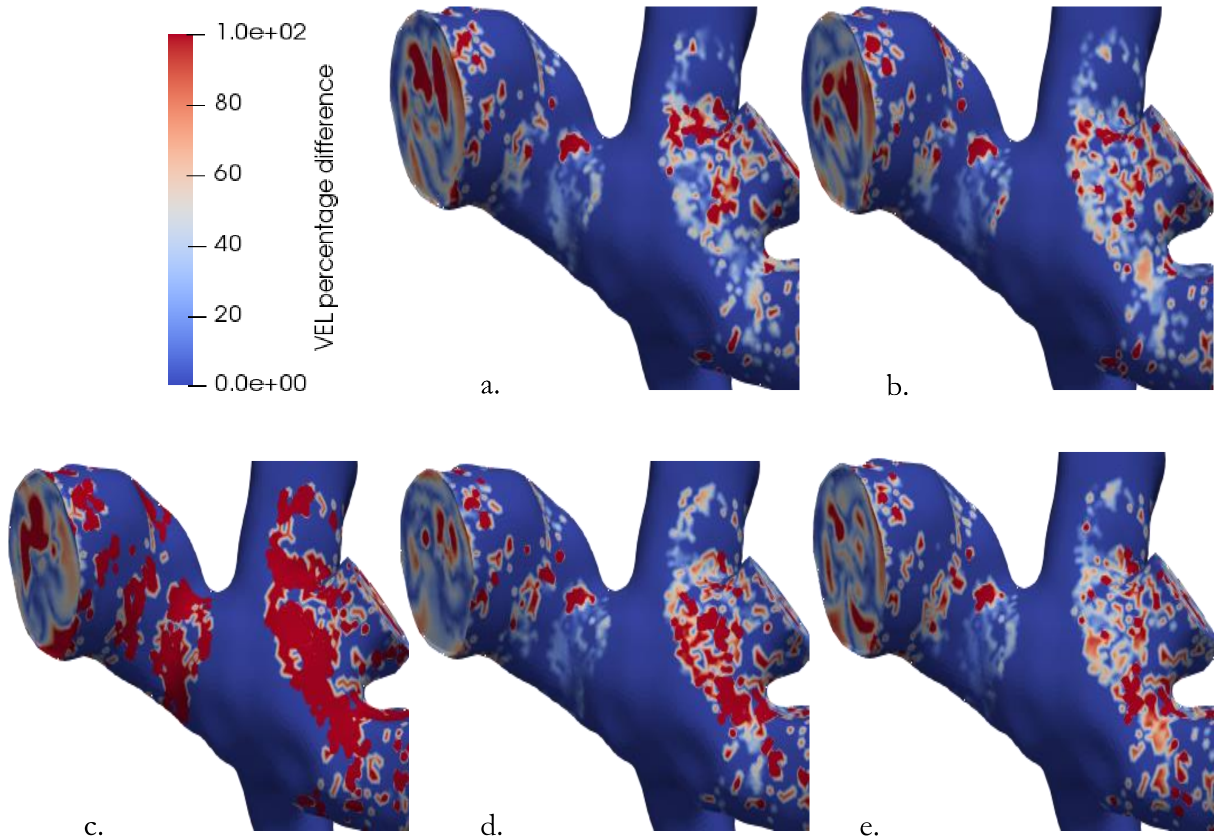

Figure 22 - Velocity magnitude percentage differences maps: a. 8x model; b. 7x model; c. 5x model; d. 3x model; e. 2x model

	x2	x3	x5	x7	x8
WSS	13.156 %	7.388 %	21.832 %	13.000 %	16.059 %
PRESS	0.370 %	0.081 %	0.067 %	0.075 %	0.154 %
VEL	32.998 %	27.197 %	355.115 %	32.818 %	34.210 %

Table 5 - Mean of percentage differences

Table 5 represents the mean value of the punctual percentage differences calculated for each model for all the parameters considered: here it is possible to see that pressure has percentage differences means very low, values that allow to say that pressure can be neglected in this comparison and that it isn't a key parameter for flow extension evaluation.

In Figure 21 and Figure 22 it isn't so clear what happens in the models and what are the differences between them: on the basis of Table 5 some thresholds are imposed in order to better visualize the percentage differences distribution and to notice some qualitative and remarkable difference in the models. In WSS case, the scale goes from -100 to +100 %: a threshold is imposed to ±20% in order to better identify the areas in which the difference from the reference model is higher. At the same time this threshold must have a higher value respect to the mean one reported in Table 5. In Figure 23 it is possible to see in blue the values < -20% and in red the > +20% ones: the distribution of the values that exceed the threshold is different in every model and it is very difficult to choose the best one.

On the other hand, velocity percentage difference mean values are very variable: the scale goes from 0 to 100% and the threshold is imposed at 35%. The threshold has to be higher than the majority of the velocity mean values (to have a better visualization of the situation), but it can't be too high because it is a sort of tolerance and it can't be considered acceptable if is too big. In Figure 24, the red volumes are the ones that exceed the threshold: their presence is different, but massive in all the models and the choice of the best FE model is even more difficult than before.

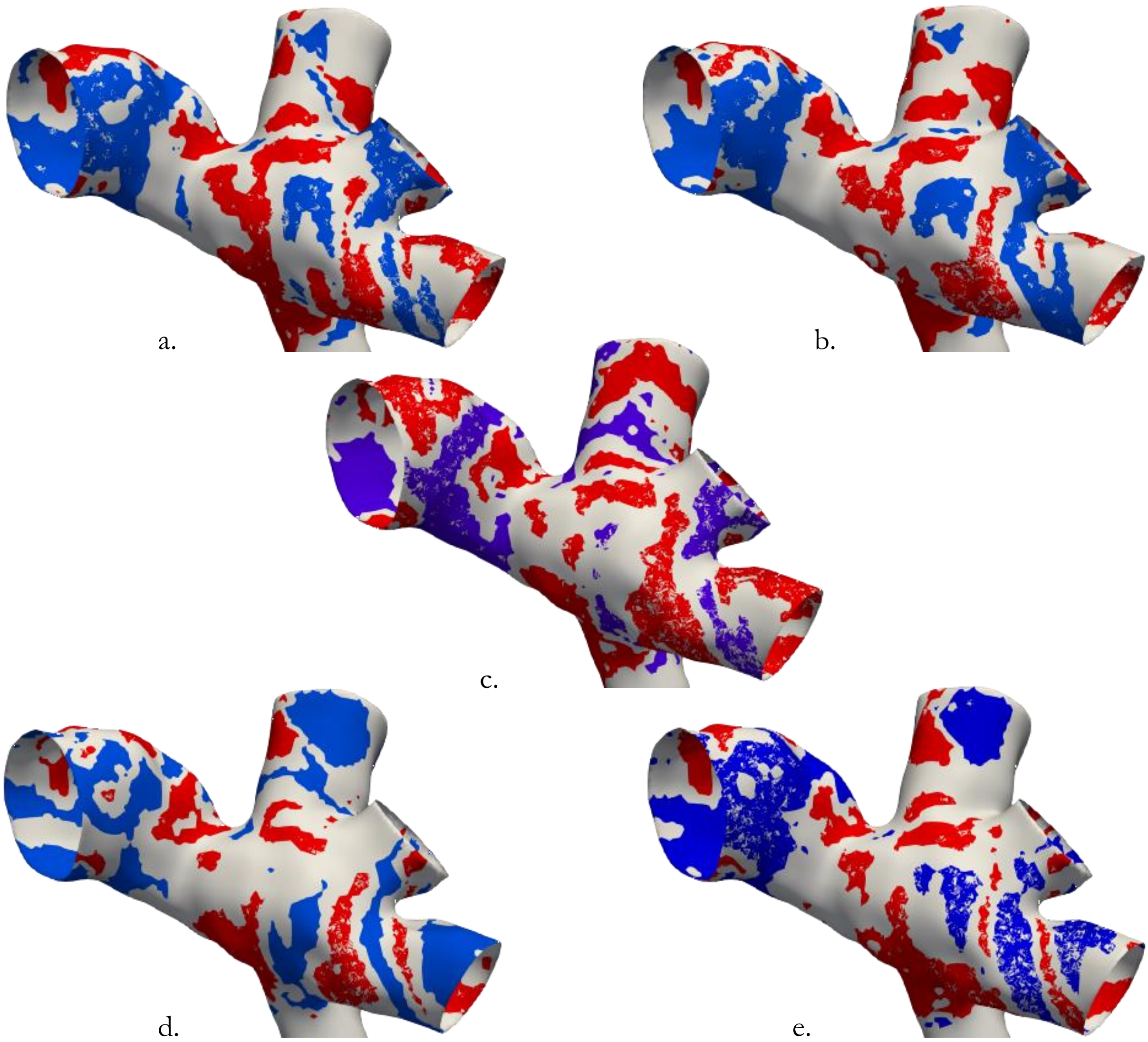

Figure 23 - WSS percentage differences with thresholds: a. 8x model; b. 7x model; c. 5x model; d. 3x model; e. 2x model

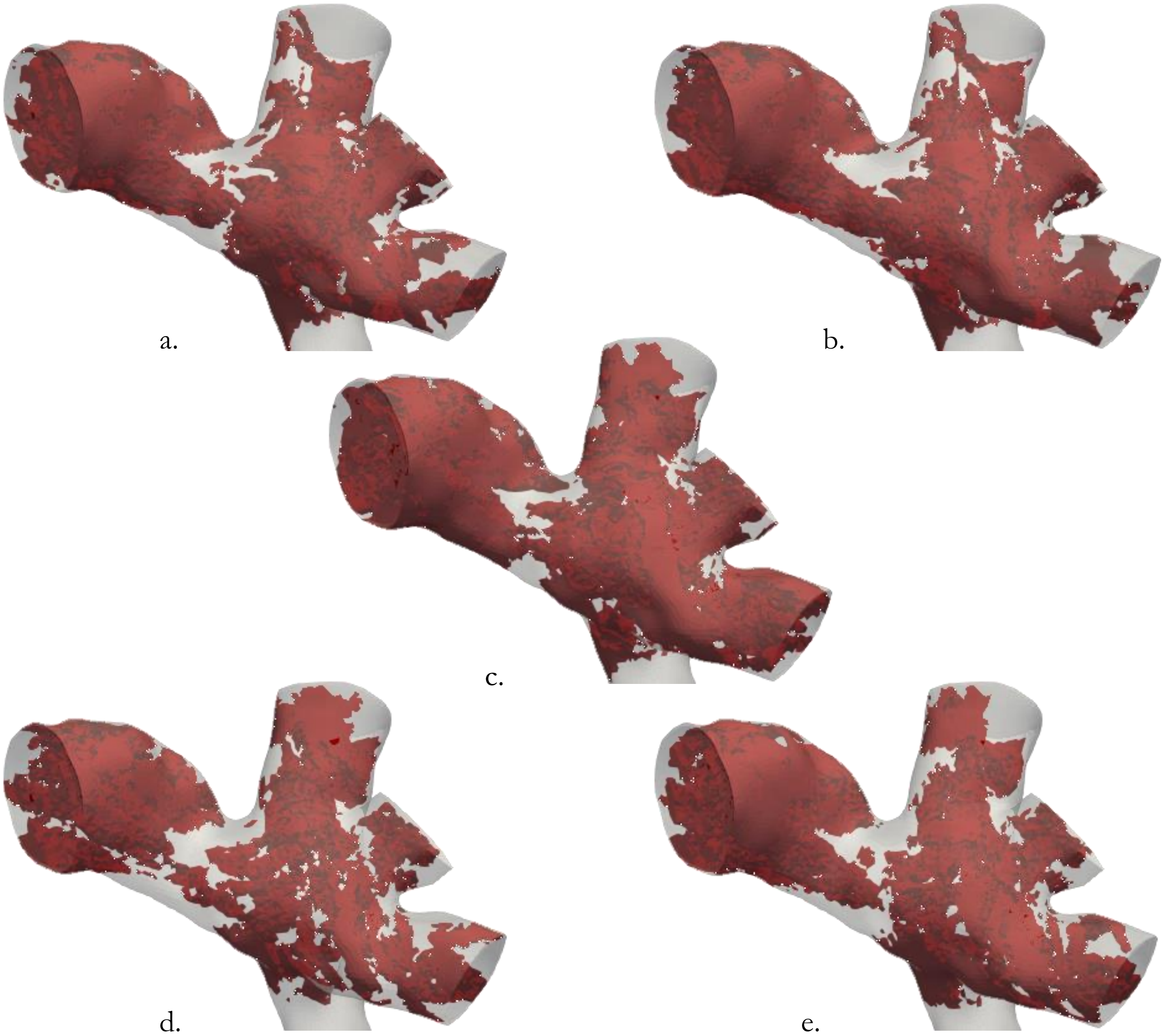

Figure 24 - Velocity percentage differences with thresholds: a. 8x model; b. 7x model; c. 5x model; d. 3x model; e. 2x model

As said before, it is almost impossible to make some conclusions from this comparative analysis. For this reason, another type of comparison is made in order to finally establish an FE model with a lower computational cost than the reference one but with acceptable results: it has been made a statistical analysis of the WSS and velocity values derived from the simulations explained before. The array created before in the Python script contains the values of these quantities for all the mesh points: in case of WSS, calculated only on the surface, the total number of points is 14,110, while for the velocity, in which all the volume is considered, they are 110,588. For all these points the Excel statistical analysis has been made, which allow to see the main statistical parameters for a distribution of values: the attention has been placed on mean value, standard deviation, variance, kurtosis and skewness. Table 6 reports the values of these statistical quantities for the reference model.

REFERENCE MODEL (10x)	WSS (dyne/cm^2)	Velocity (cm/sec)
Mean	23.141	22.607
Standard deviation	17.751	17.545
Sample variance	315.0995	307.833
Kurtosis	3.6151	-0.657
Asimmetry	1.6428	0.550

Table 6 - Statistical parameters values of reference model

After these statistical parameters have been found for all the other models too, the percentage differences are calculated as usual for each FE case respect to the reference model. Table 7 and Table 8 report the percentage differences values for WSS and velocity: the green values correspond to the lowest one, while the red ones represent the worst value regarding the same statistics.

WSS	2x	3x	5x	7x	8x
Mean	4.562	-0.697	2.549	0.991	2.640
Standard deviation	14.584	5.216	4.445	6.161	8.740
Variance	31.296	10.703	9.087	12.702	18.244
Kurtosis	1.214	12.171	14.355	14.834	15.293
Skewness	2.463	5.689	5.307	8.778	8.518

Table 7 - Percentage differences of WSS statistics

Velocity	2x	3x	5x	7x	8x
Mean	0.617	-0.806	-0.070	0.638	0.474
Standard deviation	4.556	1.399	0.836	2.926	3.297
Variance	9.319	2.818	1.678	5.938	6.703
Kurtosis	-3.940	1.597	5.392	6.899	5.681
Skewness	10.031	4.551	4.534	4.239	5.119

Table 8 - Percentage differences of velocity statistics

The model that have more lowest values and no high percentage differences is 5x: the previous comparisons don't give much information to change this preference. So, the final choice is the model with FE length that correspond to 5 times the vessel radius: it is a good compromise between results and computational times and costs.

2.4 - SENSITIVITY ANALYSIS

Once the best flow extensions' length is identified. it is possible to go ahead with the pre-study of the model doing the sensitivity analysis: this process allows to choose between a wide range of discretizing patterns the optimal (uniform) mesh without making significant errors and optimizing computational time and costs.

The IVC branch was cut because in this part of the vessel there is a bulge (in red in Figure 25) that is the distortion cause of any mesh attempt. The only way to overcome this problem is to clip out the bulge and consider a shorter IVC, as shown in Figure 25: it was possible to cut the model thanks to a Pyhton script in which, after the VMTK centerlines computation. the user can see how long the SVC and IVC are and he can decide how many centimeters the IVC would be long after the cut. In this case the IVC is imposed to become of 6.2 cm and so the cut section has a 1.37 cm length.

It is important to say that this adjustment doesn't bring to any flow modifications and that in all the next steps the new 5x cut model is used.

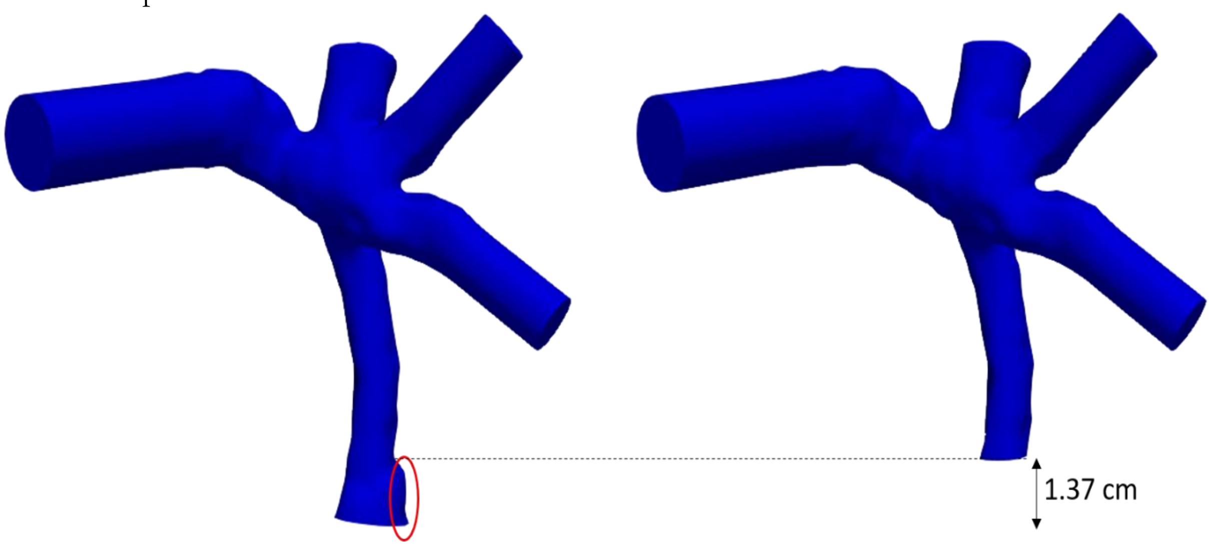

Figure 25 – Modifications applied on 5x model

Before proceeding with the best mesh individuation and the sensitivity analysis, an attempt to simplify the global discretization of the model is tried: the doubt is about if it can be possible to use a non-uniform mesh construction, with a coarse discretization on the flow extension and a finer one on the region of interest. In this way, the computational costs are reduced, but the results on the centre of the model are accurate.

2.4.1 - *UNIFORM OR NON-UNIFORM MESH?*

The difference between these two types of mesh is that in the uniform discretization the elements size is the same in the whole model, while in the non-uniform one the elements are larger on the FE and smaller in the region of interest in order to optimize computational costs and to have accurate results only in the most important area of the model. As before, all the meshing and simulation work is made thanks to SimVascular software.

Basic parameters for an optimal discretization are the same for both cases and are shown in Table 9.

	PARAMETERS	VALUE
	Global Max Edge Size (GMES)	0.085
Boundary Layers	Portion of Edge size	0.6
	# of Layers	3
	Decreasing Ratio	0.6

Table 9 - Meshing parameters

In the non-uniform mesh it is necessary to add another information that specify the elements' dimension in the flow extensions: in the Local size section of SimVascular all the PAs are selected and the element Edge Size is imposed to 0.4.

At the end, a mesh with 1 million of elements will be obtained in the non-uniform case, while the uniform one will have about 1.8 million of them. In Figure 26, it is possible to see the two meshes.

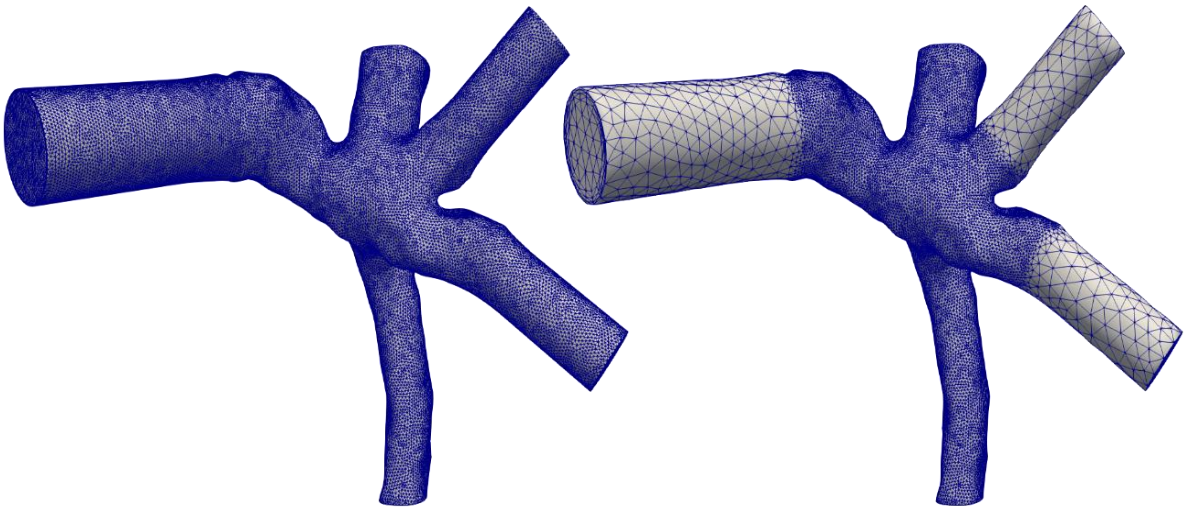

Figure 26 – Uniform VS Non-Uniform mesh

Once the meshing is done, the simulation works started with the same solver parameters used in the best FE choice showed in Table 3.

At the end of those simulations, the difference between the computational times is evident: the uniform mesh needed for 34 hours to make all the 100 time-steps on a one second steady simulation; on the other hand, the non-uniform discretization lasted only for 16 hours.

In order to understand if the simulation was stable and if the fluxes variation in the tested second was acceptable, the first step to do is the analysis of PAs flows (obtained thanks to a result file from SimVascular): if the percentage error of each time-step output flow respect to the one relative to 0.1 s is lower than 5%, the simulation can be considered stable. In Table 10 it is possible to see the percentage differences calculated for LPA, RPA1 and RPA flows in both cases.

UNIFORM MESH			
PERCENTAGE ERRORS (respect to step 10)			
step	**LPA**	**RPA1**	**RPA2**
20	0.158	-0.246	-0.074
30	0.105	-0.075	-0.136
40	0.181	-0.418	0.046
50	0.176	-0.341	-0.018
60	0.321	-0.690	0.039
70	0.268	-0.840	0.290
80	0.153	-0.509	0.191
90	0.551	-1.264	0.154
100	0.216	-0.446	0.006

NON-UNIFORM MESH			
PERCENTAGE ERRORS (respect to step 10)			
step	**LPA**	**RPA1**	**RPA2**
20	0.168	-0.246	-0.094
30	0.143	-0.126	-0.160
40	0.317	-0.760	0.117
50	0.347	-0.590	-0.110
60	0.312	-0.562	-0.072
70	0.002	-0.158	0.147
80	0.207	-0.451	0.030
90	0.415	-0.602	-0.231
100	0.327	-0.390	-0.268

Table 10 - Flow variation: percentage errors in uniform and non-uniform meshes

The percentage error is lower than 2% in both uniform and non-uniform mesh: the simulations are acceptable and stable, so it is possible to go on with the analysis. The next step is a qualitative and visual analysis made on WSS magnitude. In Figure 27 it is possible to observe the WSS distribution on the whole surface model for both discretization cases, while in Figure 28 a zoom is made in order to better observe the differences in the region of major interest.

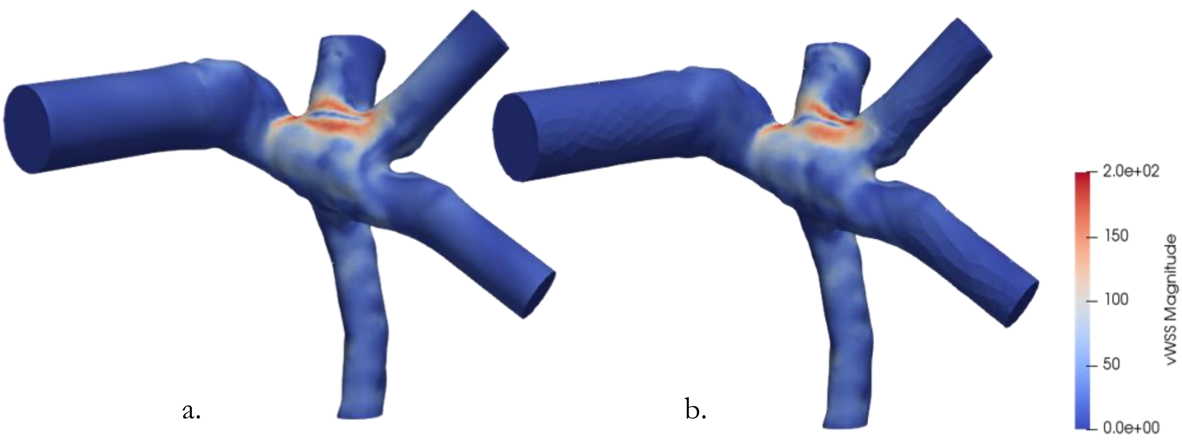

Figure 27 - WSS distributions [dyne/cm²]: a. uniform mesh, b. non-uniform mesh

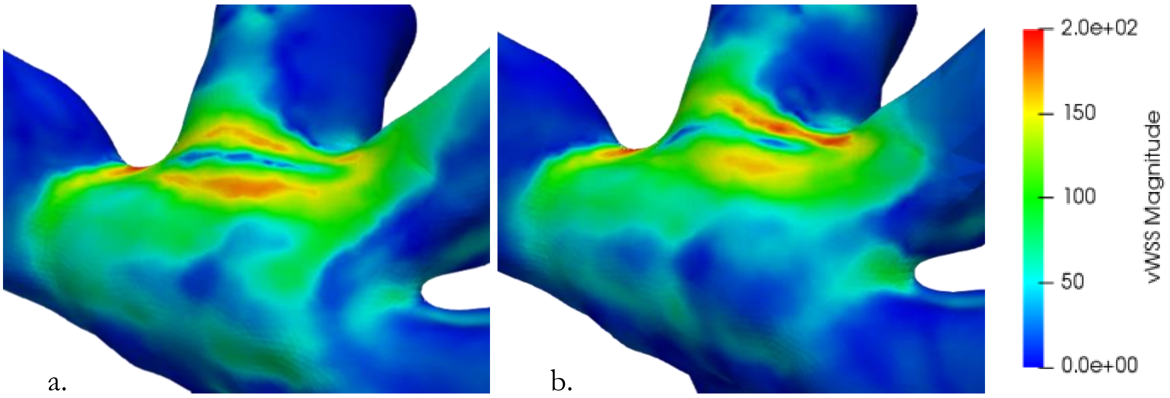

Figure 28 - WSS distribution in the region of interest [dyne/cm²]: a. uniform mesh, b. non-uniform mesh

Thanks to Figure 28, it can be observed that in the region of interest the two meshes applied on the model bring to a very different WSS distribution. This means that it is not possible to use the non-uniform mesh instead of the uniform one because the discretization affects too much the simulation results (in particular the WSS distribution), even if the gain in computational time is unquestioned. Obviously, the most accurate results belong to the uniform mesh: for this reason, in the following only uniform mesh are used.

2.4.2 - *RESEARCH FOR THE BEST MESH*

The sensitivity analysis objective is to individuate the finest mesh that brings to the most accurate results with the least mistakes. 15-16 million is the greatest number of elements that the PCs and the meshing software used for this study allow: the limitations are due to the computers' processors (reals and virtual) and the CPU.

Once the maximum number of elements is identified, it is necessary to choose the mesh parameters on SimVascular meshing section. In particular, the parameters relative to the boundary layers are the same as the ones in the uniform mesh case of the previous paragraph:

- Portion of Edge Size: 0.60
- Number of Layers: 3
- Layer Decreasing Ratio: 0.60.

Only a parameter has to be changed in order to impose the number of mesh elements and it is the Global Max Edge Size (GMES). We started with a GMES of 0.0415 that brought to a 13.9 million elements.

The chosen discretization must have another important characteristic in order to be effectively the best mesh: it has to avoid the deformation of the different surfaces of the model. The 13.9 million mesh overcomes (the element size is very small, so there are no problems in fitting the model's figure) this control.

At this point, it is necessary to create a set composed by several meshes with the aim of reducing computational times without affecting the simulations results.

2.4.3 - *COMPARISON BETWEEN DIFFERENT DISCRETIZATIONS*

The set of meshes consists of 9 different discretization starting from the best mesh and reducing the number of elements from 13.9 to 2 million with steps of 1.5 (±0.1). The objective is to find the best compromise between results accuracy and reliability and computational time. The mesh parameters used are the same of the previous sections: the changes have been made in the GMES, quantity that specify the dimension of the created elements. Thanks to GMES variations it has been possible to try different discretization with several number of elements. The final 9 mesh attempts are reported in Figure 29.

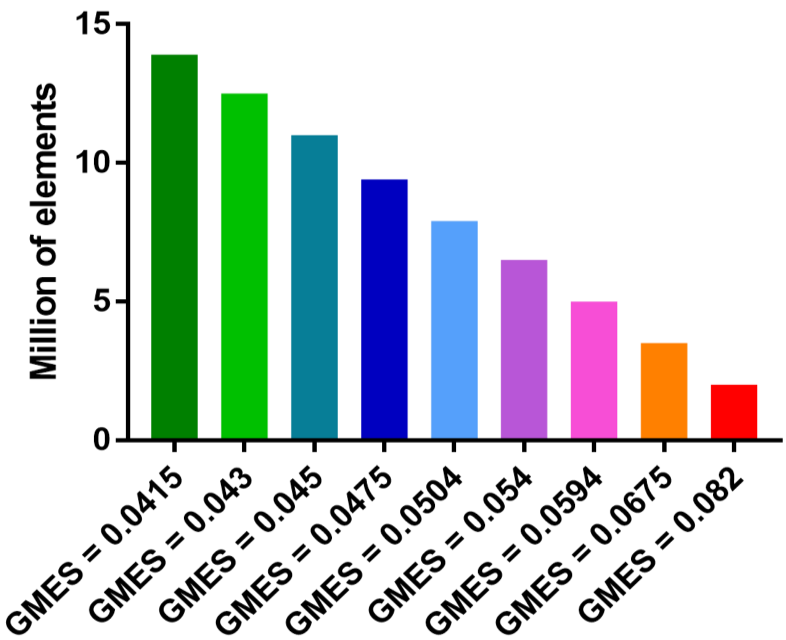

Figure 29 - GMES x Number of elements

Once created all these meshes, a steady state simulation for each one of them has been run: the solver set parameters imposed is the same used in the best flow extension research, as shown in Table 3.

Computational times of these simulations vary a lot depending on the number of mesh elements: it is possible to pass from relatively short times (about 40 hours for 2 million model) to extremely long durations that last for some weeks. This problem involves the finest meshes and it has been overcome looking at the variations of outlet flows in the initial time steps of the simulations: it is noticed that already at the 10th time step for each attempt the simulation reaches a stability because the fluxes in all the following time steps vary less than the 1%. For this reason, the simulations of the meshes with a larger number of elements (the ones with more than 7.9 million of elements) are stopped at the 40th time step (the stability is already reached) and the results considered for the final analysis and comparison belong to the 20th time step. For each discretization WSS magnitude and pressure distributions [dyne/cm^2] are computed on the surfaces of the model and are reported in Figure 30 and Figure 31 respectively.

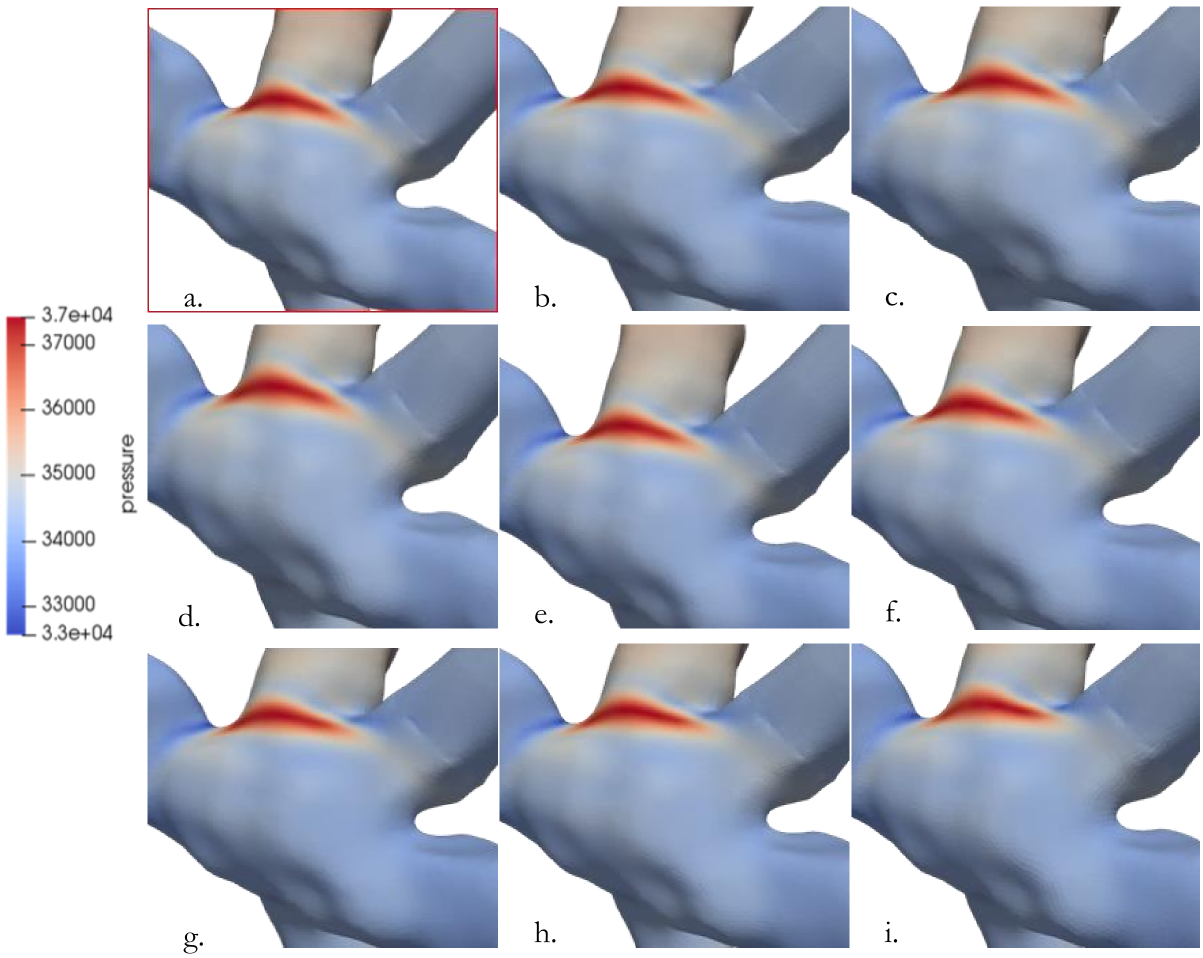

Figure 30 - Pressure distribution [dyne/cm^2] for each mesh: a. best mesh (13.9M), b. 12.5M, c. 11M, d. 9.4M, e. 7.9M, f. 6.5M, g. 5M, h. 3.5M, i. 2M

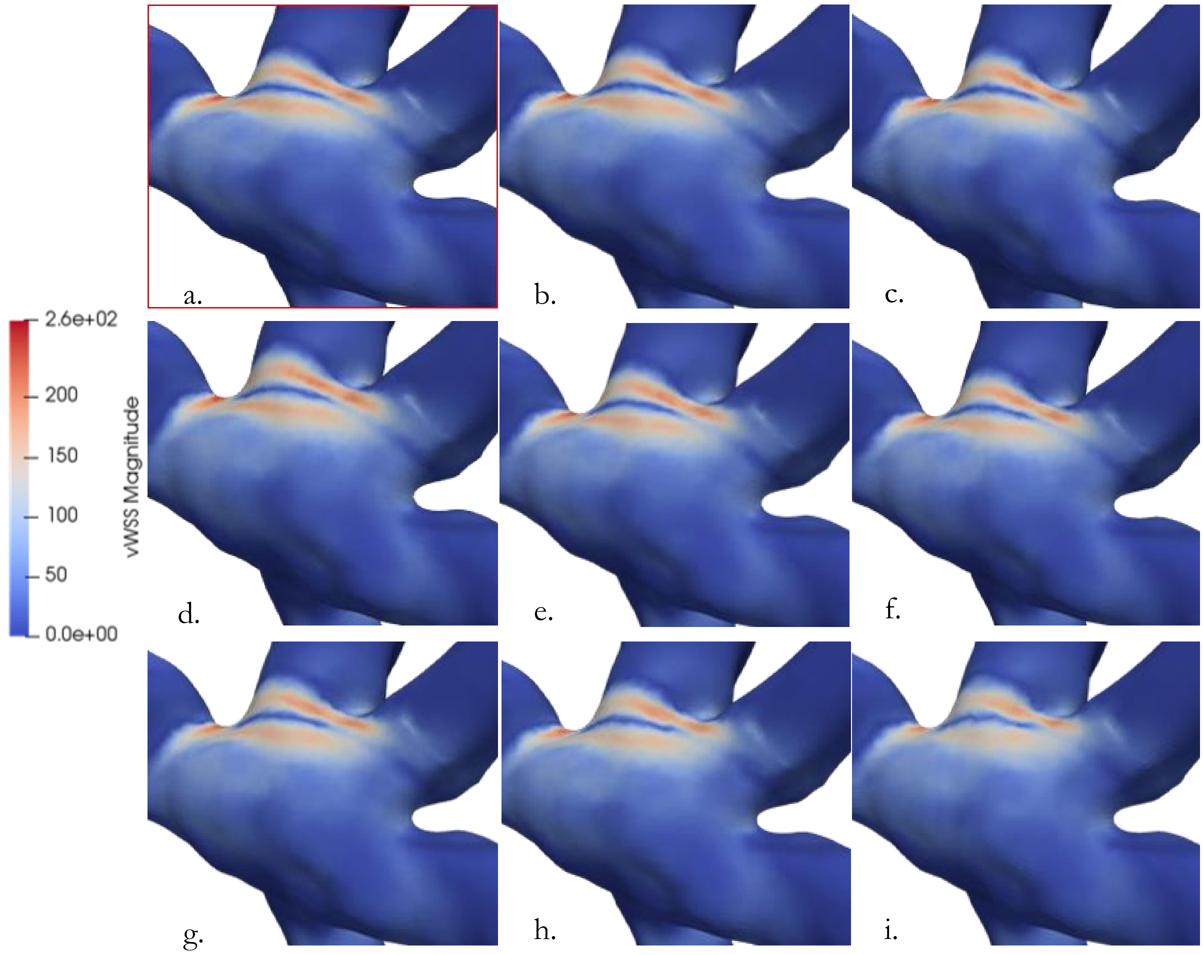

Figure 31 - WSS magnitude distribution [dyne/cm2] for each mesh: a. best mesh (13.9M), b. 12.5M, c. 11M, d. 9.4M, e. 7.9M, f. 6.5M, g. 5M, h. 3.5M, i. 2M

After this visual comparison, a statistical analysis is made in order to quantify the different behaviour of the discretization set respect to the best mesh. For each mesh four principal statistical parameters are computed using a Pyhton script for pressure, WSS and velocity: mean values, standard deviation, kurtosis and skewness. For each statistical quantity, the percentage differences are calculated considering the best mesh as a reference model: in this way it is possible to compare the different pressure, WSS and velocity distributions in a quantitative way. In Table 11, it is possible to see the statistical values of the best mesh. In the following, Table 12, Table 13, Table 14 and Table 15 represent respectively mean, standard deviation, kurtosis and skewness values.

MODEL		WSS (dyne/cm²)	PRESSURE (dyne/cm²)	VELOCITY (cm/s)
13.9M	mean value	14.151	34378.048	18.531
	standard dev	21.661	400.338	2.441
	kurtosis	25.425	6.291	1.642
	skewness	4.356	1.800	16.523

Table 11 - Statistical values of the best mesh

MESH		WSS (dyne/cm²)	PRESSURE (dyne/cm²)	VELOCITY (cm/s)
2M	mean value	13.543	34359.881	17.557
	% difference	-4.300%	-0.053%	-5.258%
3,5M	mean value	13.919	34368.214	17.858
	% difference	-1.642%	-0.029%	-3.634%
5M	mean value	14.014	34370.911	18.036
	% difference	-0.972%	-0.021%	-2.671%
6,5M	mean value	14.109	34377.148	18.193
	% difference	-0.298%	-0.003%	-1.827%
7,9M	mean value	14.293	34379.573	18.338
	% difference	1.004%	0.004%	-1.043%
9,4M	mean value	14.193	34377.086	18.393
	% difference	0.296%	-0.003%	-0.748%
11M	mean value	14.129	34376.897	18.434
	% difference	-0.157%	-0.003%	-0.525%
12,5M	mean value	14.120	34376.502	18.486
	% difference	-0.219%	-0.004%	-0.245%

Table 12 - Mean values and percentage differences

MESH		WSS (dyne/cm²)	PRESSURE (dyne/cm²)	VELOCITY (cm/s)
2M	standard dev	19.346	387.546	16.229
	% difference	-10.690%	-3.195%	-1.781%
3,5M	standard dev	20.422	393.294	16.363
	% difference	-5.723%	-1.759%	-0.973%
5M	standard dev	20.841	393.723	16.435
	% difference	-3.785%	-1.652%	-0.535%
6,5M	standard dev	21.105	399.863	16.482
	% difference	-2.569%	-0.119%	-0.250%
7,9M	standard dev	21.490	400.414	16.500
	% difference	-0.789%	0.019%	-0.144%
9,4M	standard dev	21.572	399.813	16.514
	% difference	-0.411%	-0.131%	-0.059%
11M	standard dev	21.577	399.218	16.507
	% difference	-0.388%	-0.280%	-0.100%
12,5M	standard dev	21.552	398.901	16.510
	% difference	-0.506%	-0.359%	-0.081%

Table 13 - Standard deviations and percentage differences

MESH		WSS (dyne/cm²)	PRESSURE (dyne/cm²)	VELOCITY (cm/s)
2M	kurtosis	21.476	7.629	2.854
	% difference	-15.533%	21.278%	16.921%
3,5M	kurtosis	22.331	6.783	2.690
	% difference	-12.170%	7.834%	10.174%
5M	kurtosis	23.050	6.637	2.636
	% difference	-9.343%	5.501%	8.000%
6,5M	kurtosis	23.429	6.341	2.572
	% difference	-7.851%	0.809%	5.344%
7,9M	kurtosis	23.651	6.234	2.527
	% difference	-6.977%	-0.894%	3.523%
9,4M	kurtosis	24.670	6.279	2.471
	% difference	-2.969%	-0.179%	1.211%
11M	kurtosis	25.106	6.311	2.461
	% difference	-1.255%	0.318%	0.808%
12,5M	kurtosis	25.317	6.373	2.458
	% difference	-0.423%	1.312%	0.703%

Table 14 - Kurtosis and percentage differences

MESH		WSS (dyne/cm²)	PRESSURE (dyne/cm²)	VELOCITY (cm/s)
2M	skewness	4.003	1.977	1.726
	% difference	-8.095%	9.851%	5.138%
3,5M	skewness	4.099	1.863	1.693
	% difference	-5.884%	3.496%	3.142%
5M	skewness	4.165	1.839	1.682
	% difference	-4.375%	2.195%	2.489%
6,5M	skewness	4.190	1.820	1.669
	% difference	-3.807%	1.145%	1.664%
7,9M	skewness	4.209	1.790	1.660
	% difference	-3.365%	-0.553%	1.118%
9,4M	skewness	4.297	1.801	1.649
	% difference	-1.339%	0.040%	0.436%
11M	skewness	4.335	1.801	1.646
	% difference	-0.478%	0.060%	0.273%
12,5M	skewness	4.350	1.806	1.645
	% difference	-0.125%	0.327%	0.232%

Table 15 - Skewness and percentage differences

However, attention is focused only on the most important parameter: the mean value. It is necessary to impose a percentage error threshold under which the results are considered acceptable and over which the meshes are rejected. For this reason, a histogram is made: in Figure 32 the meshes are ordered from the one with less element to the finest one. The first discretization that have errors below the 5% threshold can be considered acceptable for the continuation of this work because it lasts also for the shortest computational time.

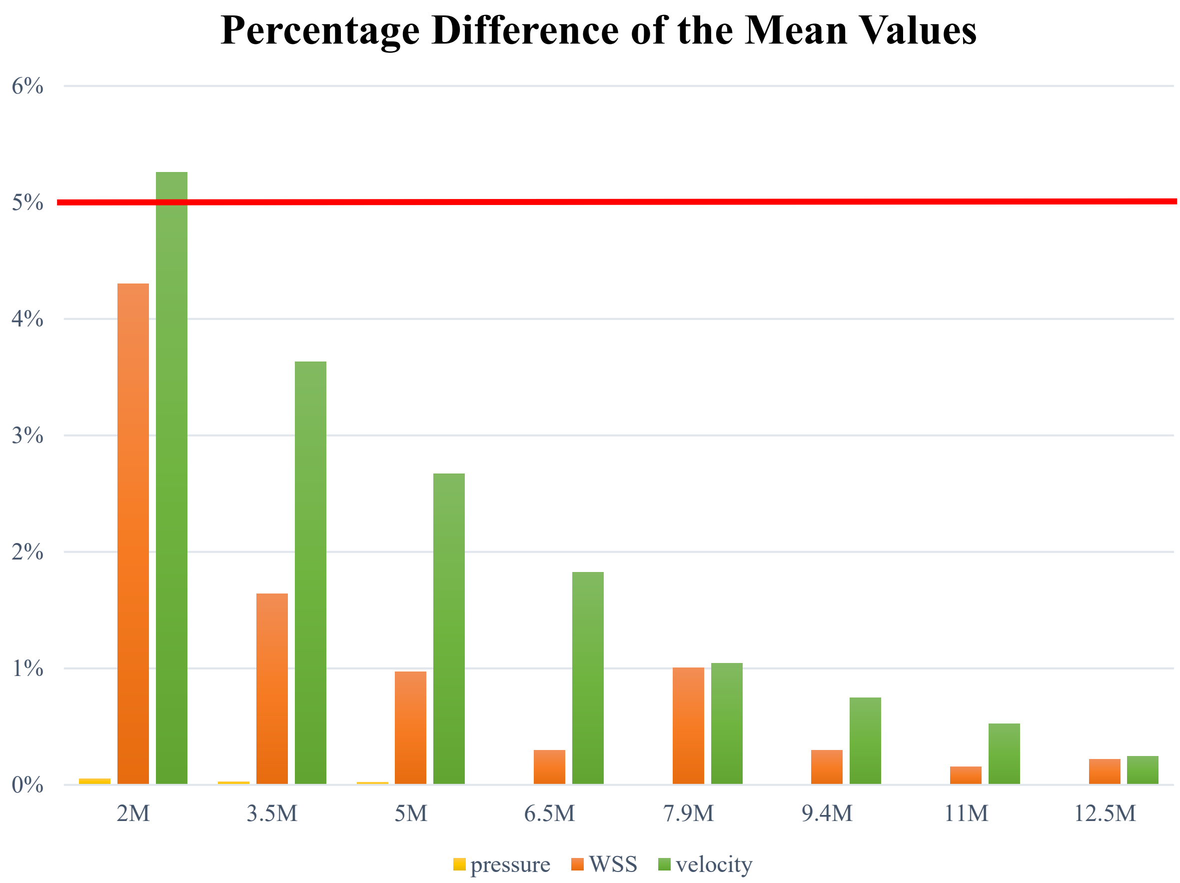

Figure 32 - Comparison between mean values' percentage differences

As it is possible to see in Figure 32, the first discretization that remains under the threshold for all the parameters under study (pressure, WSS and velocity) is the one with 3.5 million of elements: this mesh is the most indicated to be used in the next unsteady simulations, but, before drawing this conclusion, another comparison is necessary.

The last step of this sensitivity analysis is another comparison, but this time the distributions are studied following the number of points for each value: the objective is to see if the trend of the different meshes is comparable to the best mesh's one. The following graphs are obtained thanks to Matlab software that allow to compute the distribution of a set of values into a number of classes (decided by the user). This calculation is done for the set of values relative to pressure, WSS magnitude and velocity distributions: obviously, for each case a normalization on the total number of points of the mesh is done in order to make the results comparable. Figure 33 represents the trend of pressure, WSS magnitude and velocity for the best mesh, while the next figures report the comparison between the mesh in study (in blue) and the best one (in red).

a.

b.

c.

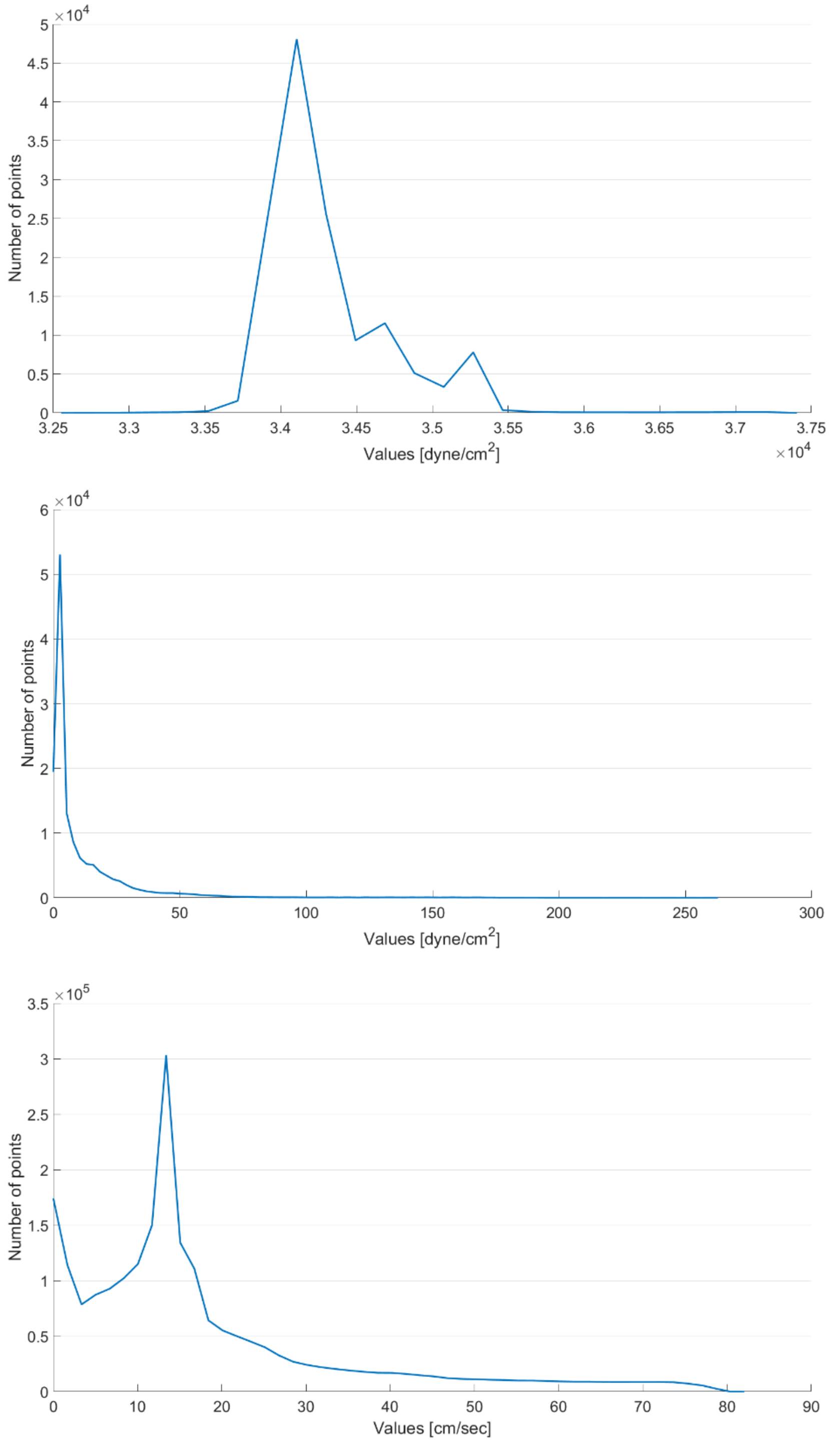

Figure 33 - Values-number of points distributions for the best mesh: a. pressure; b. WSS magnitude; c. velocity

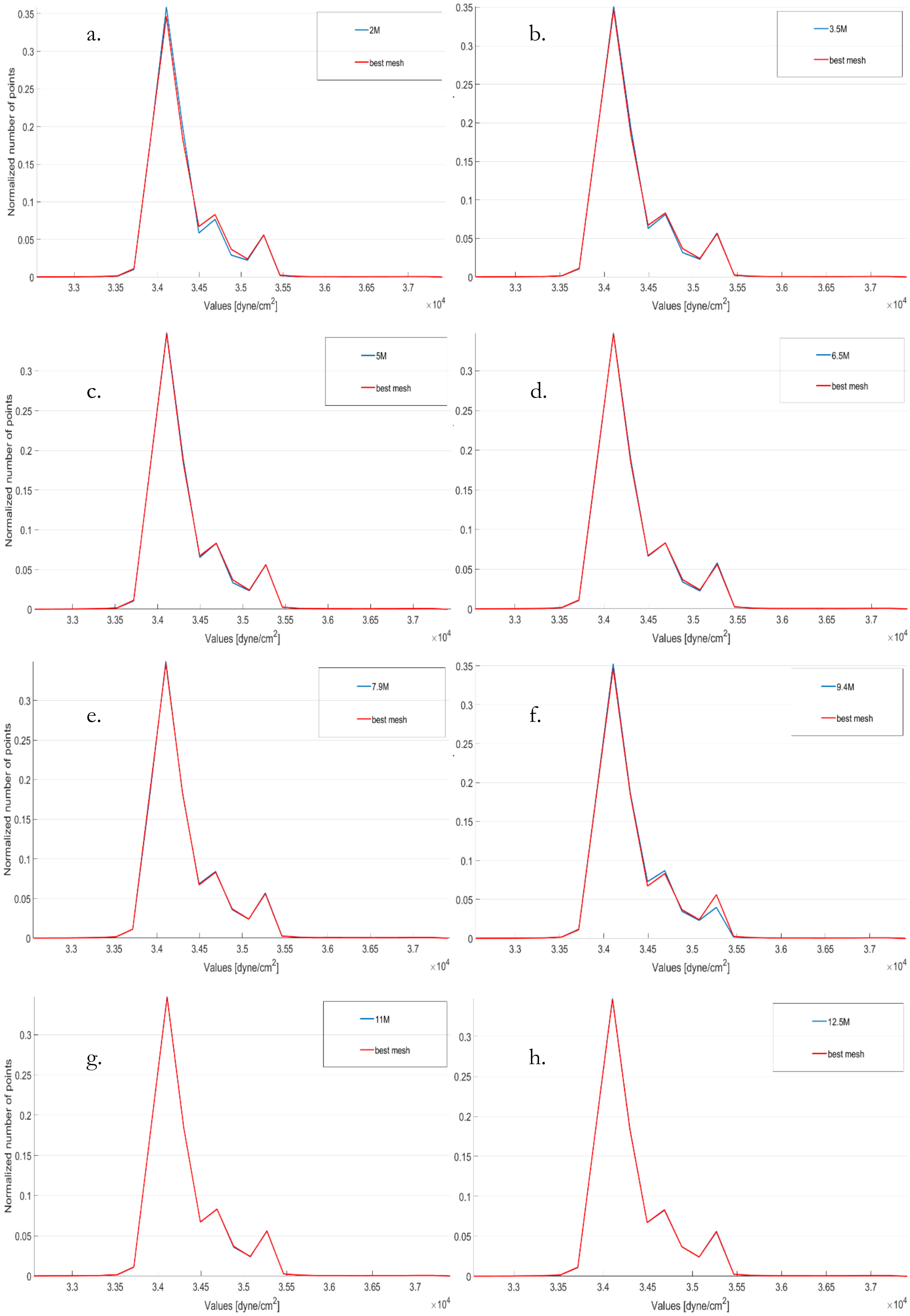

Figure 34 - Pressure values-number of points distributions: a. 2M; b. 3.5M; c. 5M; d. 6.5M; e. 7.9M; f. 9.4M; g. 11M; h. 12.5M

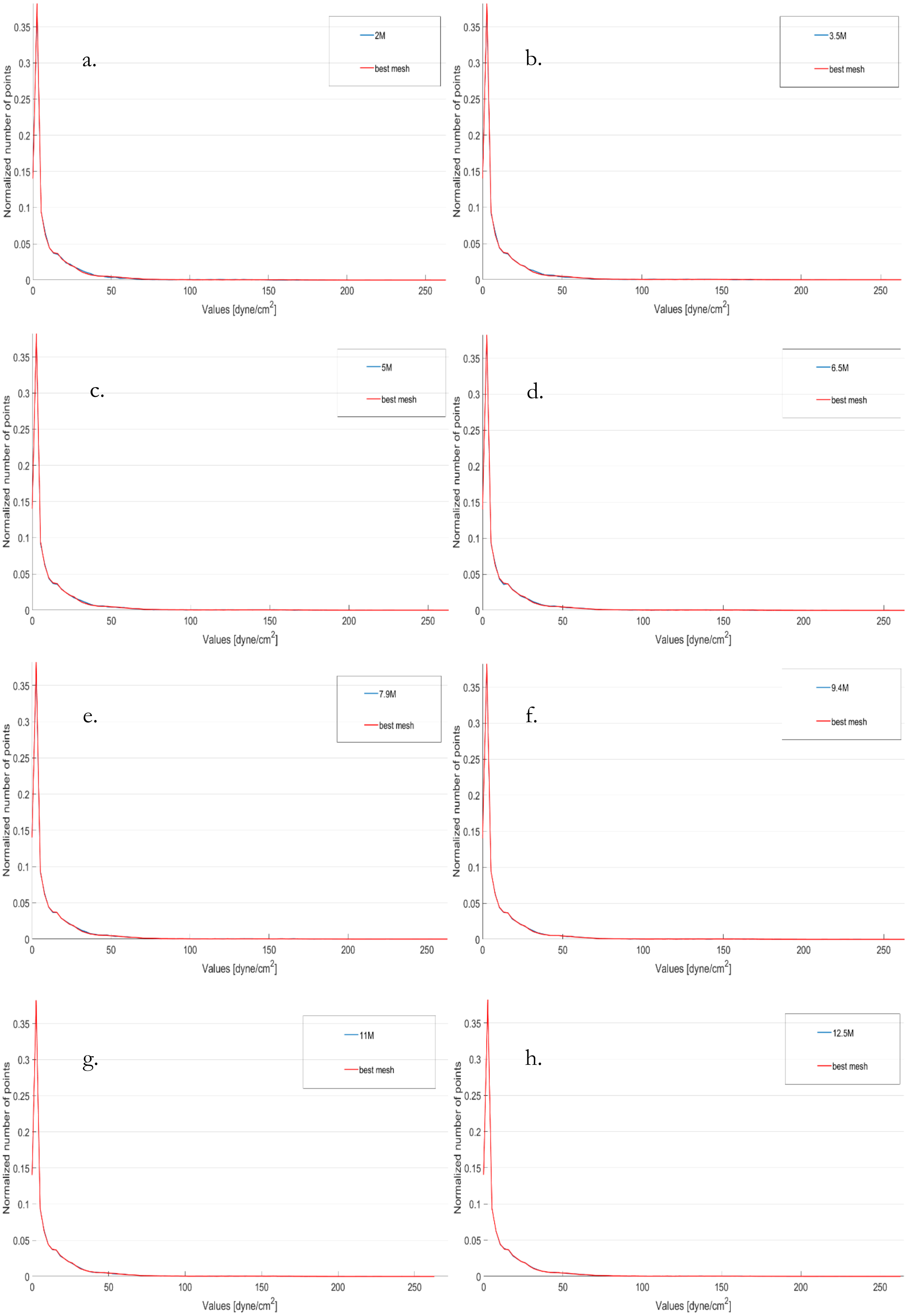

Figure 35 – WSS magnitude values-number of points distributions: a. 2M; b. 3.5M; c. 5M; d. 6.5M; e. 7.9M; f. 9.4M; g. 11M; h. 12.5M

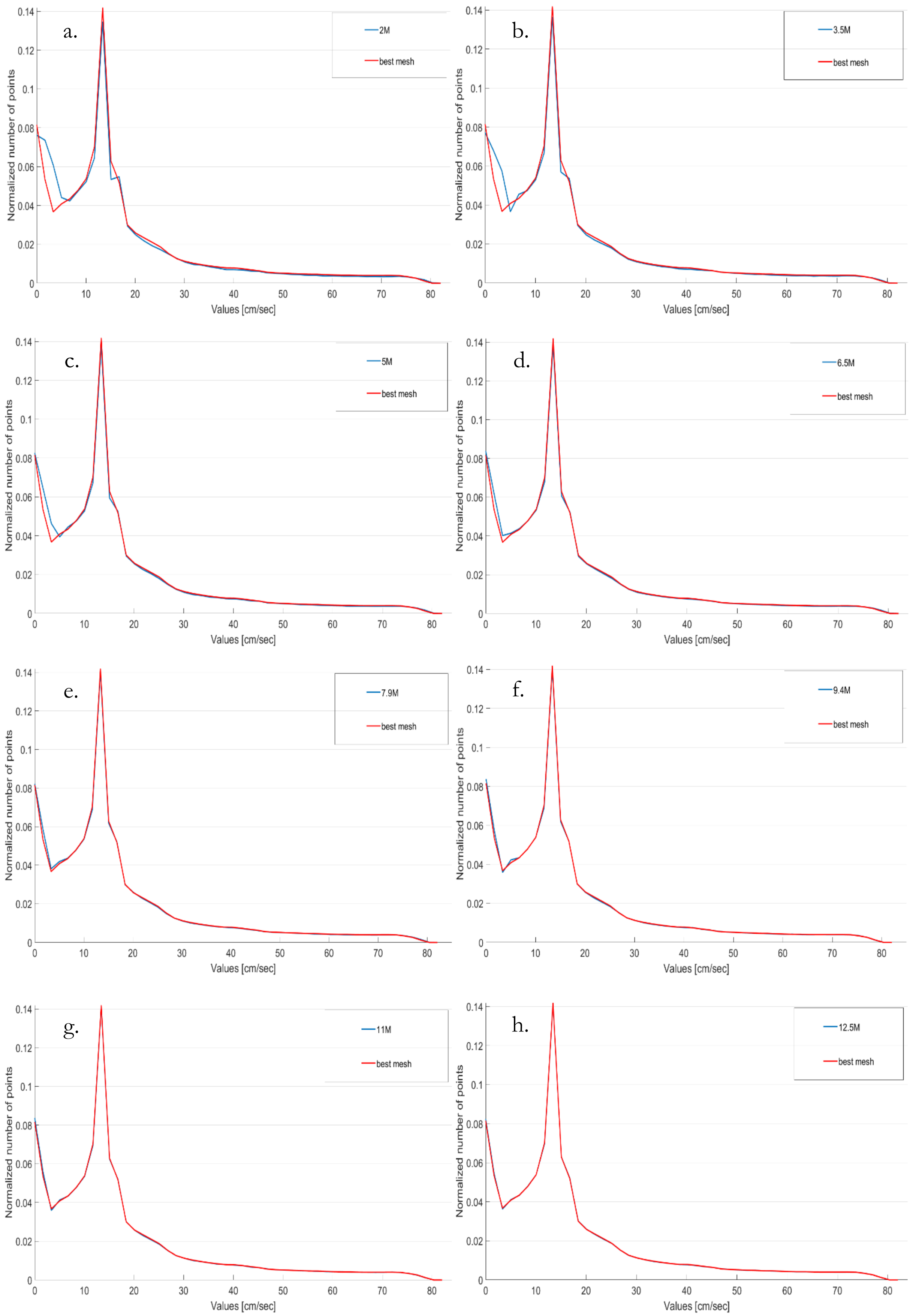

Figure 36 - Velocity values-number of points distributions: a. 2M; b. 3.5M; c. 5M; d. 6.5M; e. 7.9M; f. 9.4M; g. 11M; h. 12.5M

In Figure 35, it is possible to see a very similar behaviour in WSS distribution between all the tested meshes: the blue and the red lines are always overlapping. Little differences are shown in Figure 34 and Figure 36, especially in the discretization with a lower number of elements: however, in pressure distributions, the differences decrease with the 3.5M case, that describes very well the best mesh trend, despite the coarser mesh. Velocity distributions are the most variable: in Figure 36, it is appreciable the improvement of the trend with the increasing of elements' number and it is possible to say that only the meshes from 7.9M elements are precisely overlapping the red line. The other meshes differ from the best one especially in the part before the peak, but the trend is similar enough.

For these reasons, the final comparison doesn't reverse the preference of the statistical analysis: so, it is possible to conclude that the mesh that allows to have a remarkable gain in computational time and a good approximation of the best mesh results is the 3.5M discretization. This mesh will be used in all the following simulations.

Chapter 3 – Methodology: Unsteady Simulations

The objective of this part is to obtain different input velocity profiles to impose them at the venae cavae (VC) inlets, evaluating the effects on the haemodynamic of a patient-specific post Fontan procedure three-dimensional model. Results will be analysed in the next chapter, while in this one the different steps that bring to the construction and the following solution of the simulations are described.

All simulations have been performed on SimVascular and the model used for each case has 5x flow extensions and the relative discretization is the uniform mesh with a Global Max Edge Size of 0.0675.

3.1 - PARAMETERS FOR UNSTEADY SIMULATIONS

In the following, new boundary conditions in inflows and outflows and an optimal set of solver parameters will be specified for the unsteady simulations.

3.1.1 - *INFLOW BOUNDARY CONDITIONS*

Since patient specific data of this patient were not available, inlet flow rates at venae cavae were obtained scaling the 4D-MRI of a 4-years old patients treated with Fontan procedure, according to inlet sections. Figure 37 shows the in vivo measured VC velocity.

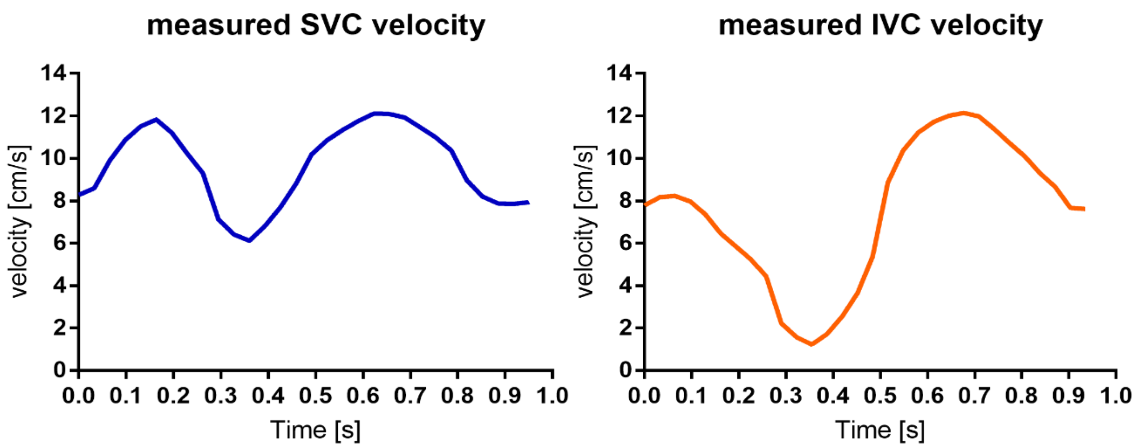

Figure 37 - In vivo velocity data

In particular, flow rates were scaled on our model with different steps:

- in this study walls were considered rigid, so the mean value of the area during the cycle is calculated and the relative diameter (with the hypothesis that the inlet surface is circular);
- from these data (inlet surface area and flow rate) it is possible to calculate the Reynolds number (Re), according to the equation described in Chapter 2. The result is considered the same also for the model of this study and from this value the computation of the quantities of interest started;
- assuming the same Re for the patient of this study and that the inlet area (and so the diameter) of this study model is known, thanks to an inversion of Re formula it is possible to calculate the new mean velocity for each time instant;
- the last step consists of the calculation of the incoming VC's blood flow through the formula $Q = A\boldsymbol{v}$.

All these steps must be repeated for both SVC and IVC data. At the end it is possible to obtain behaviour in time of the SVC and IVC flows as shown in Figure 38: here the data have been rescaled on 1 second cycle using the Fourier series computed through a Python script.

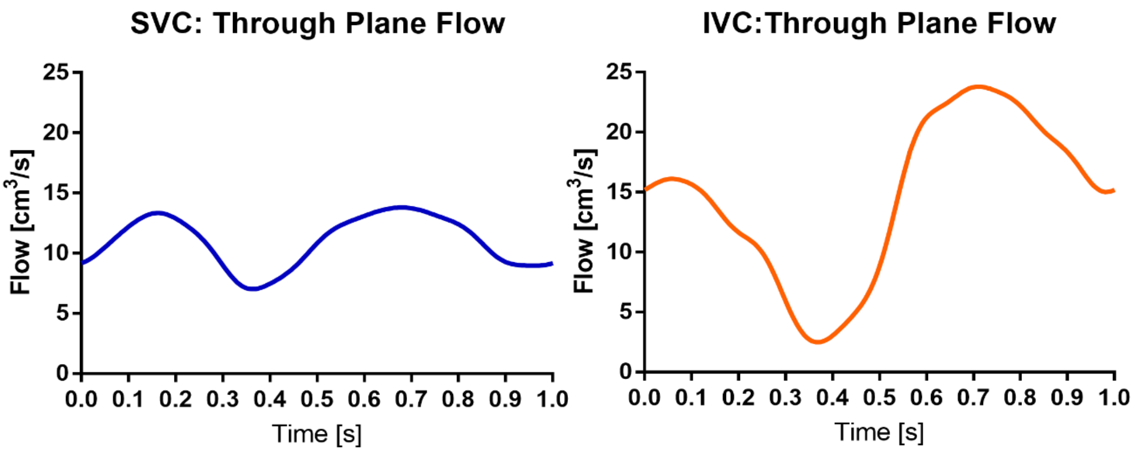

Figure 38 - Imposed inlet flows

As a SimVascular convention, the unit vectors normal to inlet and outlets were computed outwards, so for all the inlet flow rates were imposed: two .flow files are created with the values obtained with the steps before and scaled on a period of 1 second directly in SimVascular. These two files contain IVC and SVC flows values and the relative instant and will be given as input once the BCs of unsteady simulation is created.

3.1.2 - *OUTFLOW BOUNDARY CONDITIONS*

Following the same approach of many other works studying the Fontan procedure, a resistive model was chosen as outflow boundary condition. In some articles the PAR (pulmonary arteriolar resistance) value was used to find the resistance of PAs with the equation $R_{RPA} = R_{LPA} = 2 \cdot PAR$ (Migliavacca et al., 2003, 1999; Pietrabissa et al., 1996), while others give directly the values of pulmonary resistances (Chugunova et al., 2019; Dubini, De Leval, Pietrabissa, Montevecchi, & Fumero, 1996; M Grigioni et al., 2003; Pekkan et al., 2005). In any case, the equivalence $R_{RPA} = R_{LPA}$ is always mentioned. In this study because of the presence of two RPA this equivalence is transformed in $R_{LPA} = R_{equivalentRPA}$, where $R_{equivalentRPA} = \frac{1}{\frac{1}{R_{RPA1}} + \frac{1}{R_{RPA2}}}$.

articles/citations	PAR values	R_{RPA}= R_{LPA} [mmHg/(L/min)]	R_{RPA}= R_{LPA} [dyn·s/cm^5]
(Migliavacca et al., 2003)	1	2	160
(Migliavacca et al., 2003)	3	6	480
(Migliavacca et al., 2003)	4	8	640
(Migliavacca et al., 1999)	1.48	2.96	236.8
(Migliavacca et al., 1999)	0.83	1.66	132.8
(Pietrabissa et al., 1996)	1.62	3.24	259.2
(Dubini et al., 1996)	/	3.24	259.2
(Pekkan et al., 2005)	/	1.5	120
(Pekkan et al., 2005)	/	3	240
(Chugunova et al., 2019)	/	2.9	232

Table 16 - Literature pulmunary resistance values

In order to have a resistance value that derives from all these literature contributions, a mean value is calculated excluding the ones that include interatrial TCPC and idealized model with offset between the two VC (Pekkan et al., 2005): Table 16 reports the values considered for the final computation. At the end of this consideration, the final value is 276 dynes·second/cm^5. This value is imposed as LPA boundary condition in SimVascular simulation parameters: for the RPAs Split Resistance option is selected and the software compute automatically the RPA1 and RPA2 resistances from their $R_{equivalentRPA}$, imposing the Murray's coefficient = 3. The final values for PAs boundary conditions are

- R_{LPA}= 276 dynes·second/cm^5
- R_{RPA1}= 569.927 dynes·second/cm^5
- R_{RPA2}= 535.167 dynes·second/cm^5.

3.1.3 - *SOLVER PARAMETERS*

After the definition of boundary conditions for inlets and outlets, it was necessary to choose the right solver parameters in order to ensure the stability of the convergence of numerical solution.

PARAMETER	VALUE
Number of Timesteps	400
Time Step Size	0.005
Number of Timesteps between Restarts	1
Step Construction	40
Residual Criteria	0.0001
Tolerance on Momentum Equations	0.0001
Tolerance on Continuity Equations	0.001
Tolerance on svLS NS Solver	0.001
Time Integration Rule	Second Order

Table 17 - Solver parameters

Table 17 reports the most important parameters for the simulation that were varied to obtain the best combination. The first three concern the timesteps: the total simulation time is imposed to 2 seconds (400 timesteps*0.005 seconds) in order to overcome the initial conditions effect with the 2nd cycle and the time step size value is a good compromise between accuracy and computational costs. Moreover, it is imposed that a single was created at each timestep, having 400 restarts files at the end.

Another important consideration has to be done about the choice of residual criteria: when the residue goes under this value, the simulation can go on to the next timestep because the solution is sufficiently stable. If the residue value is greater than 0.0001, the simulation remains at the same time instant until 40 repetitions (Step Construction in Table 17) have been made until this value goes under the threshold imposed. Same speech must be done for non-linear solver tolerances.

At the end, the order of time integration in case of unsteady simulations is the second.

3.1.4 - *BASELINE SIMULATION: TP VELOCITY*

A first simulation was performed in order to check the quality of the chosen solver parameters: it lasted for less than 3 days and it reached convergence quickly enough. A second attempt was done with modified SVC and IVC boundary conditions: rather than a parabolic profile of the velocity in the inlets sections, it's preferred a Womersley profile (while the behaviour in time it's the same reported in Figure 38).

Womersley's formulation (Womersley, 1955) expresses the velocity profile at any cross-section for an unsteady, laminar flow of an incompressible fluid of density ρ and constant viscosity μ through a straight pipe of constant radius R, when time varying pressure gradient is available at any instant of time t. The velocity profile is expressed in terms of the coefficients of the complex Fourier series of the pressure gradient along the tube (Das et al., 2011; Womersley, 1955). Womersley type for velocity profiles (Womersley, 1955) have been used in numerical computations of blood flows in other pathophysiologies (Ryval, Straatman, & Steinman, 2004) and is considered a better approach for applying velocity boundary conditions as compared to a simplified profile such as spatially uniform or parabolic at any instant of time of a pulse cycle (Das et al., 2011).

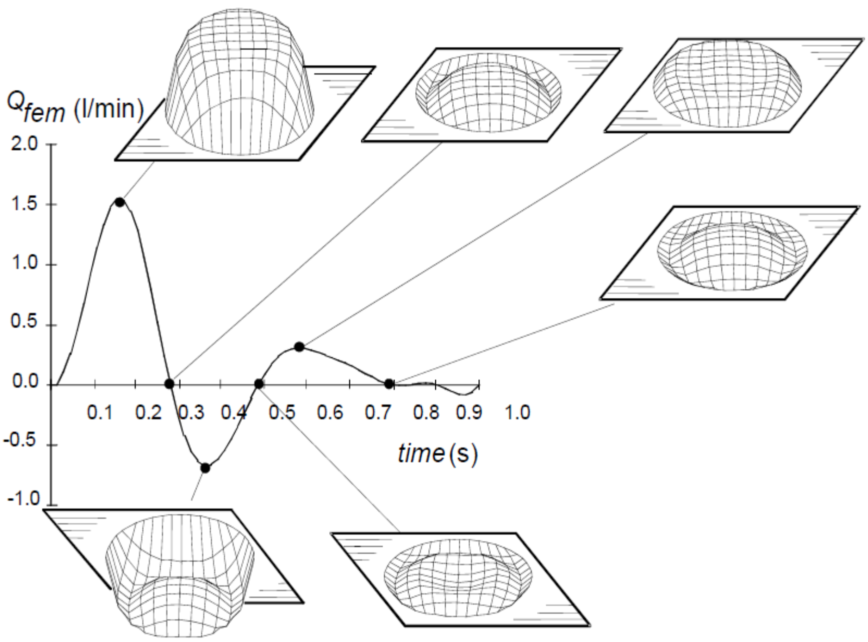

Figure 39 - Womersley flow profile in a femoral artery

An example of a Womersley profile is reported in Figure 39 in which it is possible to see the 3D waveform and the behaviour in time of blood flow in femoral artery: the profile isn't completely parabolic and that in some instants the peripheral laminae are involved in a reversal flux respect to the central part.

This type of profile is imposed in the boundary condition of SVC and IVC because considered more similar to reality: the advantage of Womersley profile over simplistic velocity profiles such as spatially constant or parabolic type is that it is able to capture the flow reversal at walls and therefore, is a more realistic boundary condition for pulsatile flows than the simplistic profiles.

So, the second simulation was performed with the previous solver parameters: it lasted for about 60 hours and it went to a stable convergence: Figure 40 shows the outflows behaviour in this case, considering only the second cycle.

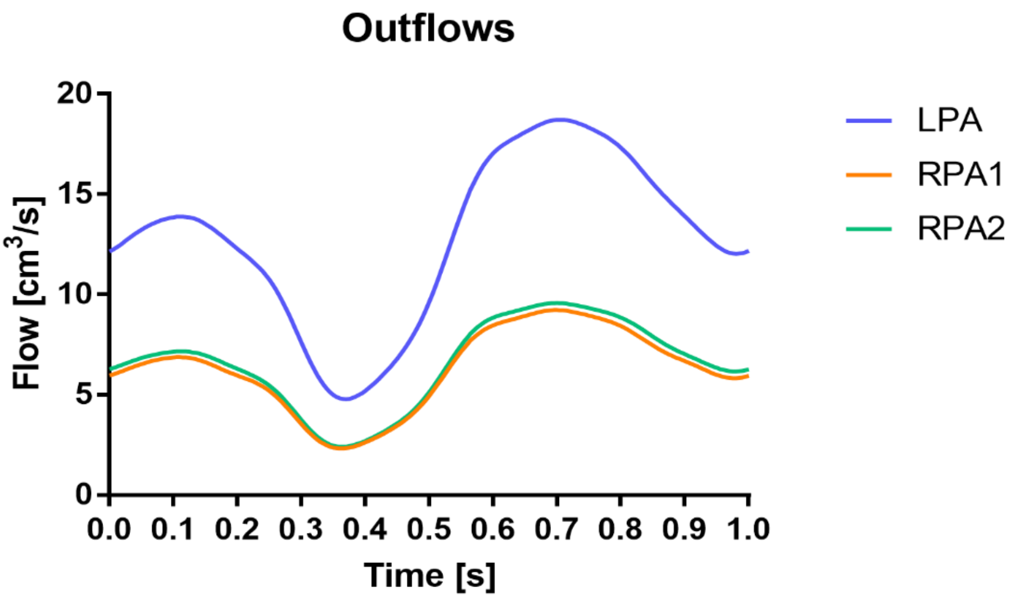

Figure 40 - Baseline outflow in time

This simulation has only the axial velocity component with a Womersley profile (imposed in the BCs of the inlets), that from now on it will always be called through plane velocity (TP velocity): in this case only the axial velocity is present, while in the next paragraph the secondary profiles will be introduced. Because the principal aim of this study is to evaluate the secondary flows effect on this patient specific model and to try to understand the quality of this Fontan procedure, in the next profiles some secondary velocities will be studied and sum to the TP component that remains the one descripted and used in this section. For these reasons this simulation and all the results referring to it will be called Baseline.

Figure 41 shows a vector representation of baseline's maximum values for SVC and IVC.

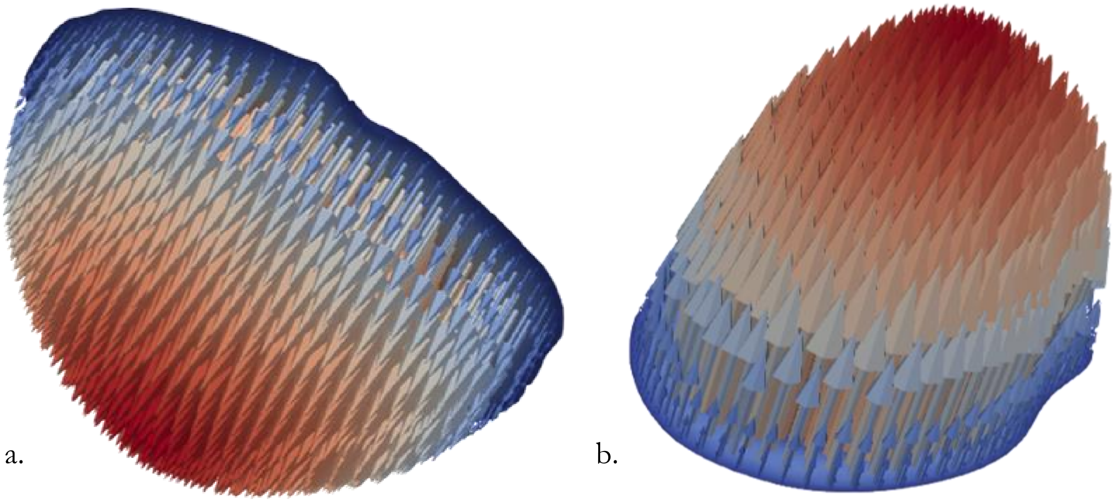

Figure 41 - Baseline TP velocity maximum value: a. SVC; b. IVC

3.2 - SECONDARY FLOWS VELOCITY PROFILES

The principal aim of this thesis is the investigation of different patterns velocity in the venae cavae flow as boundary condition and its role in modification of haemodynamic descriptors: the methodology used is a generation of different idealized, analytical based, velocity profiles to be imposed as inlet boundary condition in the patient specific model.

In-plane velocity profiles were analytically obtained through a Python script through which it was possible to do all the geometric computations required: IP velocity has to fit the surface on which it is applied, so it is computed for SVC and for IVC separately.

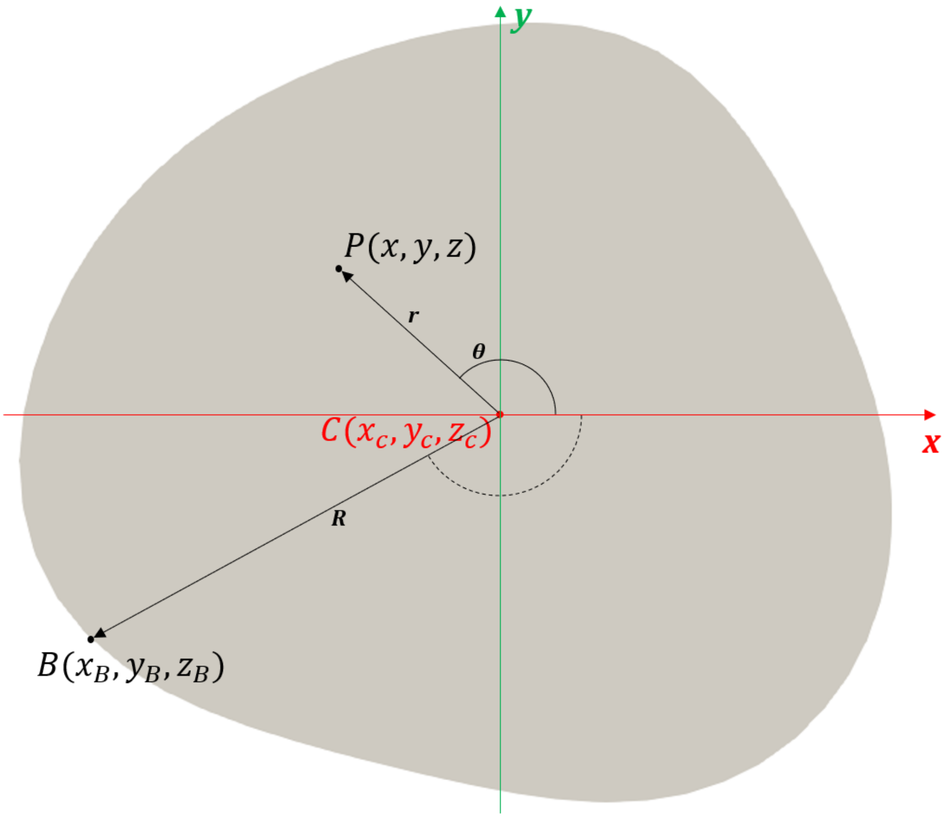

Figure 42 - IP velocity fitting the surface

To fit the velocity profile on a not circular cross section area the script is able to identify the centre **C** of the inlet surface, the points on the boundary, like **B**, and **P** is a generic point on the surface. Each point on the surface is identified with a radial and an angular component (**r**, **θ**), defined with the following formulas

$r = \sqrt{(x - x_C)^2 + (y - y_C)^2 + (z - z_C)^2}$ and $\theta = arctan2(\frac{y - y_C}{x - x_C})$.

In addition, an adaptive radius $\mathbf{R}(\boldsymbol{\theta})$ is calculated which depends on the angular component because the vessel surface isn't perfectly circular. The angular and radial unit vectors were computed too.

All these quantities allow to go on with the computation: IP velocity is composed by the sum of a radial velocity component and an angular one. Here the generalized in-plane velocity Dean equations are reported:

$$\boldsymbol{v_{IP}}(r,\theta) = \boldsymbol{v_r}(r,\theta) + \boldsymbol{v_{an}}(r,\theta)$$

$$\begin{cases} \boldsymbol{v_{an}}(r,\theta) = \left\{A \cdot \left[1-\left(\frac{r}{R}\right)^2\right]\left[4-23\left(\frac{r}{R}\right)^2+7\left(\frac{r}{R}\right)^4\right]\cos(\theta+\alpha) + B\cdot\left(\frac{r}{R}\right)\left[1-\left(\frac{r}{R}\right)^2\right]\right\}\boldsymbol{u_\theta} \\ \boldsymbol{v_r}(r,\theta) = \left\{C \cdot \left[1-\left(\frac{r}{R}\right)^2\right]^2\left[4-\left(\frac{r}{R}\right)^2\right]\sin(\theta+\alpha) + D\cdot\left(\frac{r}{R}\right)\left[1-\left(\frac{r}{R}\right)^2\right]\right\}\boldsymbol{u_r} \end{cases}$$

Parameters A, B, C, D and α are constants that the user chooses on the basis of which pattern of velocity distribution he wants. It is possible to obtain one vortex that covers the whole inlet section, two opposite vortices or other distributions.

The blood flow becomes a 3D motion, with fluxes on the orthogonal section of the vessels: imposing secondary flows is like to impose an equilibrium lack between pressure, viscous and centrifugal forces (Dean, 1928). This imbalance causes the presence of Dean vortices on the transverse cross-section of the vessel (the inlet surface), as it is possible to see in Figure 43. Dean vortices are symmetric, but they induce a displacement of the velocity peak.

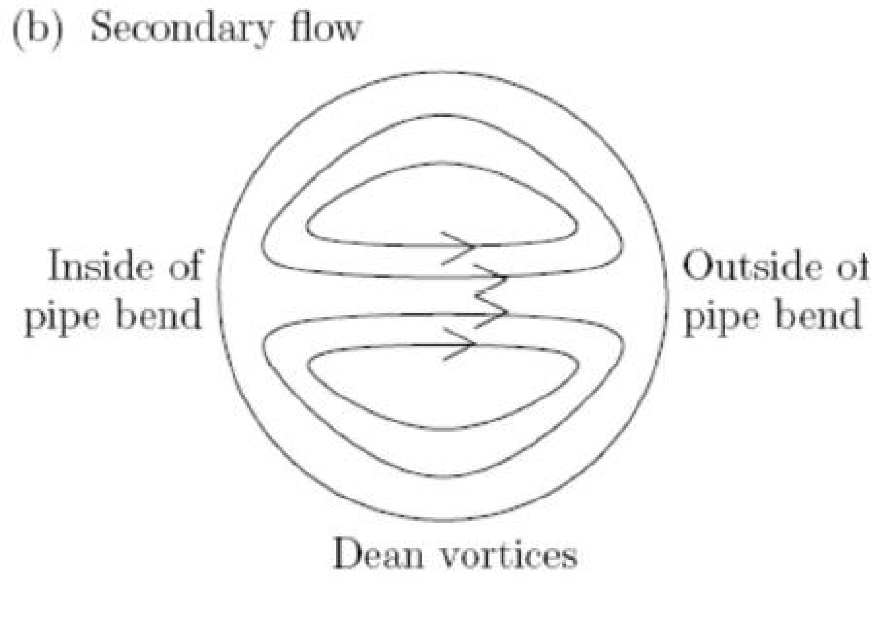

Figure 43 - Formation of Dean vortices

The set of different velocity profiles this thesis wants to analyse is composed by two different distribution:

- Two Dean Vortices, obtained with
  - A = -1
  - B = 0
  - C = -1
  - D = 0
  - $\alpha = 0$

  In this way the system of velocities equations becomes

$$\begin{cases} \boldsymbol{v_{an}}(r,\theta) = \left\{-\left[1-\left(\frac{r}{R}\right)^2\right]\left[4-23\left(\frac{r}{R}\right)^2+7\left(\frac{r}{R}\right)^4\right]\cos(\theta)\right\}\boldsymbol{u_\theta} \\ \boldsymbol{v_r}(r,\theta) = \left\{-\left[1-\left(\frac{r}{R}\right)^2\right]^2\left[4-\left(\frac{r}{R}\right)^2\right]\sin(\theta)\right\}\boldsymbol{u_r} \end{cases}$$

- One Vortex, obtained with
  - A = 0
  - B = 5
  - C = 0
  - D = 1
  - $\alpha = 0$

  In this way the system of velocities equations becomes

$$\begin{cases} \boldsymbol{v_{an}}(r,\theta) = \left\{5\cdot\left(\frac{r}{R}\right)\left[1-\left(\frac{r}{R}\right)^2\right]\right\}\boldsymbol{u_\theta} \\ \boldsymbol{v_r}(r,\theta) = \left\{\left(\frac{r}{R}\right)\left[1-\left(\frac{r}{R}\right)^2\right]\right\}\boldsymbol{u_r} \end{cases}$$

As it is possible to see form these formulas, IP velocity depends only on geometrical factors of the surface of interest and on parametric constants. At this point the IP velocity is normalized for each direction (x, y, z) respect to the mean value of its magnitude: these three normalized components are then multiplied by the TP values obtained from the Fourier series (SVC or IVC data scaled on 1 second) and by the fraction of TP velocity that the user choose as magnitude of IP velocity.

Two fractions of TP velocity were used: 1/3, that corresponds to a 33% of axial component, and 2/3, that stays for 66% of axial component. Figure 44 shows the behaviour in time of the three different magnitude compared, that are TP velocity, IP33 (in-plane velocity with a magnitude that is the 33% of the TP one) and IP66 (in-plane velocity with a magnitude that is the 66% of the TP one).

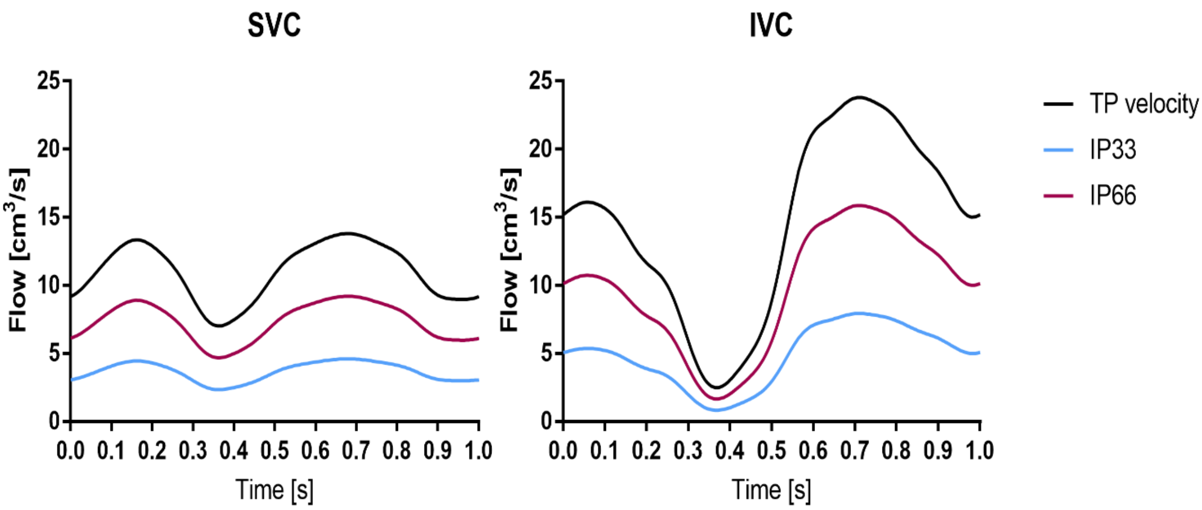

Figure 44 - Different inflow imposed in time

At the end, an array is created with all the computed values for the three directions of IP velocity for each point of the surface in each time instant: this array is mapped onto the correspondent inlet surface of interest visualizable in Paraview.

The following figures show the in-plane vectors visualizations in Paraview of IP velocity for SVC and IVC profiles at 0.025 s.

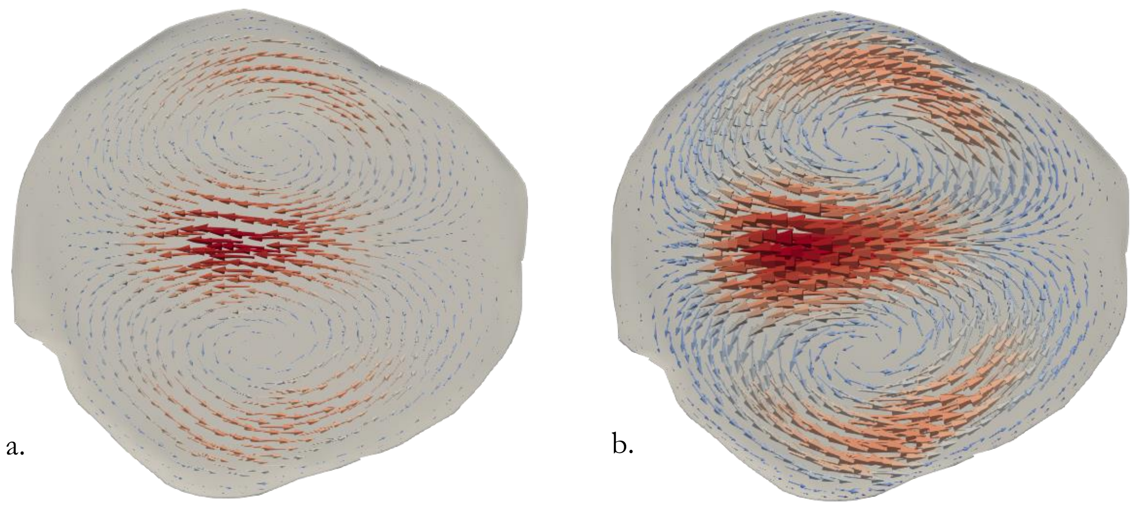

Figure 45 - SVC in-plane velocity with double vortex profiles: a. IP33; b. IP66

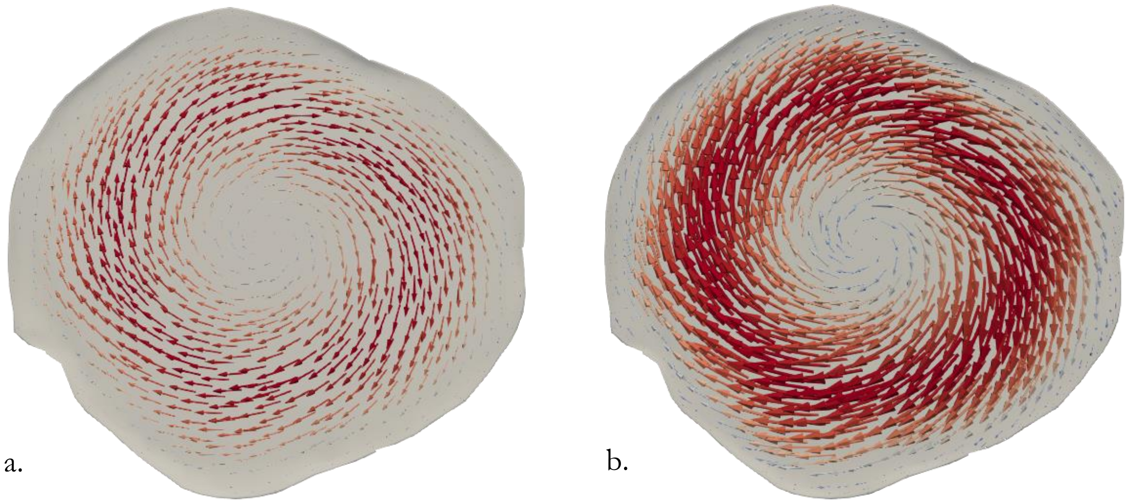

Figure 46 - SVC in-plane velocity with single vortex profiles: a. IP33; b. IP66

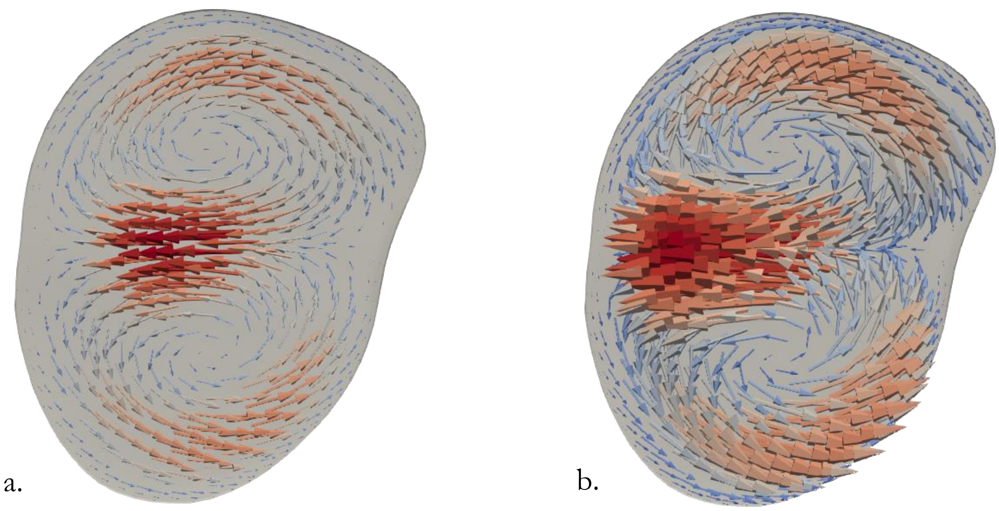

Figure 47 - IVC in-plane velocity with double vortices profiles: a. IP33; b. IP66

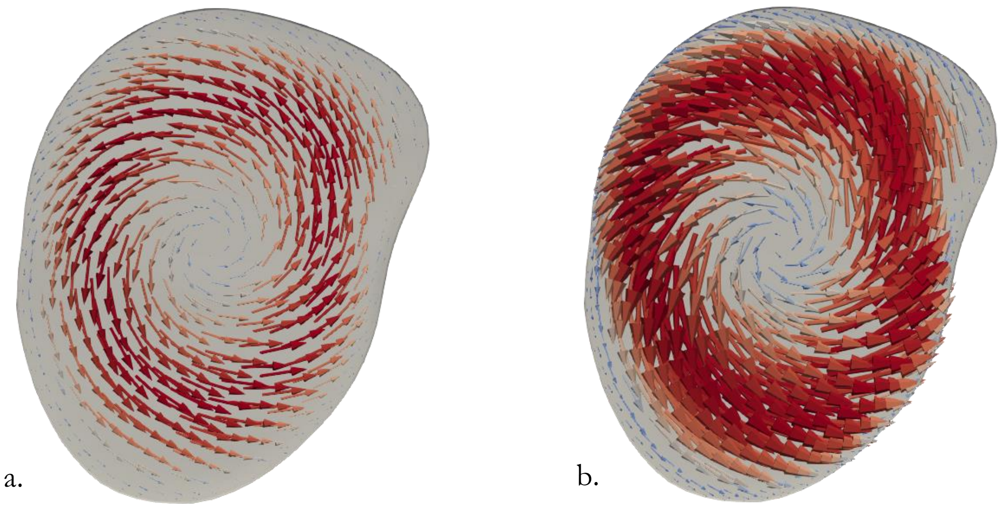

Figure 48 - IVC in-plane velocity with double vortices profiles: a. IP33; b. IP66

3.2.1 - *NEW BCT FILES CONSTRUCTION: TP + IP VELOCITY*

At this point, for each velocity profile a file .vtp is made for each VC: however, in order to do a new boundary conditions file, it is necessary to merge the two IP files. The VMTK software allows this operation by the mean of *vmtksurfaceappend* script: the output will be another .vtp file with both the SVC and IVC surface and their velocity IP data. The final velocity waveforms that have to be the new inlets boundary conditions are the sum of TP and IP profiles: a new Python script is made to load in a new VTK array the final velocity data. The input files of this script are the bct.vtp file coming from the Baseline simulation that contains the TP information, the new IP .vtp file with both SVC and IVC merged surface and the IP data and the .txt file (because has already the time discretization in time-step).

The final total velocity was $V_{TOT} = V_{IP} + V_{TP}$ and it was inserted in the new boundary conditions file of the relative simulation. In this way SimVascular had all the updated information to perform the unsteady simulations with the same resistive outlets' boundary conditions and the same solver parameters as the ones used for the baseline case. In the following, the different cases will be identified on basis of IP velocity profiles as:

- Baseline (as said in the previous paragraph)
- IP33 Double Vortex
- IP66 Double Vortex
- IP33 Single Vortex
- IP66 Single Vortex.

Next figures show Paraview vector visualizations of the final total velocities of SVC and IVC for each case at time 0.025 second.

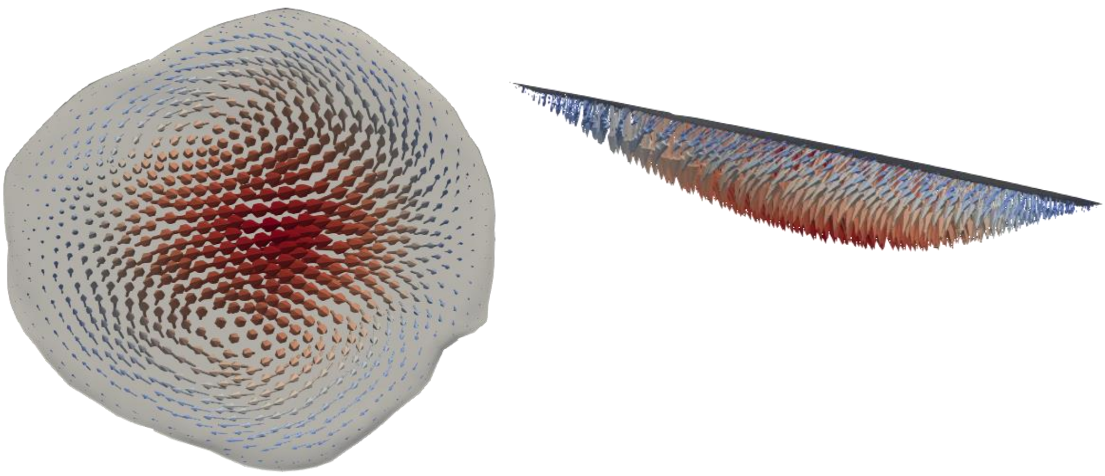

Figure 49 - Two visualizations of SVC final velocity in IP33 Double Vortex case

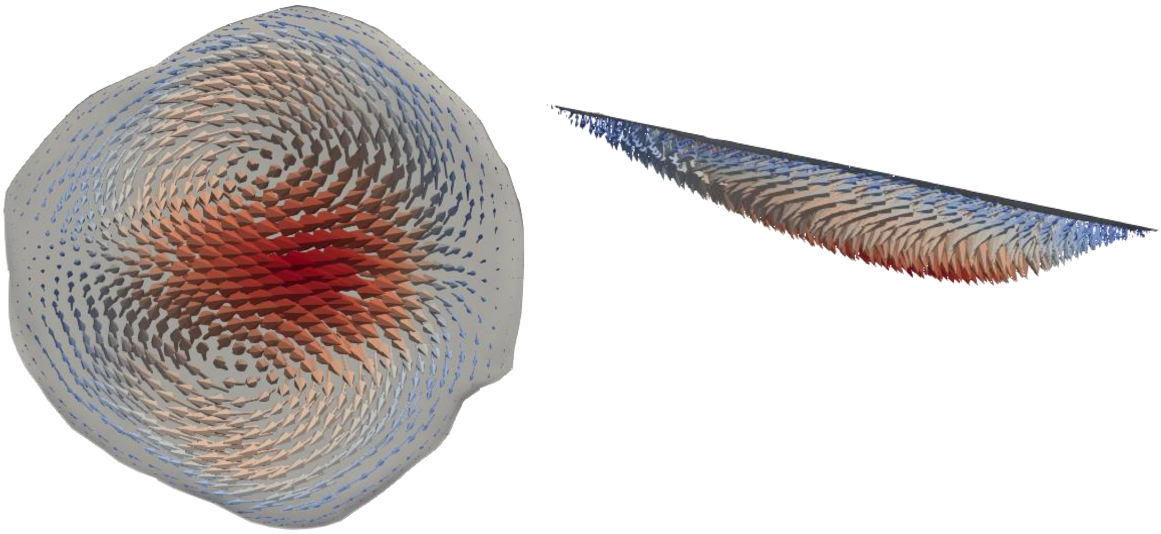

Figure 50 - Two visualizations of SVC final velocity in IP66 Double Vortex case

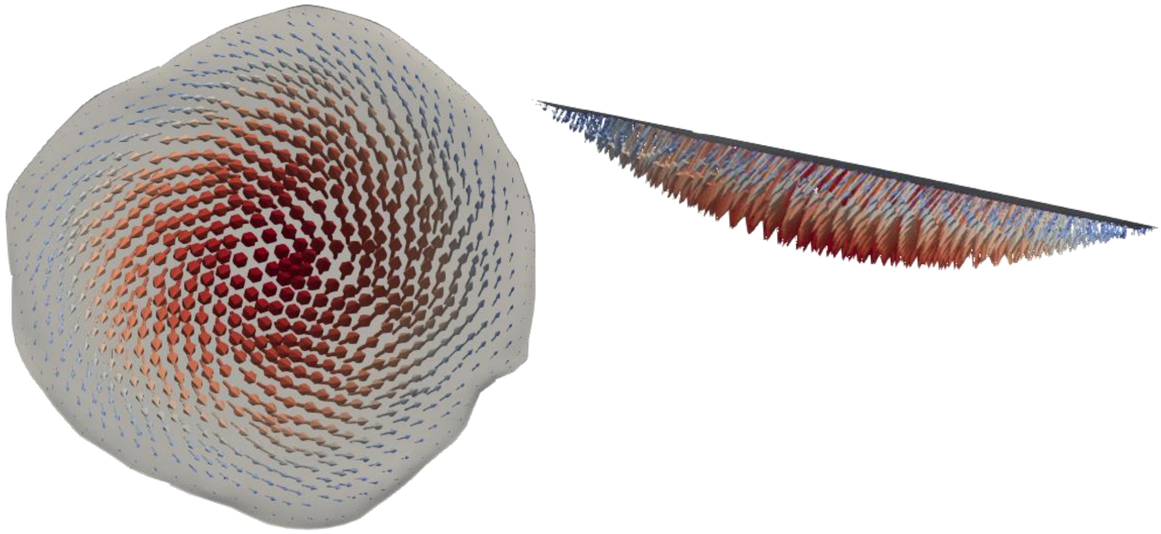

Figure 52 - Two visualizations of SVC final velocity in IP33 Single Vortex case

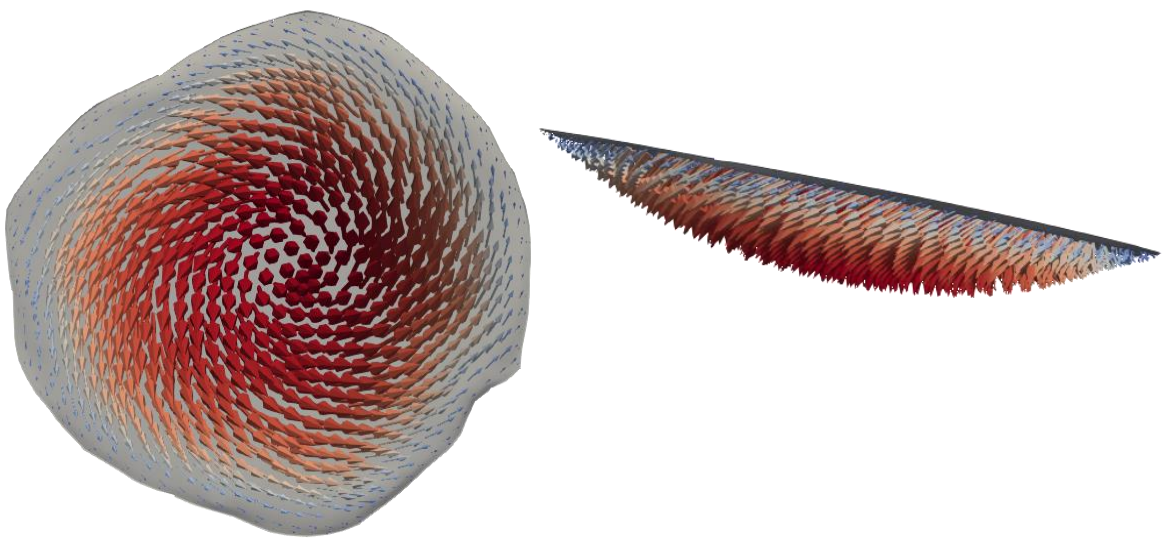

Figure 51 - Two visualizations of SVC final velocity in IP66 Single Vortex case

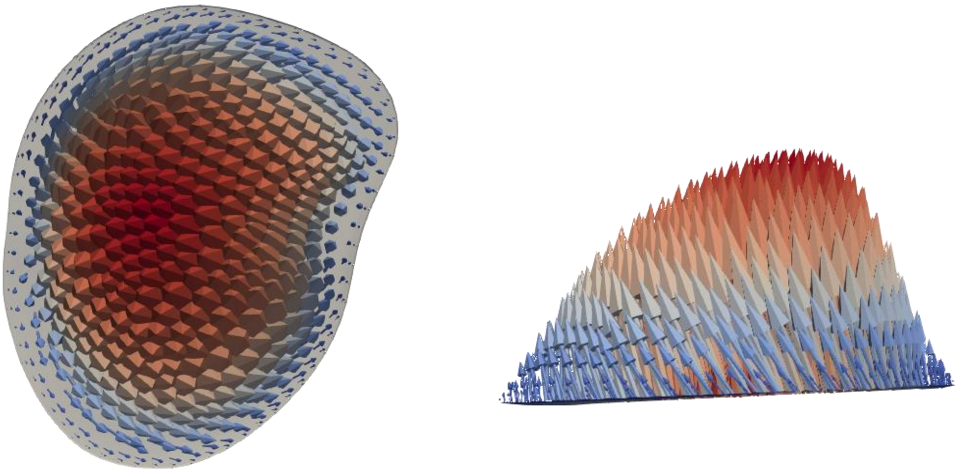

Figure 53 - Two visualizations of IVC final velocity in IP33 Double Vortex case

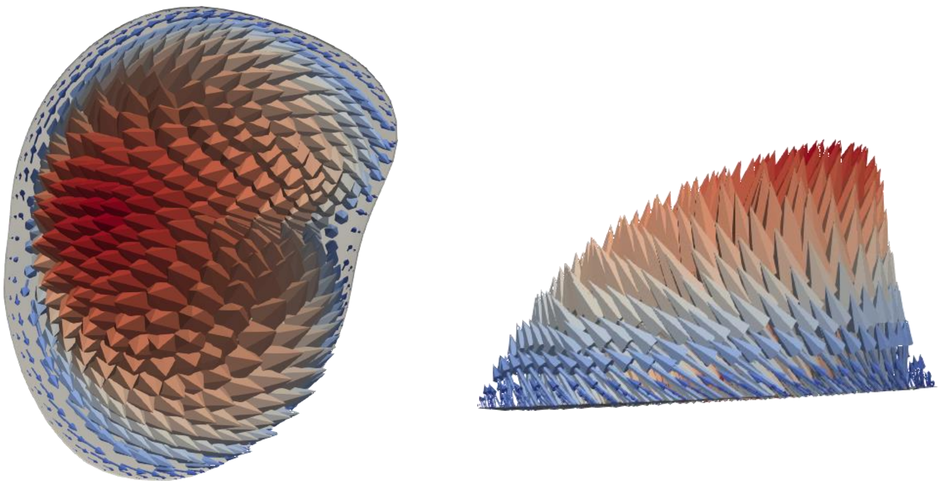

Figure 54 - Two visualizations of IVC final velocity in IP66 Double Vortex case

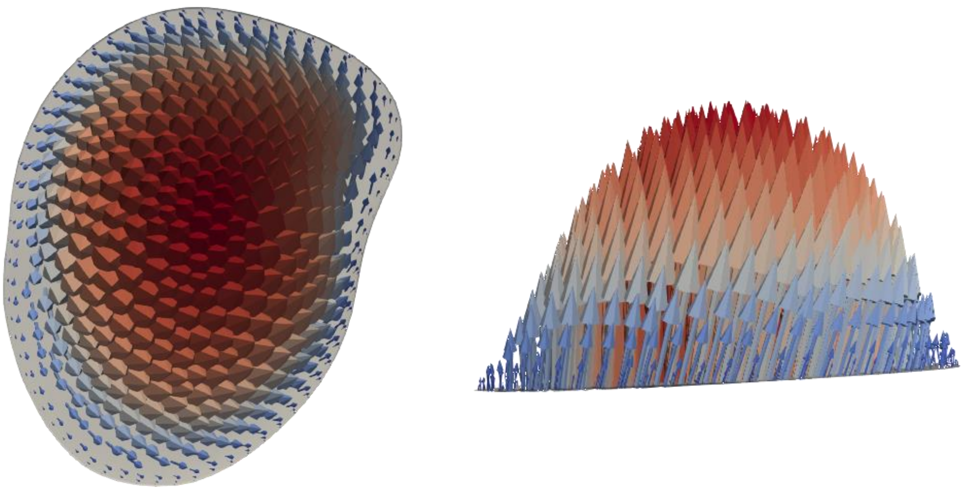

Figure 55 - Two visualizations of IVC final velocity in IP33 Single Vortex case

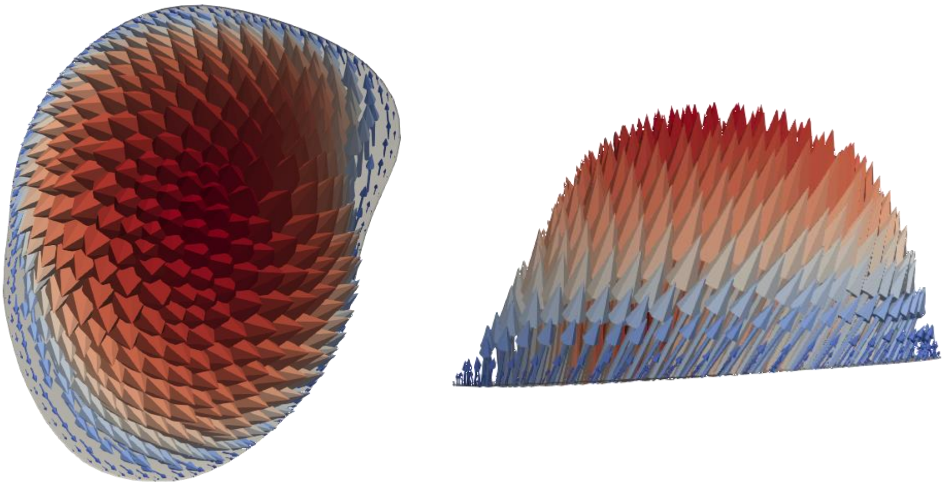

Figure 56 - Two visualizations of IVC final velocity in IP66 Single Vortex case

3.3 - HAEMODYNAMIC INDICES

3.3.1 - *WSS-BASED DESCRIPTORS*

WSS-based descriptors are surface indices that show the disturbed flow into a structure of vessels like Fontan one: they highlight the role playing by haemodynamic forces on the vessel wall, that can cause the generation and proliferation of atherosclerotic plaques, thrombosis or hyperplasia. This disease is influenced by disturbed flow whose indicator functions are related to WSS and its variations, normal pressure gradient and others (Morbiducci, 2017b).

The role played by wall shear-stress is fundamental: low WSS and the resultant stagnation of blood permit increased uptake of atherogenic blood particles (Glagov et al., 1988; Shaaban & Duerinckx, 2000) and both low and oscillatory (that means that changes direction and modulus during cardiac cycle) patterns of WSS cause intimal wall thickening (Ku, 1985; Moore, Xu, Glagov, Zarins, & Ku, 1994; Pedersen, Agerbaek, Kristensen, & Yoganathan, 1997). Moreover, in areas with disturbed flow, endothelial cells experience low or oscillatory WSS and they look polygonal without a clear orientation, with a lack of organization and a better permeability to different substances (Malek & Alper, 1999; Morbiducci, 2017b).

To consider critical factors, such as low mean shear stress and marked oscillations in WSS direction, the distributions at the vessel wall of WSS-based metrics must be computed.

TAWSS

Time-Averaged Wall Shear Stress (TAWSS) is an index that consists of an integration in time of the WSS magnitude and it is a quantity that varies in space (with model points): it evaluates the total shear stress exerted on the wall throughout a cardiac cycle (Pinto & Campos, 2016). TAWSS descriptor is calculated by integrating each nodal WSS vector magnitude at the luminal surface:

$$TAWSS = \frac{1}{T}\int_0^T |\boldsymbol{WSS}(\boldsymbol{s},t)|dt$$

in dynes/cm² (Morbiducci et al., 2010) and with WSS magnitude computation as

$$|\boldsymbol{WSS}(\boldsymbol{s},t)| = \sqrt{WSS_x{}^2 + WSS_y{}^2 + WSS_z{}^2}$$

The reference values are

- low TAWSS values (lower than 4 dynes/cm²) stimulate a proatherogenic endothelial phenotype (Gallo, Steinman, Bijari, & Morbiducci, 2012; Malek & Alper, 1999; Morbiducci, 2017b);
- moderate TAWSS values (about 15 dynes/cm² and greater) induce quiescence and an atheroprotective gene expression profile (Malek & Alper, 1999; Morbiducci, 2017b);
- higher TAWSS values (greater than 100-150 dynes/cm²) can lead to endothelial trauma (Malek & Alper, 1999; Morbiducci, 2017b).

OSI

The second WSS-based descriptor considered for this work is the Oscillatory Shear Index (OSI)(Ku, 1985) and it is used to identify highly oscillating WSS values during the cardiac cycle: as said before, oscillating WSS regions are usually associated with bifurcating or secondary flow and vortex formation, conditions strictly related to atherosclerotic plaque formation and fibrointimal hyperplasia (Morbiducci, 2017b).

OSI descriptor is calculated by the following formula:

$$OSI = 0.5\left[1 - \left(\frac{|\int_0^T \boldsymbol{WSS}(\boldsymbol{s},t)dt|}{\int_0^T |\boldsymbol{WSS}(\boldsymbol{s},t)|dt}\right)\right]$$

with $0 \leq OSI \leq 0.5$ (Morbiducci et al., 2010).

This index is function of space too: the result will be a value for each model point.

The reference values are:

- low OSI values occur where flow disruption is minimal (Morbiducci, 2017b), approximately about 0;
- high OSI values (with a maximum of 0.5) highlight sites where the instantaneous WSS deviates from the main flow direction in a large fraction of the cardiac cycle (Morbiducci, 2017b) and they can cause intimal thickening (Gallo et al., 2012).

RRT

The last WSS-based descriptor studied is Relative Residence Time (RRT) (Himburg et al., 2004) and it measures how long the particles stay near the wall of the vessel (Pinto & Campos, 2016). RRT is recommended as a robust single metric of low and oscillating shear flow because it is proportional to a combination of TAWSS and OSI: in fact RRT is, by definition, the inverse of the magnitude of the time-averaged WSS vector (Lee, Antiga, & Steinman, 2009).

The mathematical formulation is

$$RRT = \frac{1}{(1 - 2 \cdot OSI) \cdot TAWSS} = \frac{T}{\left| \int_0^T \boldsymbol{WSS}(\boldsymbol{s}, t) \cdot dt \right|}$$

in cm²/dynes (Morbiducci et al., 2010).

RRT is an important metric because it identifies the regions with low TAWSS and high OSI, but it hasn't a threshold value under or over which it is acceptable: moreover, it suffers of a bias if TAWSS or OSI value is much higher than the other one.

3.3.2 - *BULK FLOW METRICS*

The study of bulk flow behaviour in unsteady simulations is very interesting: in particular, the geometry of our model with all the branches can affect the flux distribution and division in all the vessels. Moreover, the different velocity profiles imposed in the inlets can induce different behaviour in the middle of the model that will be studied in this section, thanks to some descriptors. Many studies have demonstrated that torsion and curvature contribute to the onset and development of helical patterns in the bulk flow. There is evidence that helical blood flow elicits atheroprotective fluid–wall interaction processes, by limiting flow instabilities within the cardiovascular bed (Morbiducci et al., 2011) and regulates the transport of atherogenic particles at the luminal surface (Liu et al., 2004; Morbiducci et al., 2010).

From a phenomenological viewpoint, an arrangement of the bulk flow in complex helical/vortical patterns might play a significant role in the tuning of the cells mechanotransduction pathways, due to the existence of a relationship between flow patterns and transport phenomena that could affect blood–vessel wall interaction and that can initiate the inflammatory response (Morbiducci, 2017b).

HELICITY AND LNH

A better understanding of the role of pitch and torsion in blood flow development can be obtained through **helicity**, a pseudoscalar eligible to study relationships between complexity and energy (Gallo et al., 2012): like energy, helicity influences evolution and stability of both turbulent and laminar flows (Gallo et al., 2012; Moffatt & Tsinober, 1992).

In addition, helicity is related to the reduction of non-linear processes responsible for transfer and redistribution of energy through various scales, and hence energy dissipation (Gallo et al., 2012; Morbiducci, 2017b).

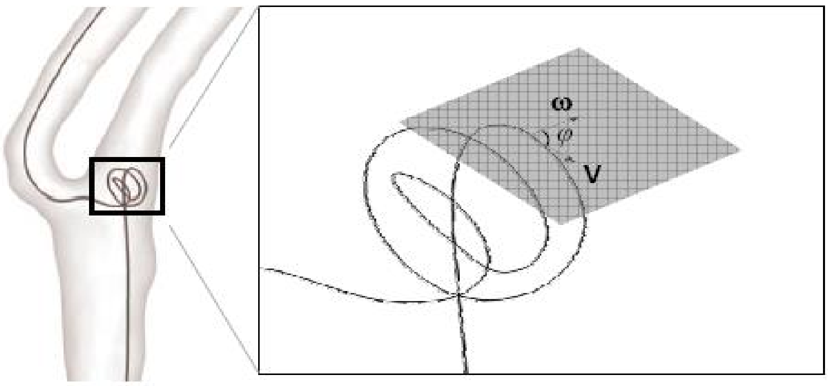

Figure 57 - Vector representation of vorticity and velocity

Before describing the helicity computation, it is necessary to introduce another fundamental quantity: **vorticity** is related to the rotation spin of the fluid and is defined by the following formula

$$\boldsymbol{\omega}(\boldsymbol{s};t) = \nabla \times \boldsymbol{V}(\boldsymbol{s};t) = \begin{pmatrix} \dfrac{\partial v_3}{\partial x_2} - \dfrac{\partial v_2}{\partial x_3} \\ \dfrac{\partial v_1}{\partial x_3} - \dfrac{\partial v_3}{\partial x_1} \\ \dfrac{\partial v_2}{\partial x_1} - \dfrac{\partial v_1}{\partial x_2} \end{pmatrix}$$

where $\boldsymbol{V}(\boldsymbol{s};t) = (v_1, v_2, v_3; t)$ is velocity in time and space. Vorticity is a Galilean-invariant quantity that can also be computed from the vorticity tensor $\boldsymbol{\Omega}$, derived from the Jacobian matrix construction (Günther & Theisel, 2018).

Helicity gives measure of alignment of velocity and vorticity vectors (shown in Figure 57) and it can describes the arrangement of blood streams into complex structures. Now it is possible to define the density of kinetic helicity through

$$h(\boldsymbol{s};t) = \boldsymbol{V}(\boldsymbol{s};t) \cdot \left(\nabla \times \boldsymbol{V}(\boldsymbol{s};t)\right) = \boldsymbol{V}(\boldsymbol{s};t) \cdot \boldsymbol{\omega}(\boldsymbol{s};t)$$

while helicity $\mathrm{H}(t)$ corresponds to the volume integration of $h(\boldsymbol{s};t)$ (Gallo et al., 2012; Moffatt & Tsinober, 1992; Morbiducci, Ponzini, Gallo, Bignardi, & Rizzo, 2013).

To simplify the analysis and visualization of helicity, the Local Normalized Helicity descriptor is introduced by the formula

$$LNH(\boldsymbol{s};t) = \frac{\boldsymbol{V}(\boldsymbol{s};t) \cdot \boldsymbol{\omega}(\boldsymbol{s};t)}{|\boldsymbol{V}(\boldsymbol{s};t)||\boldsymbol{\omega}(\boldsymbol{s};t)|} = \cos\varphi(\boldsymbol{s};t)$$

where $\varphi(\boldsymbol{s};t)$ is the angle between velocity and vorticity vectors (visible in Figure 57); as the cosine function, LNH can assume only values belonging to $-1 \leq LNH \leq 1$ interval and the sign indicates the swirling direction relative to the flow direction (Günther & Theisel, 2018).

H DESCRIPTORS

Integrating helicity density $h(\boldsymbol{s};t)$ over defined time intervals and volumetric fluid domain, it is possible to have a bulk flow characterization in terms of helical content and helical flow topology. These four descriptors allow to obtain a quantitative analysis of helical flow structures strength, size and relative rotational direction.

The first descriptor h_1 is the mean of helicity $H(t)$ in time: this time-averaged value is an integral measure of helical flow accounting for changes in sign of helicity density $h(\boldsymbol{s};t)$. Its mathematical formulation is

$$h_1 = \frac{1}{TV} \int_T \int_V h(\boldsymbol{s};t)\, dV\, dt$$

where T is the considered time interval and V is control volume and h_1 is in cm/s^2. This descriptor can assume the 0 value if the flow arrange in symmetrical counter-rotating helical structures or in case of no helicity (Gallo et al., 2012).

The second descriptor h_2 defines the helicity intensity through the integration of absolute value of $h(\boldsymbol{s};t)$ given by the following formula

$$h_2 = \frac{1}{TV} \int_T \int_V |h(\boldsymbol{s};t)|\, dV\, dt$$

where T is the considered time interval and V is control volume and h_2 is in cm/s^2. It is an indicator of the total amount of helical flow in the fluid domain, irrespective of direction (Gallo et al., 2012).

The last two descriptors focused on the balance of rotating fluid structures: h_3 formulation is the following

$$h_3 = \frac{h_1}{h_2}$$

So, it is a non-dimensional quantity with values ranging between -1 and 1. When $h_3 = -1$, it means that only left-handed helical structures are present in the domain, while for $h_3 = 1$ the volume has only right-handed structure(Gallo et al., 2012).

Fourth descriptor h_4, on the other hand, neglects the major direction of rotation because it is the absolute value of h_3:

$$h_4 = |h_3| = \frac{|h_1|}{h_2}$$

with values ranging from 0 to +1. It describes the balance between counter-rotating structure (Gallo et al., 2012).

Q-CRITERION

Before introducing Q, it is necessary to introduce the Jacobian matrix: it is an *n* x *n* matrix that contains a first-order description of how the flow behaves locally around a given location and can be written as

$$J = \nabla v = \begin{pmatrix} \frac{\partial v_1}{\partial x_1} & \frac{\partial v_2}{\partial x_1} & \frac{\partial v_3}{\partial x_1} \\ \frac{\partial v_1}{\partial x_2} & \frac{\partial v_2}{\partial x_2} & \frac{\partial v_3}{\partial x_2} \\ \frac{\partial v_1}{\partial x_3} & \frac{\partial v_2}{\partial x_3} & \frac{\partial v_3}{\partial x_3} \end{pmatrix}$$

where v_i are the three velocity components and x_i are the three spatial directions.

Many region-based vortex extraction methods are based on the decomposition of the Jacobian $\mathbf{J}$ into $\mathbf{J} = \mathbf{S} + \mathbf{\Omega}$, with

$$\mathbf{\Omega} = \frac{\mathbf{J} - \mathbf{J}^T}{2}, \ \mathbf{S} = \frac{\mathbf{J} + \mathbf{J}^T}{2}$$

where the symmetric matrix S is called the strain rate tensor and the anti-symmetric matrix Ω is called vorticity tensor (Günther & Theisel, 2018).

Q is the second Jacobian invariant and is defined according to the following formula

$$Q = \frac{1}{2}\{[tr(\mathbf{J})]^2 - tr(\mathbf{J}^2)\} = \frac{1}{2}(\|\mathbf{\Omega}\|^2 - \|\mathbf{S}\|^2) + \frac{1}{2}(\nabla \cdot \mathbf{v})^2$$

where $\mathbf{v}$ is the velocity vector (Günther & Theisel, 2018).

In a 3D-divergence flow the ***Q-criterion*** considers a connected region to be a vortex if the second invariant of the Jacobian is positive. Using the definition formula above but considering $\nabla \cdot \mathbf{v} = 0$, the condition becomes

$$\frac{1}{2}(\|\mathbf{\Omega}\|^2 - \|\mathbf{S}\|^2) > 0.$$

The criterion considers a vortex as a region in which the vorticity tensor norm is stronger than the strain rate tensor one (Günther & Theisel, 2018). Final scalar Q computation for each point of the model volume, simplified and explained with the Jacobian components, is

$$Q = \frac{\partial v_1}{\partial x_1}\frac{\partial v_2}{\partial x_2} + \frac{\partial v_1}{\partial x_1}\frac{\partial v_3}{\partial x_3} + \frac{\partial v_2}{\partial x_2}\frac{\partial v_3}{\partial x_3} - \frac{\partial v_1}{\partial x_2}\frac{\partial v_2}{\partial x_1} - \frac{\partial v_1}{\partial x_3}\frac{\partial v_3}{\partial x_1} - \frac{\partial v_2}{\partial x_3}\frac{\partial v_3}{\partial x_2}.$$

The criterion condition remains $\mathbf{Q} > \mathbf{0}$.

3.3.3 - *ENERGY DISSIPATION METRICS*

As said in the introduction, Fontan procedure is fundamental for patient with single ventricle heart disease, but the consequent non-physiological conformation causes haemodynamic problems: for example, in literature one of the theme on which many studies focused is the quality of this surgical procedure in terms of energetical or power losses (Mauro Grigioni, D'Avenio, Amodeo, & Di Donato, 2006; Khiabani et al., 2012). Unfortunately, the main factors that affect this inefficiency are different, i.e. geometry of connection (Bravo-valenzuela et al., 2018; M Grigioni et al., 2003; Migliavacca et al., 2003; Ryu et al., 2001), varying resistances in the PAs (M Grigioni et al., 2003), pulsatile flow (Khiabani et al., 2012) and other.

For these reasons, an analysis on power losses and energy dissipation has to be done even in this study, where different metrics are studied.

PRESSURE DROPS

An interesting quantity that help to understand the haemodynamic behaviour of the model during the cardiac cycle is the pressure difference between the inlets and the outlets: thanks to the multiscale approach described in Chapter 2, the pressure levels within the computational domain are realistic. This is a key factor in hemodynamic modeling, since the pressure level at the different outlets may influence the pressure gradients between the inlet and outlet faces of the model, and therefore affect the flow distribution between the branches and the WSS field (Morbiducci et al., 2010). So, pressure drops are very important to see also the goodness of the model and computational work (Pekkan et al., 2005). Moreover, the pressure drops have a correlation with the blood flows: in the outlets the equation $P = RQ$ is valid (Dubini et al., 1996).

Pressure is considered uniform in the different axial section of the vessels.

The computation of inlet and outlet pressure values started with the creation of a single file containing all the pressure values during the (second) simulated cycle: in this case the cell data relative to ModelFaceID were used to identify the points belonging to the different surfaces of the model

- the points with ModelFaceID = 2 belong to SVC
- the points with ModelFaceID = 3 belong to RPA1
- the points with ModelFaceID = 4 belong to RPA2

- the points with ModelFaceID = 5 belong to LPA
- the points with ModelFaceID = 6 belong to IVC.

At this point, the mean values of each surface's pressure data on the space are calculated for each time-step and then the differences between inlets and outlets mean values are computed: in this way it is possible to have an idea of pressure drops during time. The differences are computed separately for SVC and IVC.

After that, mean values and standard deviations of the different ΔP are calculated in time too.

POWER LOSSES

The surgical palliation of Fontan condition requires an optimization of the new connection haemodynamic: we have to focus on the correct determination of the mechanical power dissipated by the blood flow in the studied district that is particular important because of the low level of pressure in the venous return (Mauro Grigioni et al., 2006).

The most rigorous method to calculate power losses in a connection with multiple inlets and outlets is proposed by Grigioni et al. and it requires the local pressure and flow profiles at BC knowledge: the following formula was already presented in 1987 (Leefe & Gentle, 1987) and is

$$W_{loss} = -\int_{IN}(p+\rho g h)\mathbf{u}\cdot\mathbf{dA} - \int_{IN}\frac{1}{2}\rho u^2\,\mathbf{u}\cdot\mathbf{dA} - \int_{OUT}(p+\rho g h)\,\mathbf{u}\cdot\mathbf{dA} - \int_{OUT}\frac{1}{2}\rho u^2\,\mathbf{u}\cdot\mathbf{dA}$$

where p is the static pressure, ρ the fluid density, g the gravity acceleration, h the elevation of fluid particle above an arbitrary horizontal plane, $\mathbf{u}$ the velocity vector and $\mathbf{dA}$ the oriented surface element ($\mathbf{dA} = \mathrm{d}A\mathbf{n}$, where $\mathbf{n}$ is the outward unit vector normal to the section); in this equation, the first and the third term represent the static contribution, while the second and the fourth are the dynamical contributions (Mauro Grigioni et al., 2006).

However, in our case, the gravitational contribution is neglected and the formula becomes

$$W_{loss} = -\int_{IN} p\,\mathbf{u}\cdot\mathbf{dA} - \int_{IN}\frac{1}{2}\rho u^2\,\mathbf{u}\cdot\mathbf{dA} - \int_{OUT} p\,\mathbf{u}\cdot\mathbf{dA} - \int_{OUT}\frac{1}{2}\rho u^2\,\mathbf{u}\cdot\mathbf{dA}$$

VISCOUS DISSIPATION RATE

Fluid flow efficiency in Fontan connection is fundamental because pulmonary circulation is without the ventricular support and this arises the importance of venous return efficiency. To quantify the quality of Fontan connection from an energy point of view, in addition to power losses analysis, another metric is used, the Viscous Dissipation Rate (VDR). Its difference from power losses is that it doesn't require limiting assumption and it is easy to calculate in the clinic. Moreover, VDR can provide an additional insight because it has spatial distribution contours and time-resolved values.

In Yoganathan et al. opinion, using VDR has some benefits in studying Fontan efficiency and it fulfils some basic but important requirements for a haemodynamic metric: it accurately describe Fontan physiological flow efficiency; it can be easily calculable from clinical measurements; and it maintain the relationship between Fontan connection flow efficiency and patient outcomes from previous studies (Wei et al., 2018).

The relative formulation in Pa/s is (Wei et al., 2018)

$$VDR = \mu\left[2\left(\frac{\partial u_x}{\partial x}\right)^2 + 2\left(\frac{\partial u_y}{\partial y}\right)^2 + 2\left(\frac{\partial u_z}{\partial z}\right)^2 + \left(\frac{\partial u_x}{\partial y} + \frac{\partial u_y}{\partial x}\right)^2 + \left(\frac{\partial u_x}{\partial z} + \frac{\partial u_z}{\partial x}\right)^2 + \left(\frac{\partial u_y}{\partial z} + \frac{\partial u_z}{\partial y}\right)^2\right]$$

where μ is fluid density and u_x, u_y, u_z are the three components of velocity vector.

VDR can now be studied mediated in time or in volume and, in both cases, it gives interesting information. Time integration is executed on a single cycle and tells us time-averaged data for each volume point of the model: its mathematical formulation in Pa/s is

$$\Phi_V = \frac{1}{T}\left\{\mu \int_T^0 \left[2\left(\frac{\partial u_x}{\partial x}\right)^2 + 2\left(\frac{\partial u_y}{\partial y}\right)^2 + 2\left(\frac{\partial u_z}{\partial z}\right)^2 + \left(\frac{\partial u_x}{\partial y} + \frac{\partial u_y}{\partial x}\right)^2 + \left(\frac{\partial u_x}{\partial z} + \frac{\partial u_z}{\partial x}\right)^2 + \left(\frac{\partial u_y}{\partial z} + \frac{\partial u_z}{\partial y}\right)^2\right] dt\right\}$$

where T is the period of one cardiac cycle.

Chapter 4 – Results

After unsteady-state simulations, wall and volume data were exported from *SimVascular* for each time step of the second cardiac cycle (the first one was discarded to avoid the impact of initial conditions on our results). In particular, WSS and pressure data at luminal surface and pressure and velocity data in bulk were extracted. The series of indicators presented in Chapter 3 were computed and studied in order to understand the haemodynamic behaviour for each velocity input profile, the possible presence of atherogenic areas or the energy losses and distribution into this Fontan image-based model.

Each following comparison is made on the original model without FE: all the results for each time-step were inserted in a single file with only the wall (for surface descriptors) or the wall and its volume with the caps (for volume information). These steps were possible thanks to a series of Python and VMTK scripts.

In the following, the resulting figures are reported and discussed.

4.1 - WSS-BASED DESCRIPTORS

4.1.1 - *TAWSS*

Figure 58 shows the Paraview visualization of this parameter for each velocity profile case in front and back view: it is important to underline that the risk values for TAWSS are the values below 4 dynes/cm^2 that for this reason are coloured in red (Morbiducci et al., 2011).

In Figure 58 it is possible to see that the areas with lower TAWSS values are at the beginning of SVC and at the end of LPA, while in the centre of the model, where the branches meet, there are no relevant risk value; in this area, at the beginning of LPA, a small zone with the highest TAWSS values is always present.

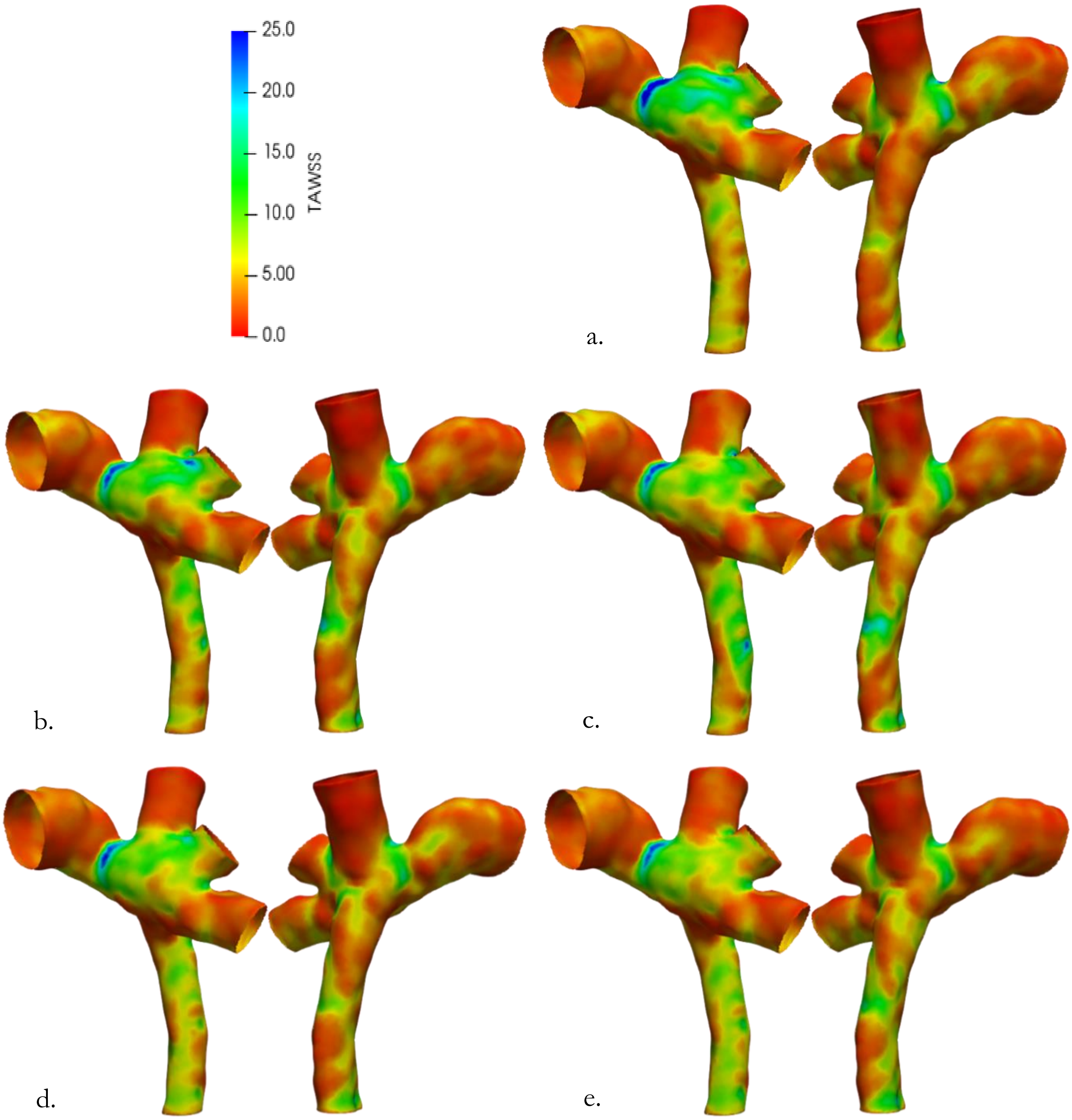

Figure 58 - TAWSS distribution in dynes/cm²: a. baseline; b. IP33 double vortex; c. IP66 double vortex; d. IP33 single vortex; e. IP66 single vortex

After this visual comparison, an interesting analysis can be done through another Python script where the percentile computation is executed. Because the dangerous area are the ones with low TAWSS values, the 20th and the 10th percentile are calculated on a population that contains all the time-averaged shear stress values of all the velocity profiles (Morbiducci et al., 2013): the areas in which TAWSS is lower than the 20th percentile (2.136 dynes/cm²) or even lower than the 10th percentile (1.654 dynes/cm²) are very dangerous from a atherogenic point of view. The distribution of the risk areas identified by the TAWSS values are reported in Figure 59.

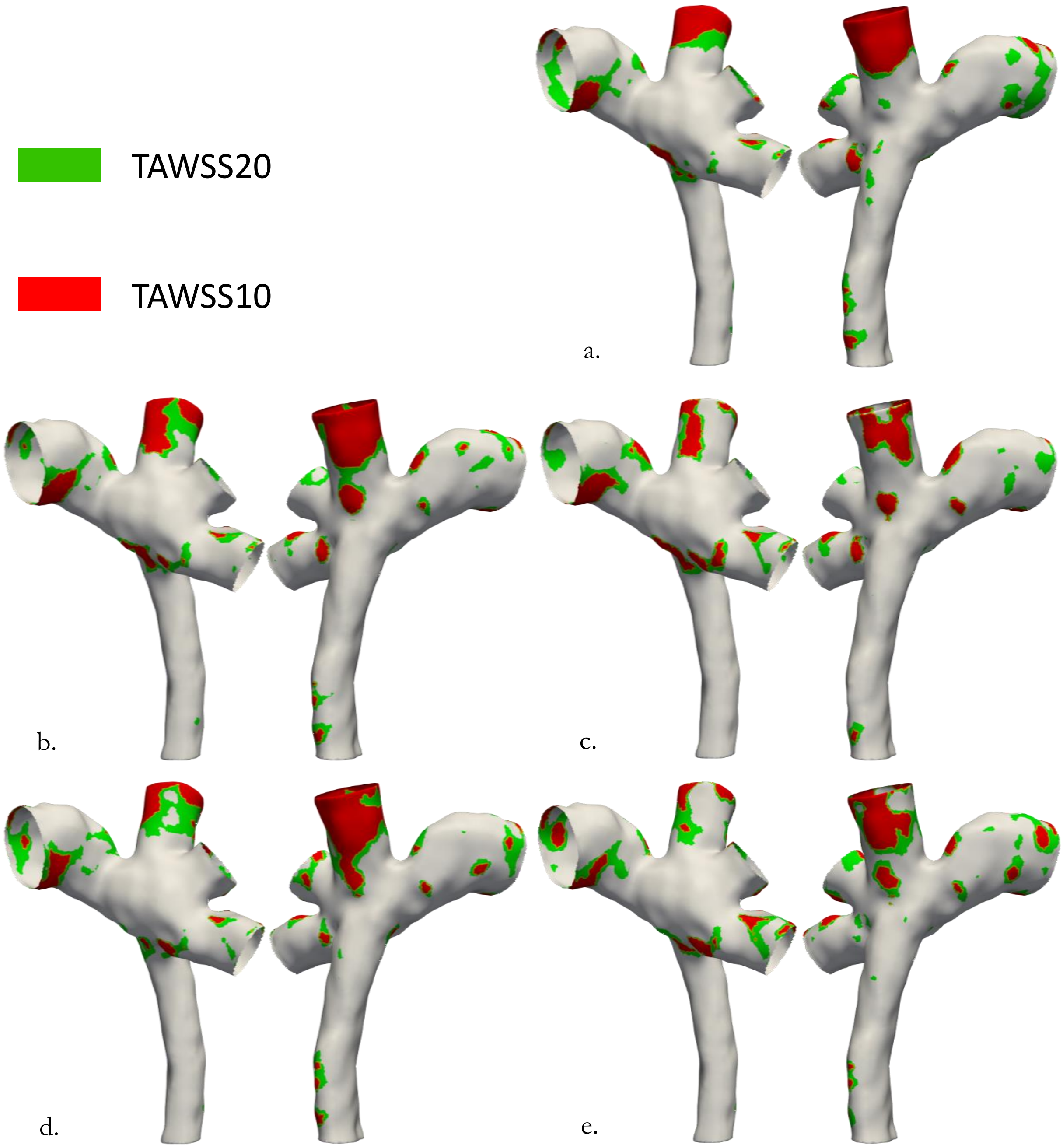

Figure 59 - TAWSS risk areas: a. baseline; b. IP33 double vortex; c. IP66 double vortex; d. IP33 single vortex; e. IP66 single vortex

Figure 59 results confirm the considerations done before for TAWSS distribution with the most dangerous area at SVC and LPA.

To simplify the comprehension of this visual comparison, Figure 60 shows a histogram in which the risk area is calculated respect to the total area of the model, in order to have a percentage value of areas with TAWSS value lower than the 20th or 10th percentile.

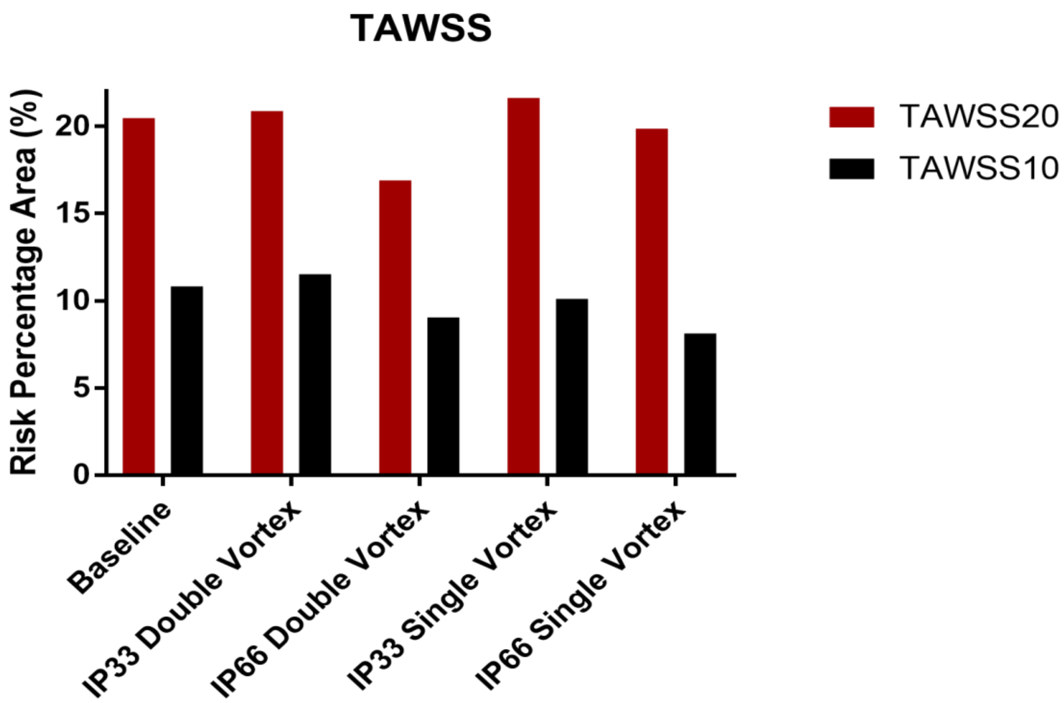

Figure 60 - TAWSS risk percentage area

In Figure 60 there is a comparison of all the velocity profiles and it is interesting to note that both the waveform with a higher IP velocity magnitude (IP66) are the ones with lower percentage of risk areas in TAWSS 20th percentile (IP66 Double Vortex) and in TAWSS 10th percentile (IP66 Single Vortex) cases, with respectively 16.891% and 8.127% of dangerous areas.

4.1.2 - *OSI*

The OSI computation was done for all the velocity profiles cases and Figure 61 shows the Paraview visualization of this parameter: in this case the dangerous values (coloured in red) are the highest, so the ones that are near to 0.5 (Morbiducci et al., 2010, 2011).

OSI distribution differs a lot from TAWSS one: in this case, the highest values are present at the end of IVC, where this vein attached the core of the whole connection, and in some points of LPA.

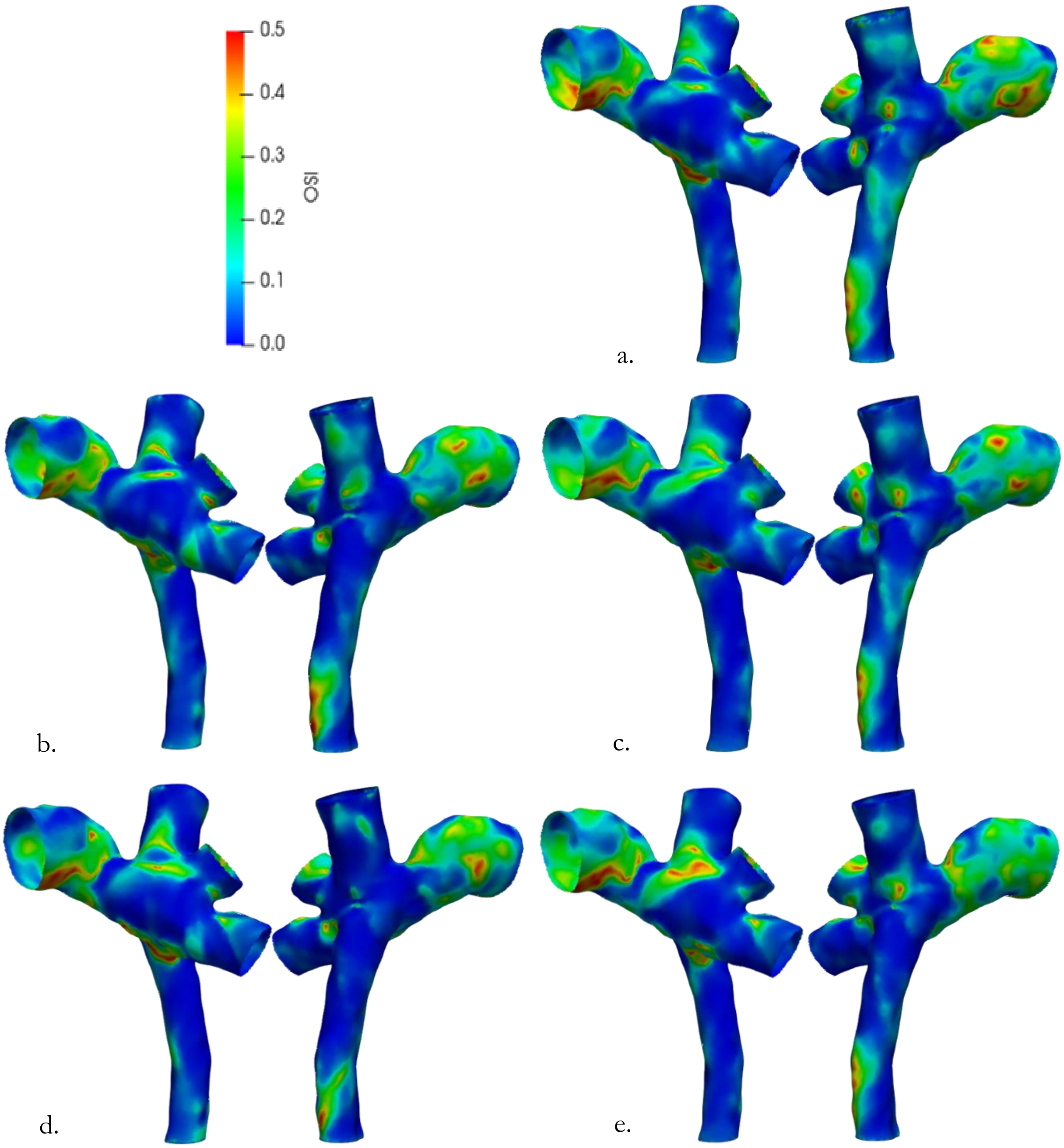

Figure 61 - OSI distribution: a. baseline; b. IP33 double vortex; c. IP66 double vortex; d. IP33 single vortex; e. IP66 single vortex

As for TAWSS, the next analysis concerns the percentile computation: because the dangerous area are the ones with high OSI values, the 80th and the 90th percentile are calculated on a population that contains all the points of all the velocity profiles (Morbiducci et al., 2011, 2013). The most dangerous regions from an atherogenic point of view are where OSI values are higher than the 80th percentile (0.159) or even higher than the 90th percentile (0.246). The distribution of the risk areas identified by the OSI values are reported in Figure 62.

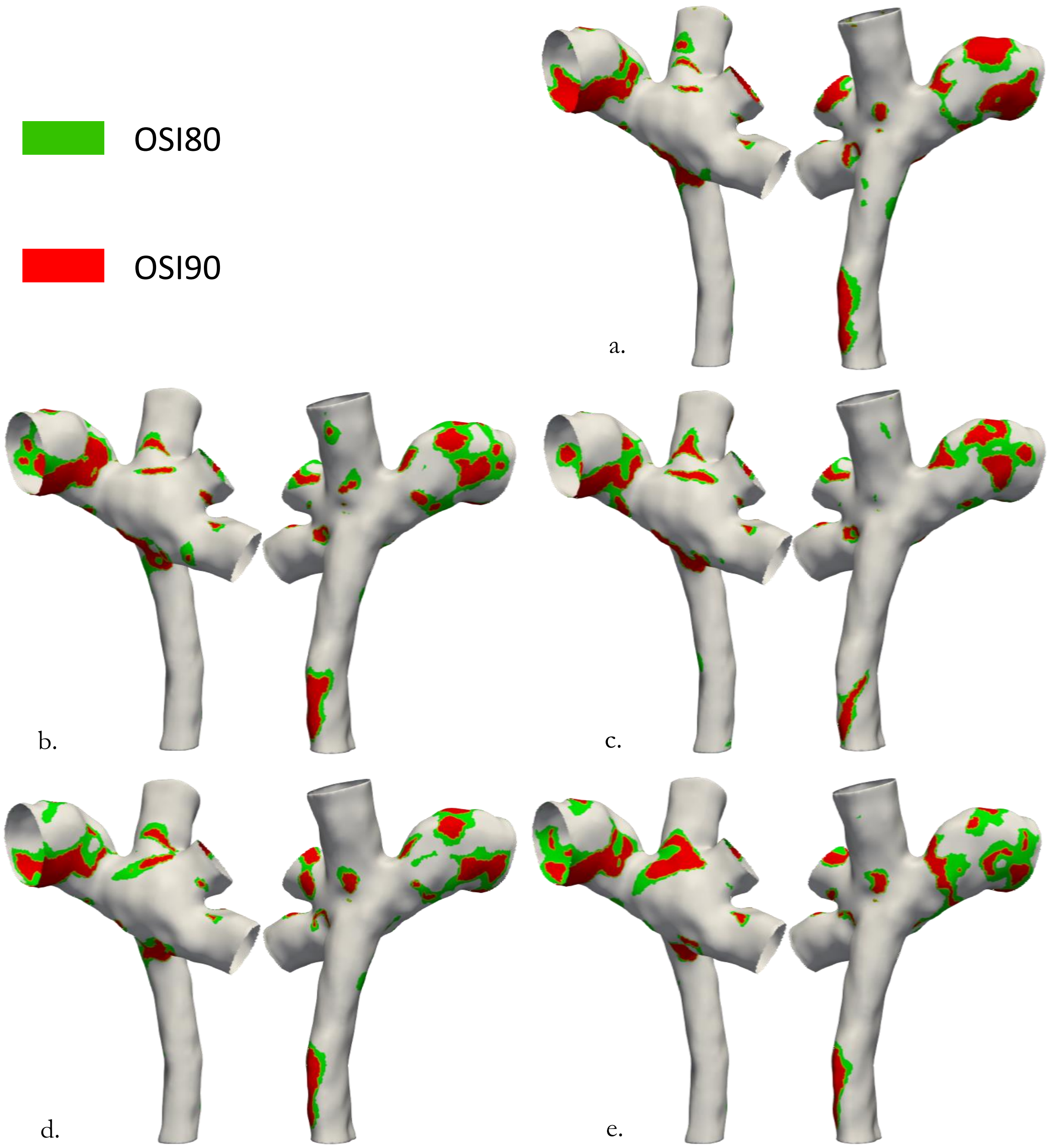

Figure 62 - OSI risk areas: a. baseline; b. IP33 double vortex; c. IP66 double vortex; d. IP33 single vortex; e. IP66 single vortex

Figure 62 helps to identify the risk zone in OSI distribution: IVC has dangerous areas at the beginning (visible in the back view) and at the end; different risk areas are present also in LPA and where SVC connects with the other vessels (especially in IP66 single vortex case).

To simplify the comprehension of this visual comparison, Figure 63 shows a histogram in which the risk region is calculated respect to the total area of the model, in order to have a percentage value of areas with OSI value higher than the 80th or 90th percentile.

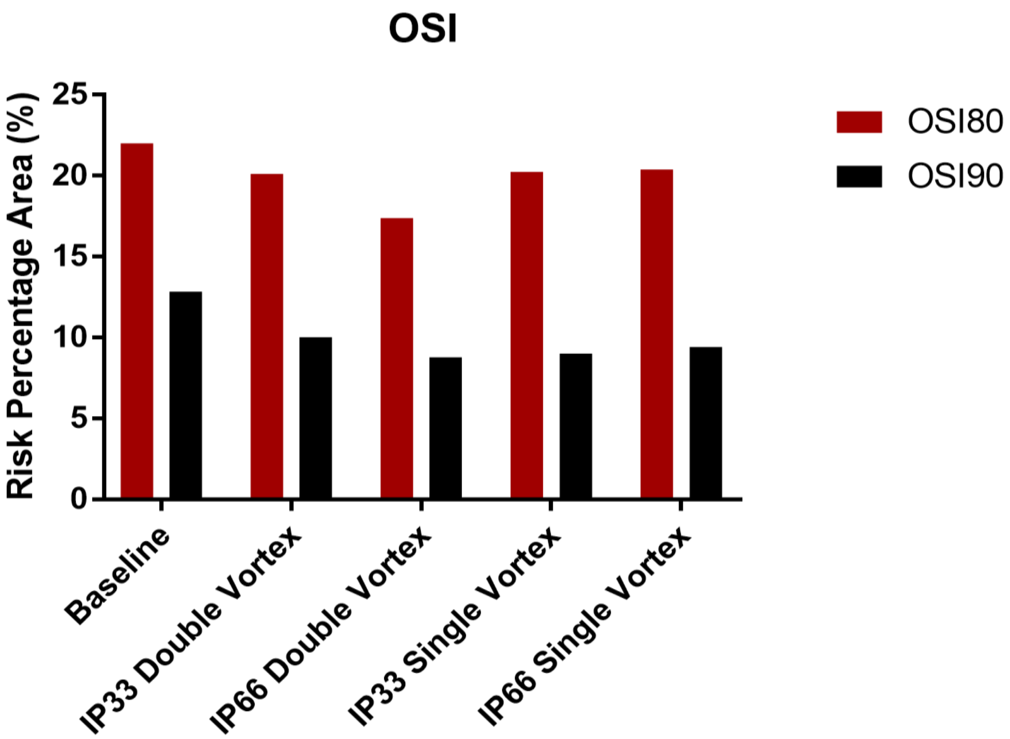

Figure 63 - OSI risk percentage area

In Figure 63 comparison between all the velocity profiles, it is notable that IP66 Double Vortex has the lower percentage of risk areas in both 80th and 90th OSI percentiles, with percentage values of 17.387% and 8.781% respectively. In single vortex cases there is no appreciable difference between IP33 and IP66.

4.1.3 - *RRT*

RRT distribution is computed for all the velocity profiles cases and it is possible to see it through Paraview visualization in Figure 64. In this case the dangerous values (coloured in red) are the highest (Morbiducci et al., 2010, 2011), because, if TAWSS decreases, RRT increases and, if OSI increases, RRT increases too. Risk areas are at the end of IVC and in LPA: dangerous surfaces corresponds to the OSI ones.

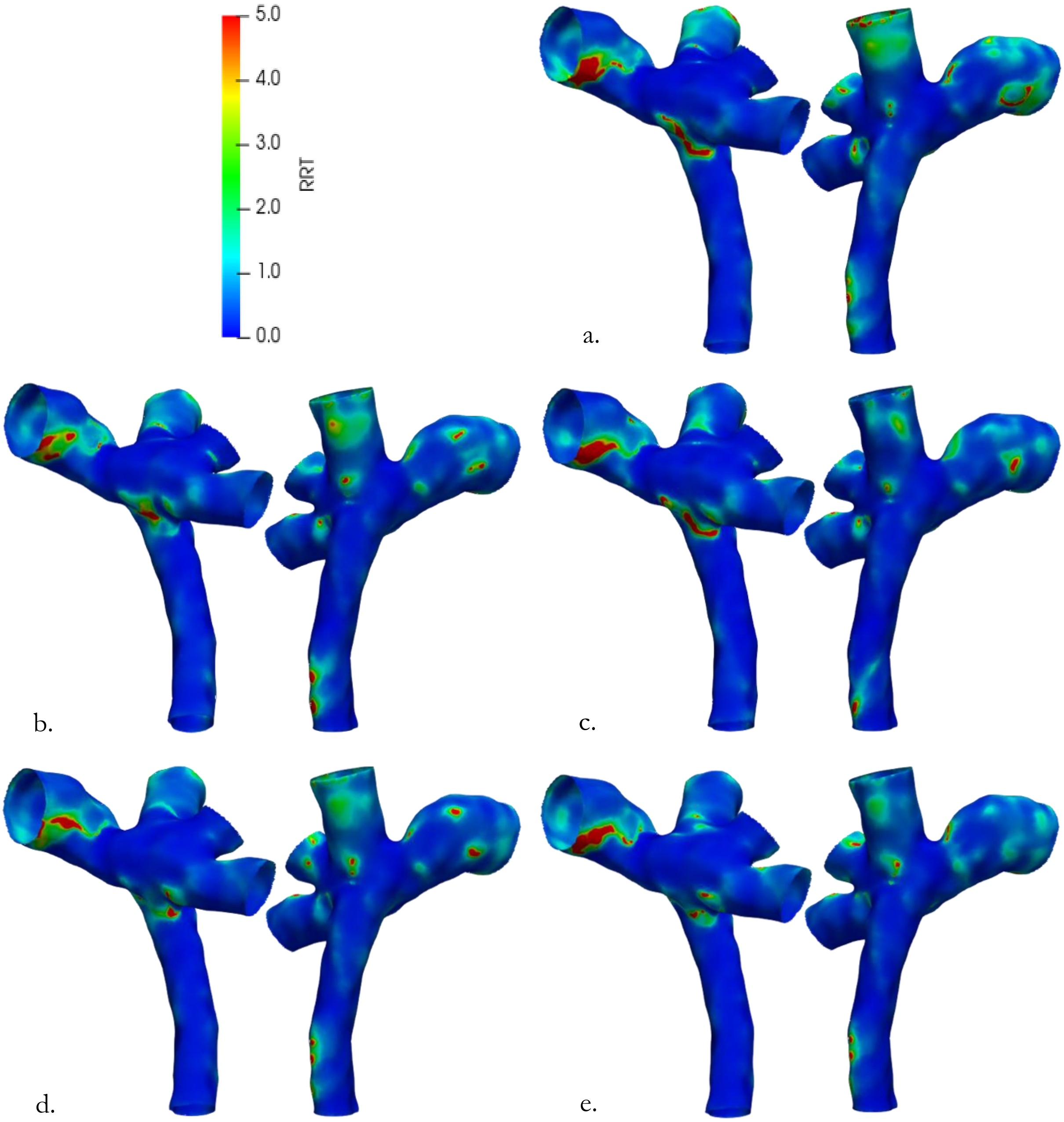

Figure 64 - RRT distribution in $cm^2/dynes$: a. baseline; b. IP33 double vortex; c. IP66 double vortex; d. IP33 single vortex; e. IP66 single vortex

As for the previous descriptors, the next analysis concerns the percentile computation through a Python script: because the dangerous area are the ones with high RRT values, the 80th and the 90th percentile are calculated on a population that contains all the points of all the velocity profiles (Gallo et al., 2012; Morbiducci et al., 2011, 2013). The most dangerous regions from an atherogenic point of view are where RRT values are higher than the 80th percentile (0.686 cm^2/dynes) or even higher than the 90th percentile (1.063 cm^2/dynes). The distribution of the risk areas identified by the RRT values are reported in Figure 65.

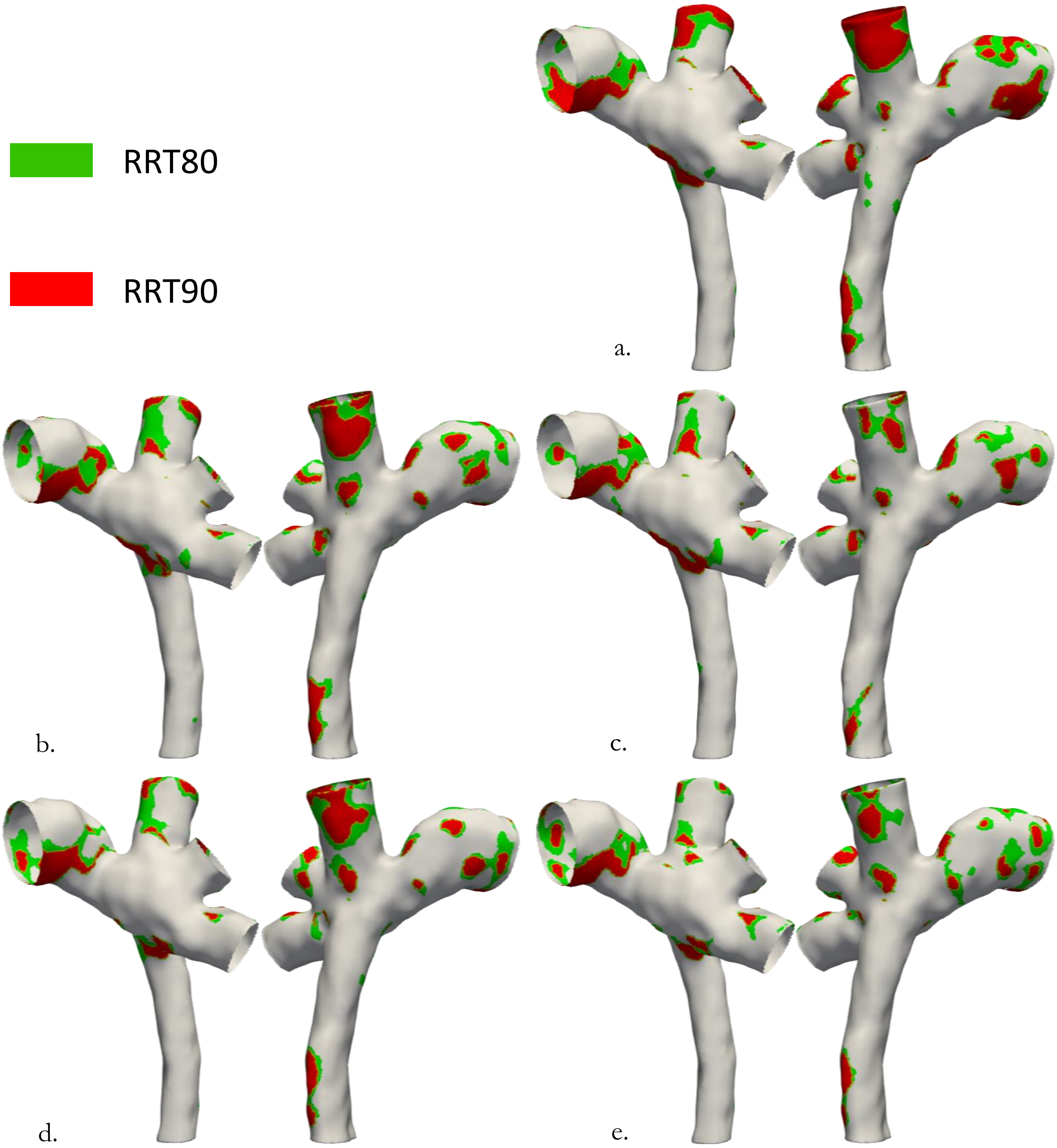

Figure 65 - RRT risk areas: a. legend; b. baseline; c. IP33 double vortex; d. IP66 double vortex; e. IP33 single vortex; f. IP66 single vortex

Figure 65 shows the most dangerous areas in RRT case: they are a sort of sum of TAWSS and OSI risks zones because it includes SVC, LPA and IVC areas.

The histogram shown in Figure 66 simplifies the comparison between the different velocity profiles: the risk region is calculated respect to the total area of the model, in order to have a percentage value of areas with RRT value higher than the 80th or 90th percentile.

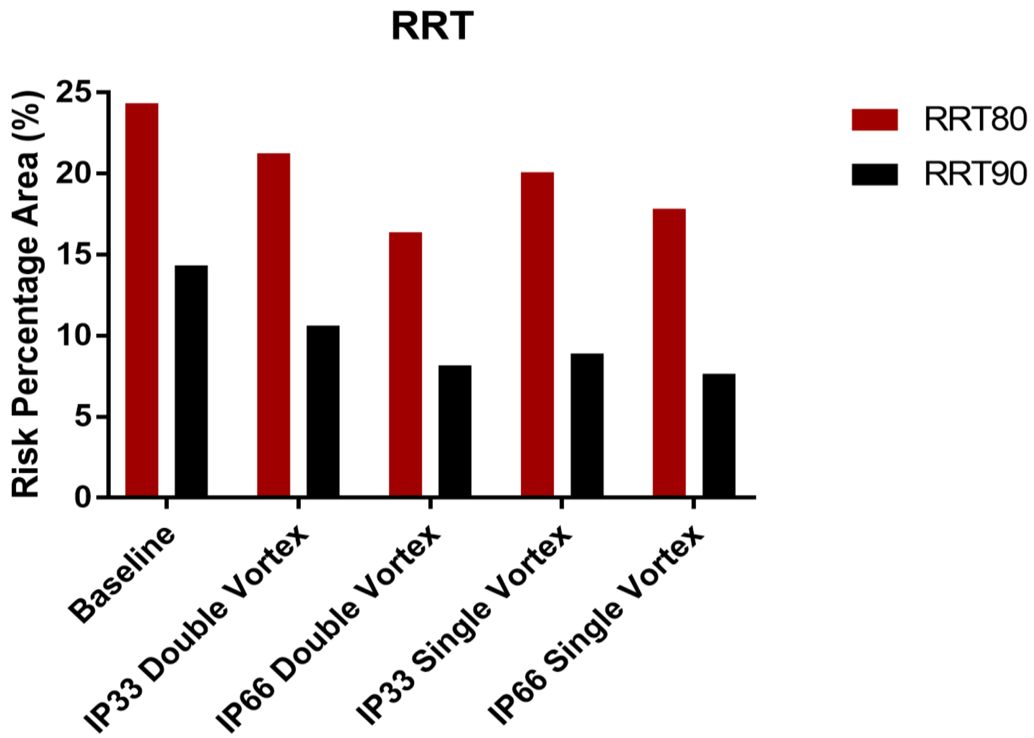

Figure 66 - RRT risk percentage area

The comparison between the different waveforms reported in Figure 66 shows that both the waveform with a higher IP velocity magnitude (IP66) are the ones with lower percentage of risk areas (16.389%) in RRT 80th percentile (IP66 Double Vortex) and (7.658%) in RRT 90th percentile (IP66 Single Vortex) cases.

4.2 - BULK FLOW METRICS

4.2.1 - *HELICITY AND LNH*

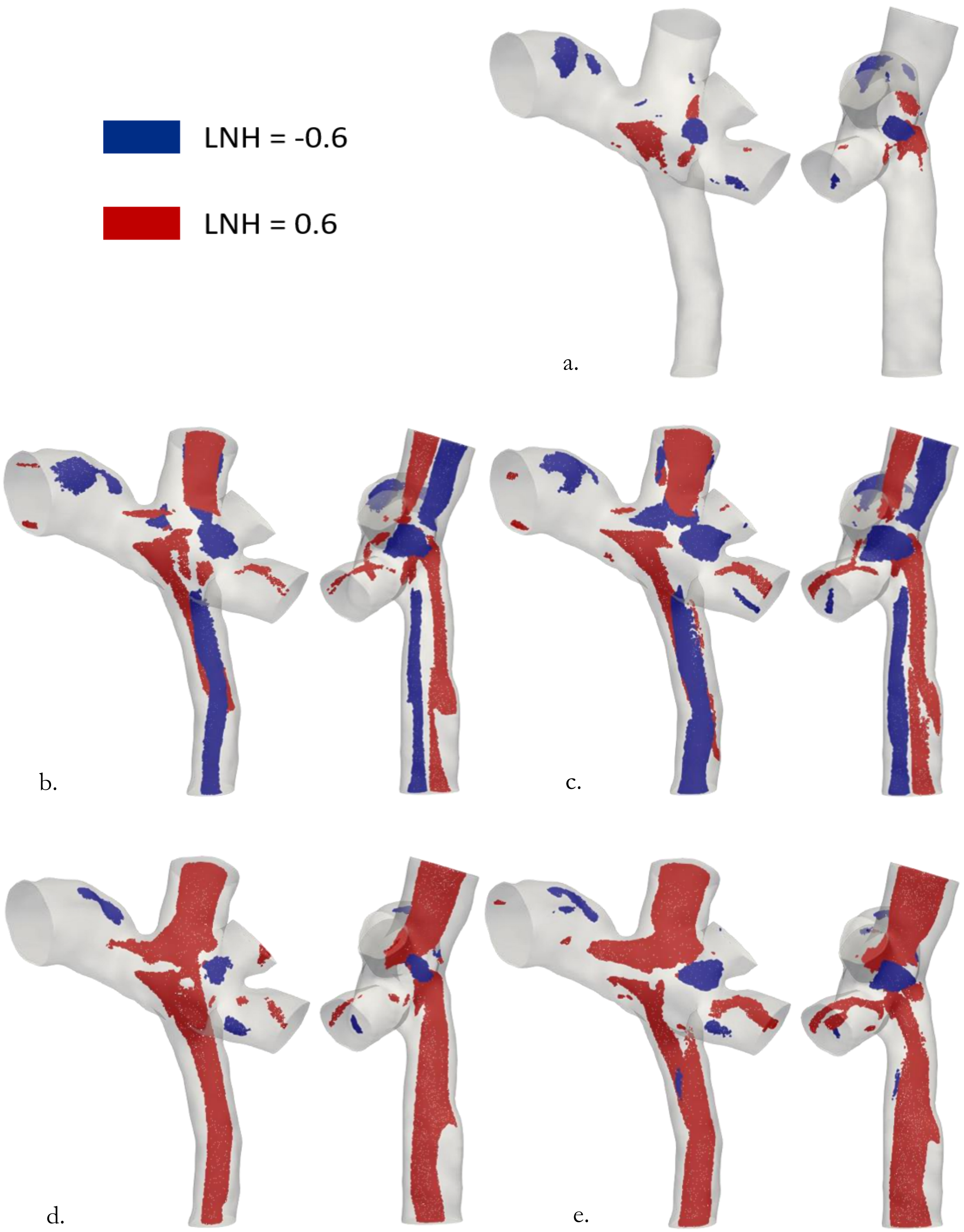

Figure 67 - Mean LNH distributions: a. baseline; b. IP33 double vortex; c. IP66 double vortex; d. IP33 single vortex; e. IP66 single vortex

LNH describes the alignment of velocity and vorticity directions during the cycle. Figure 67 shows the mean values of LNH over the 2nd cycle simulated for each velocity profiles in Paraview front and lateral view, because these views allow to better visualize the vortex induced through the Double Vortex velocity profiles: the optimal LNH threshold for visualization purposes were 0.6 (red, right-handed) and -0.6 (blue, left-handed).

Comparing the different cases, the baseline has very few values over and under the imposed thresholds: probably when there is only the TP component, the angle between velocity and vorticity is about 90 degrees, so the two vectors are often perpendicular. Another observation is about the two Double Vortex velocities: in Figure 67 it is visible the permanence of the division of the two vortices for the whole length of SVC and IVC vessels, while in the centre of the model this separation ends. On the other hand, in single vortex cases it is visible only one verse of rotation in both SVC and IVC.

4.2.2 - *H DESCRIPTORS*

h_1 represents the average helicity, the values for each boundary condition are reported in the histogram in Figure 68, comparing this descriptor for each velocity profile. From Figure 68 we understand that Double Vortex cases have low values because h_1 considers even the direction of rotation of the helical flow patterns the two vortices balance themselves.

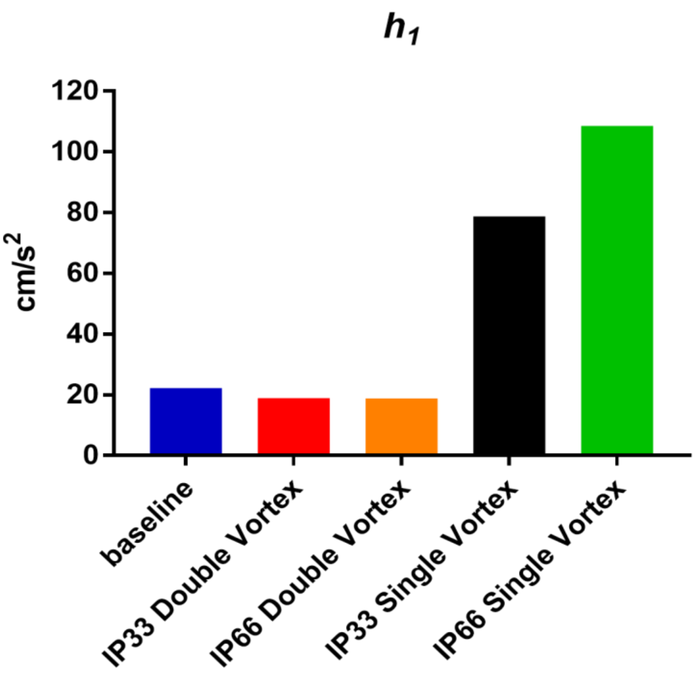

Figure 68 - h1 descriptor

Like h_1, h_2 is a value in cm/s^2 and is represented towards a histogram represented in Figure 69.

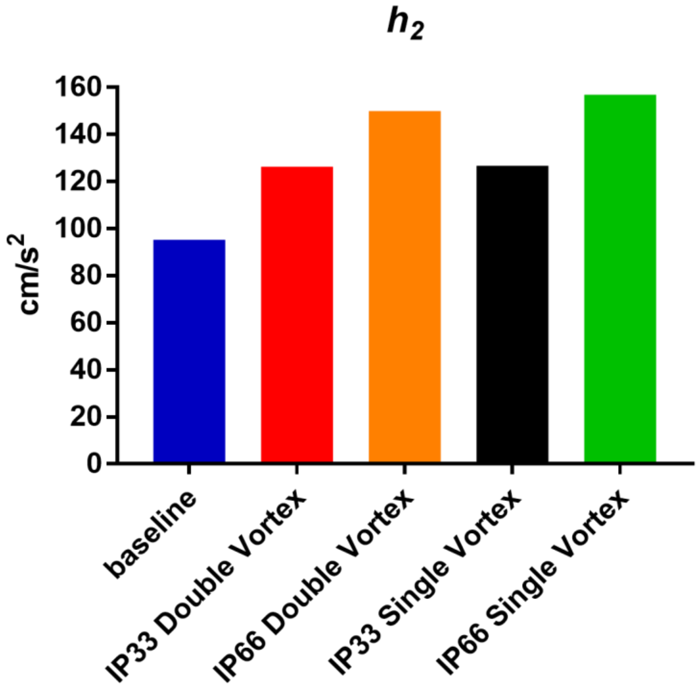

Figure 69 - h2 descriptor

Because of h_2 formulation (in particular, the presence of the absolute value), this parameter does not consider the different direction of rotation of helical flow patterns: for this reason, this descriptor strongly depends on the module value of in-plane velocity, but not on the pattern imposed by IP velocity. In fact, the IP33 velocities h_2 values are almost the same and the same it's true also for the IP66 cases. So, we can conclude that h_2 strongly depends on the boundary condition.

We prefer h_2 high values because it indicates a good presence of helical flow: the best profiles are the two with IP66 velocity.

However, it is noticeable the difference between h_1 and h_2 double vortex values. This difference can be explained because the counter rotating structures are considered in the first parameter, with a balancing effect on h_1 value, while the second descriptor neglect them.

The last two descriptors focused on the balance of rotating fluid structures: in our case h_3 and h_4 are exactly the same, so only h_3 histogram is reported in Figure 70.

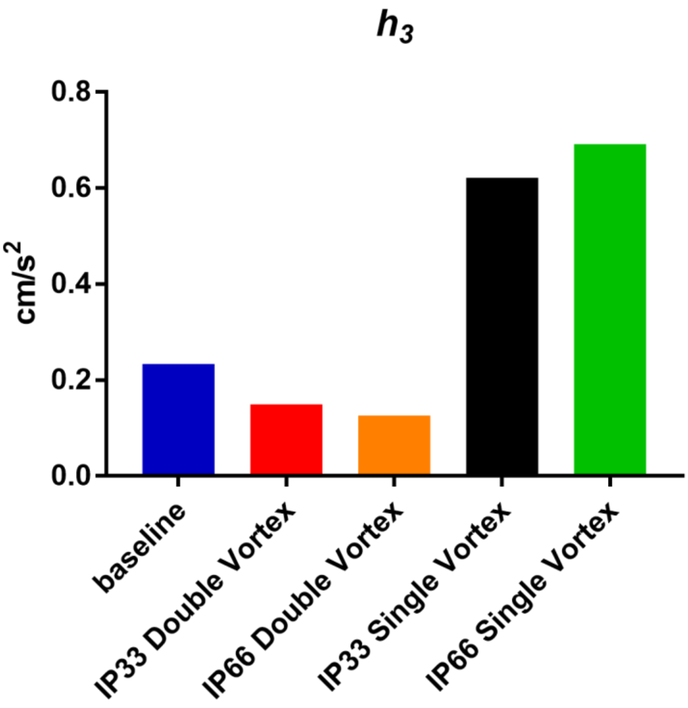

Figure 70 - h3 (and h4) descriptor

Even in this case, the different rotation directions are considered, so the profiles with two vortices have low h_3 values. Figure 70 confirms the considerations made above for h_1.

4.2.3 - *Q-CRITERION*

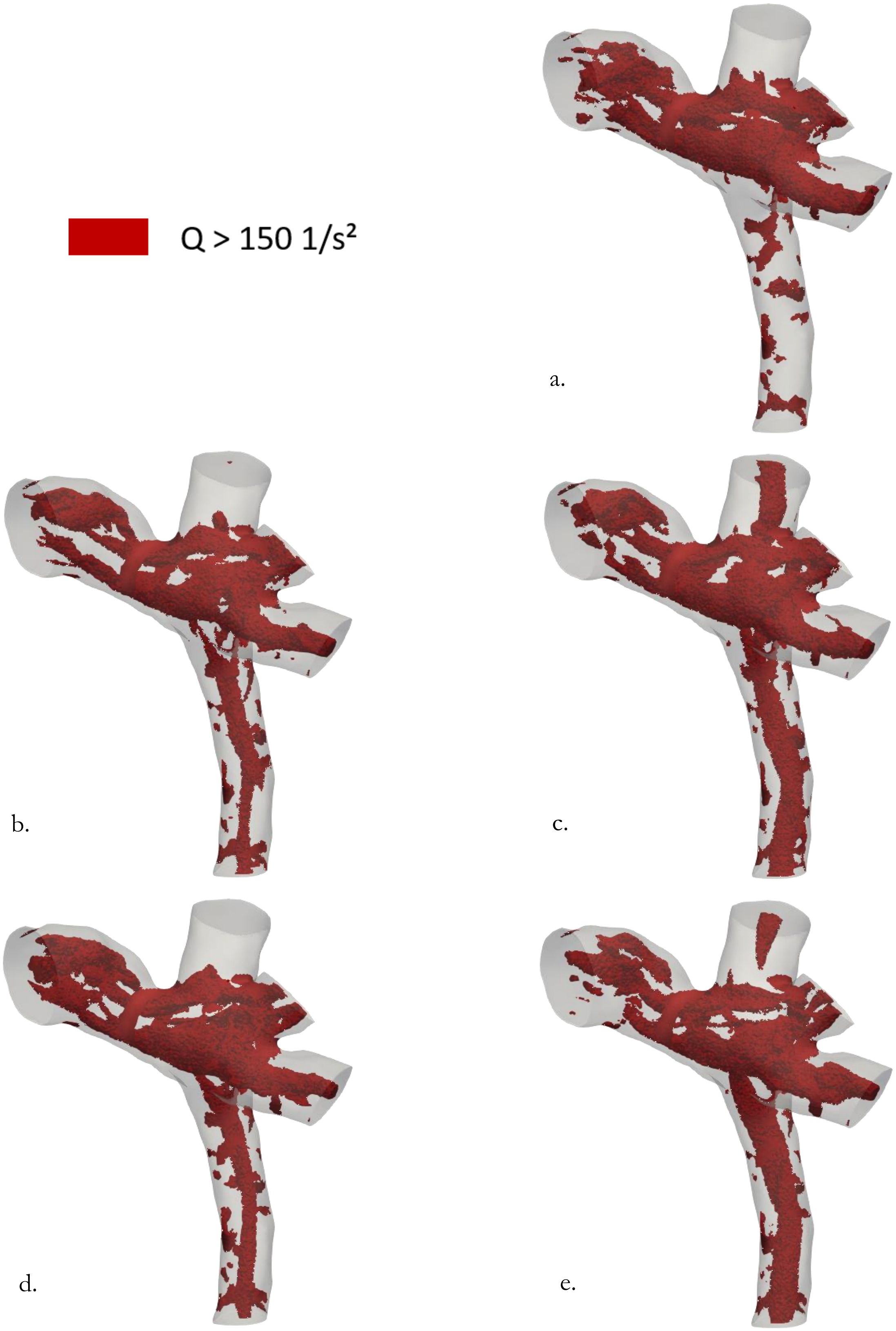

Figure 71 - Volumes with Q mean values > 150 1/s²: a. baseline; b. IP33 double vortex; c. IP66 double vortex; d. IP33 single vortex; e. IP66 single vortex

Figure 71 shows the distributions of time-averaged volumes that satisfy *Q-criterion*: however, a 150 $1/s^2$ threshold is imposed for a better visualization of the interested flow structures. In literature some cases of representation of *Q-criterion* with a higher threshold are present (Anufriev, Krasinsky, Shadrin, & Sharypov, 2014; Günther, Schulze, & Theisel, 2016). In this figure the baseline case has structures that have $Q > 0$ only where the vessels converge, while in the other velocity profiles there are visible flow volumes even for all the inlets length (especially in IVC).

Now, the percentage of volume (respect to the total amount of volume) that satisfies *Q-criterion* is represented: Figure 72 shows the change in time of this percentage, while Figure 73 displays the mean and standard deviation values. No significant different are present in these graphs.

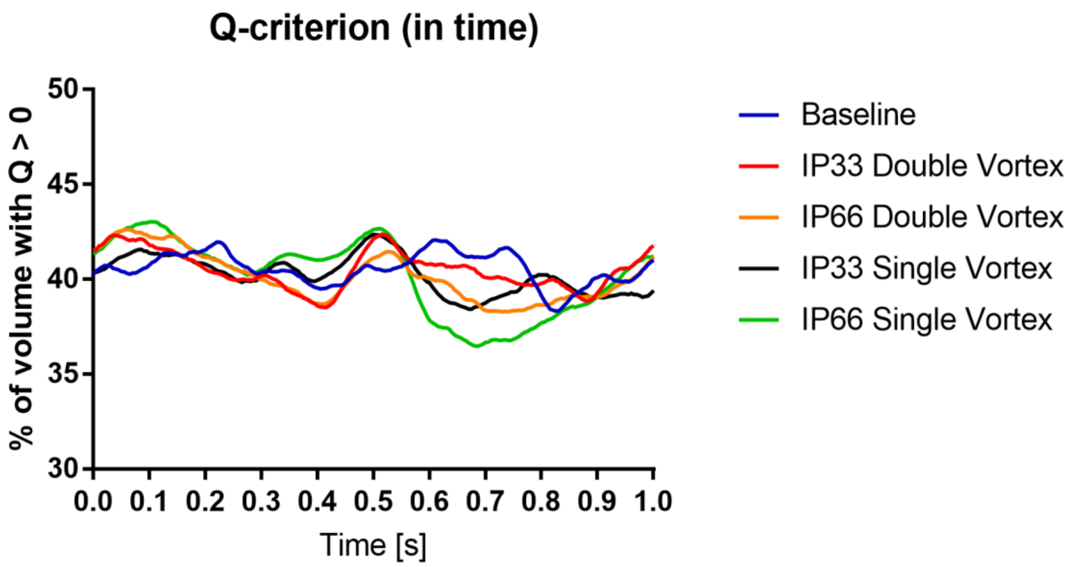

Figure 72 - Percentage of volume with Q > 0 in time

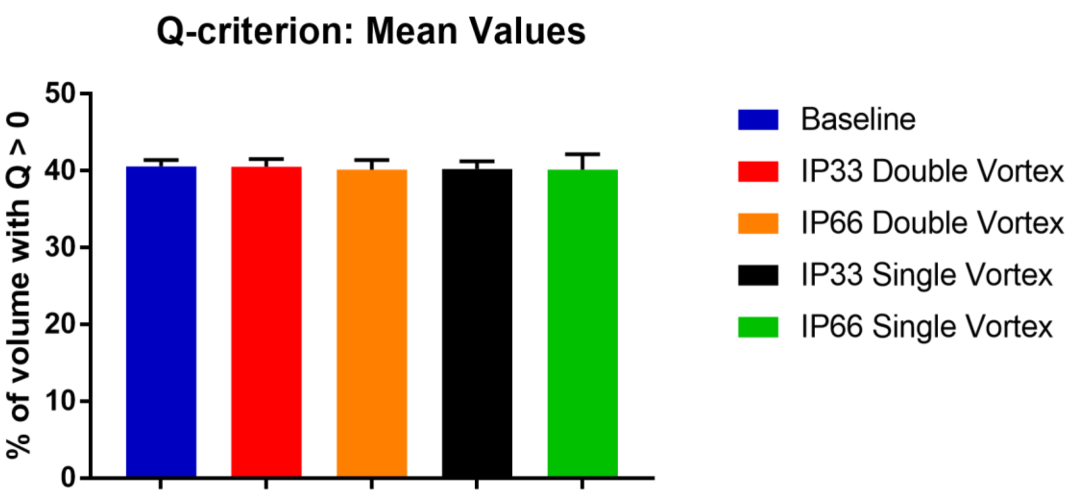

Figure 73 - Mean values of percentage of volume with Q > 0

4.3 - ENERGY DISSIPATION METRICS

4.3.1 - *PRESSURE DROPS*

The pressure drops during time are represented in time in Figure 74 and Figure 75 where all the different velocity profiles cases are compared separately for SVC and IVC respectively.

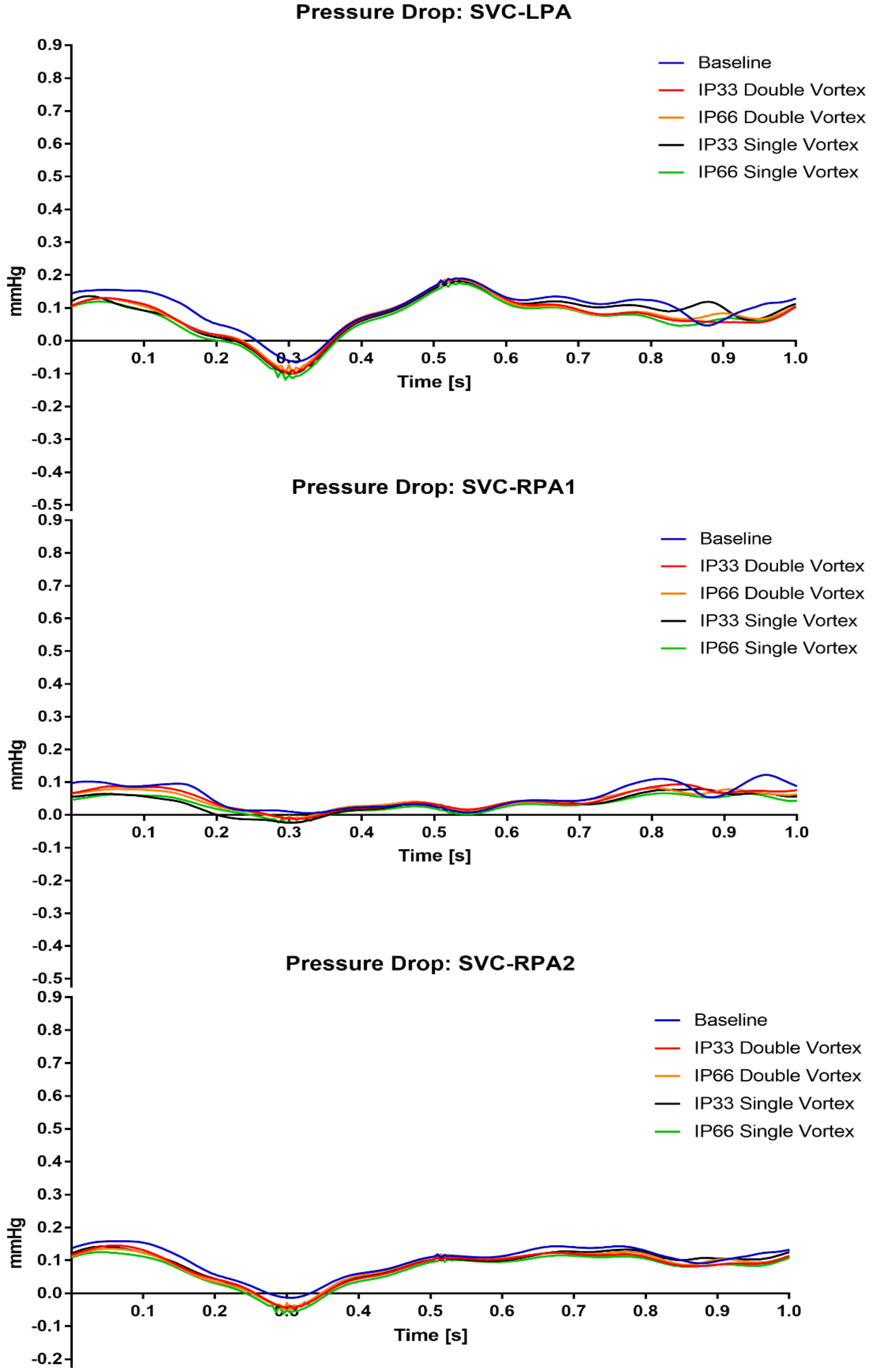

Figure 74 - SVC pressure drops

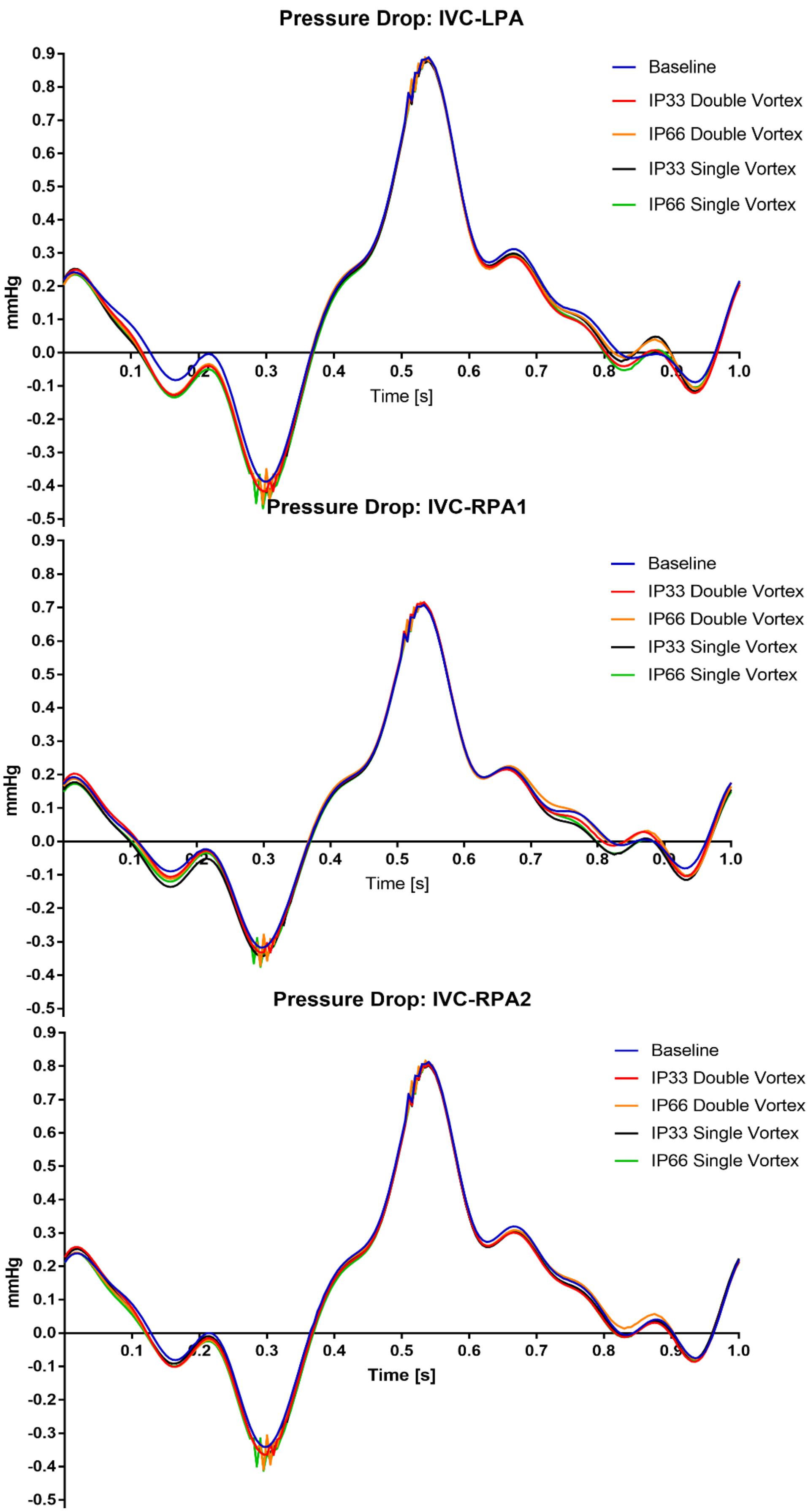

Figure 75 - IVC pressure drops

After that, mean values and standard deviations of the different pressure drops were calculated averaged on the cardiac cycle.

In Figure 76 they are reported in bar diagrams with error bars, comparing the cases with different input profile for each pressure drop.

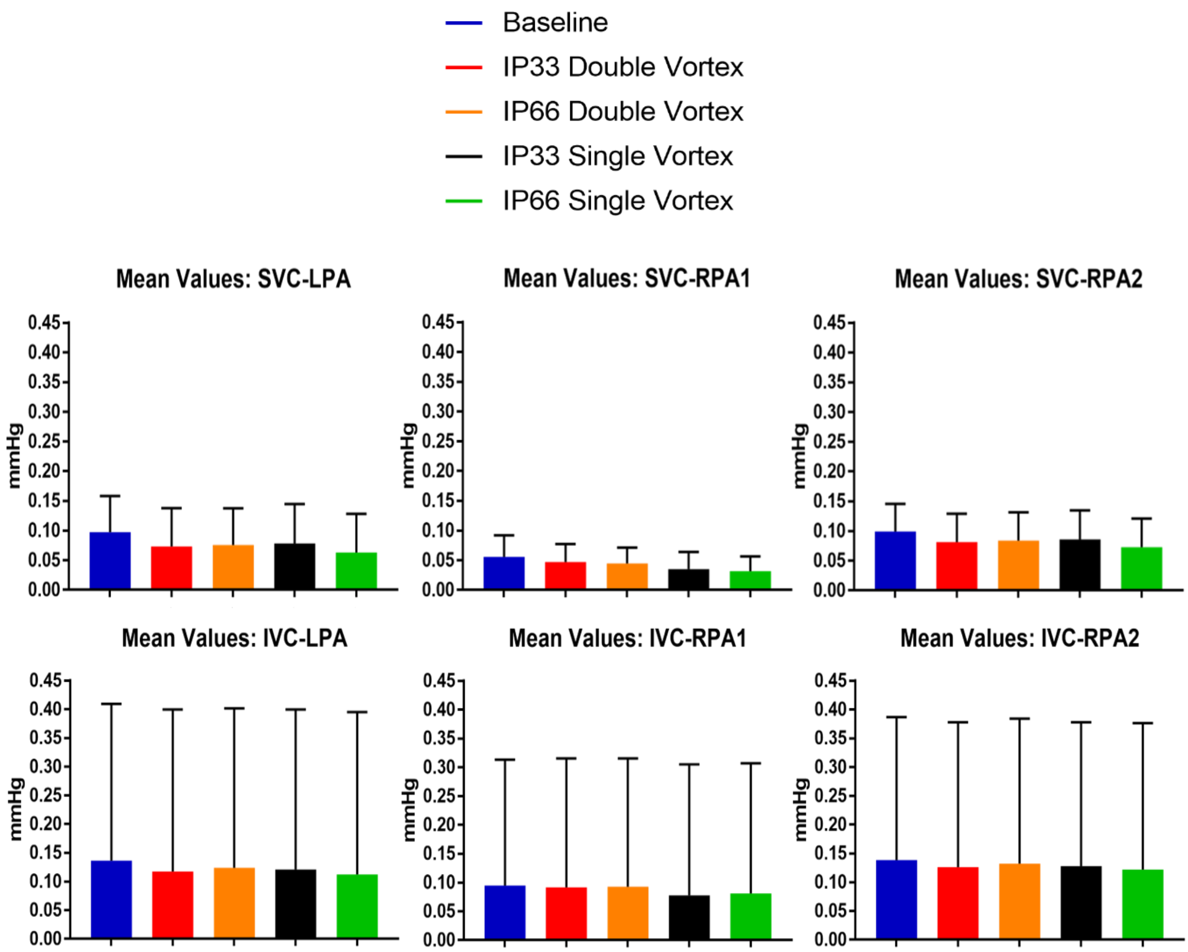

Figure 76 - Pressure drops: mean values and standard deviations

As it is possible to see in Figure 74, Figure 75 and Figure 76 pressure drops calculated respect to IVC have a major variability during the cardiac cycle, visible also in the standard deviation bars: probably it happens because even the flow and its variability were higher in IVC than SVC. Moreover, the trend over time of the different output is similar and comparable in both SVC and IVC cases.

4.3.2 - *POWER LOSSES*

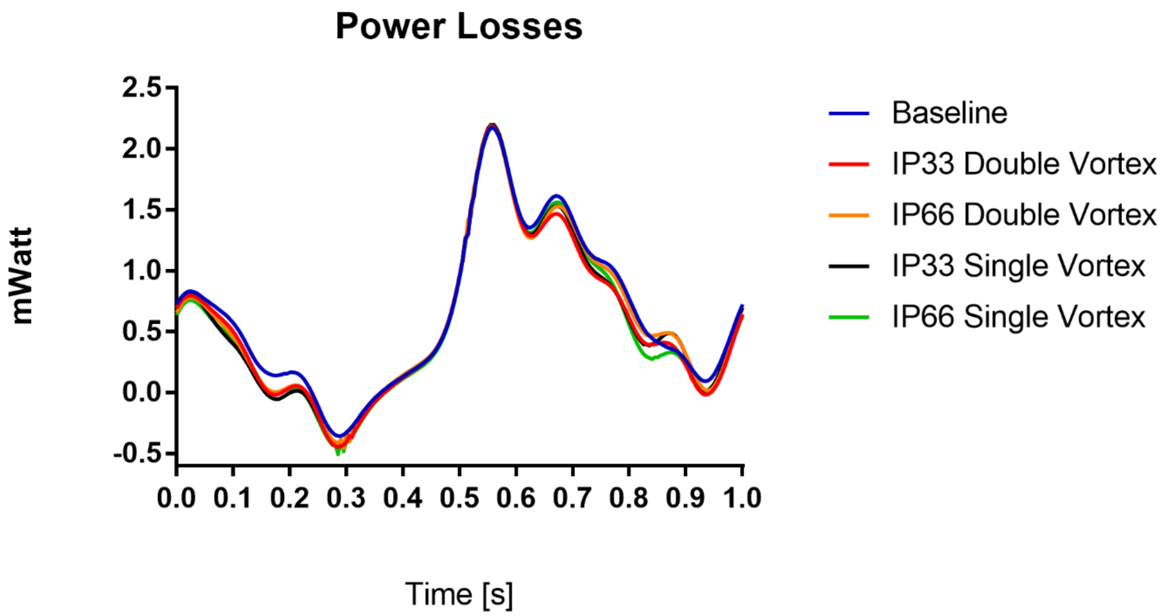

Figure 77 - Power losses in time

The comparison of time behaviour power losses between each velocity profile is studied and reported in Figure 77.

The power losses trend of the different velocity profile is the same, there are no marked differences. An interesting consideration is that the power losses behaviour in time brings us back to the IVC's pressure drops one reported in Figure 75: in fact, the maximum and minimum peaks are exactly at the same time instants.

At this point, the comparison involves the power losses mean values and standard deviations of the different velocities, but the differences between the cases are very low: for these reasons Figure 78 represents the power losses percentage differences of the profiles respect to the baseline.

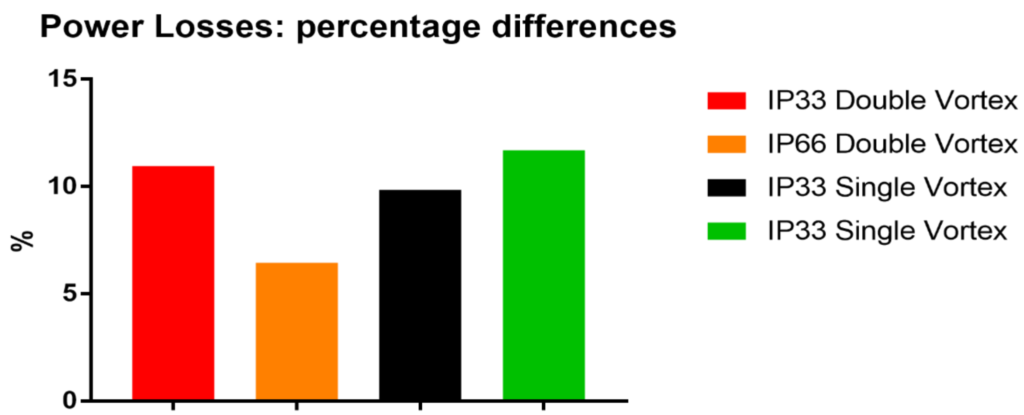

Figure 78 - Power losses: percentage differences respect to baseline profile

4.3.3 - *VISCOUS DISSIPATION RATE*

Figure 79 shows VDR during the cardiac cycle comparing the different velocity profile cases; the representation is in mWatt.

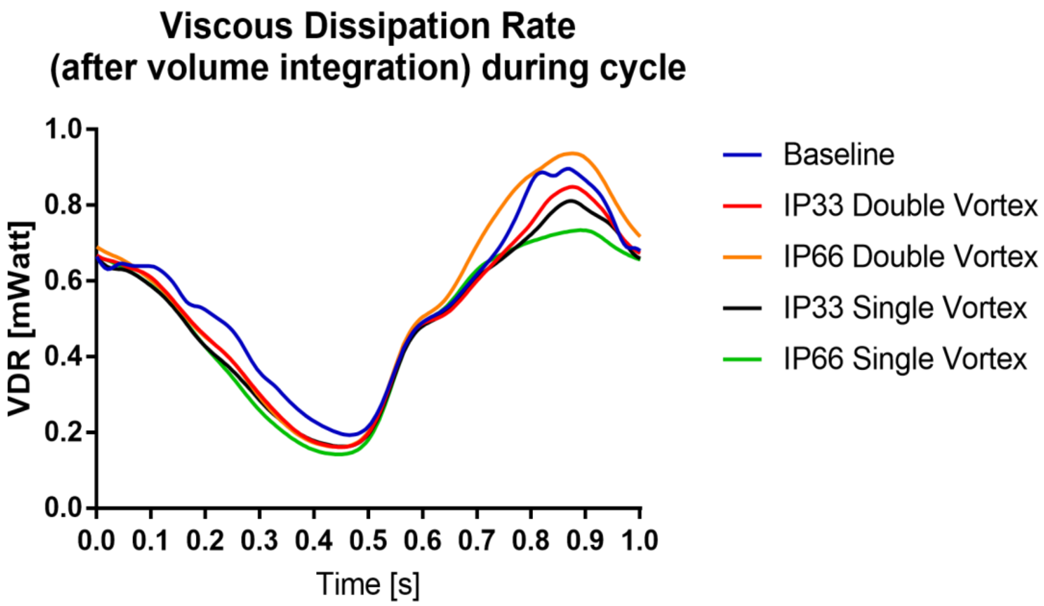

Figure 79 - VDR in time

At this point a final evaluation is done by volume integrated VDR time-averaging: in this way the comparison between the different cases is more immediate as it is possible to see in Figure 80. Even the relative standard deviations are calculated, and the representation is in milliWatt too.

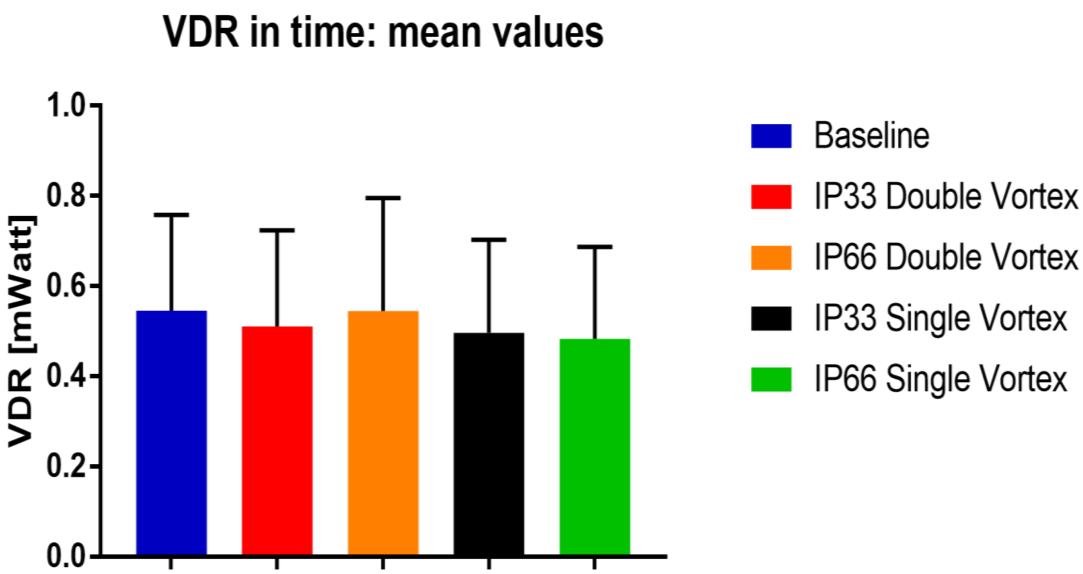

Figure 80 - Mean VDR and standard deviations

In order to see better the differences between VDR values, percentage differences computation respect to baseline was made and Figure 81 shows it. Comparing Figure 80 and Figure 81, we can understand that the greater is the percentage difference between baseline and another profile, the lower will be the energy dissipation of this velocity profile.

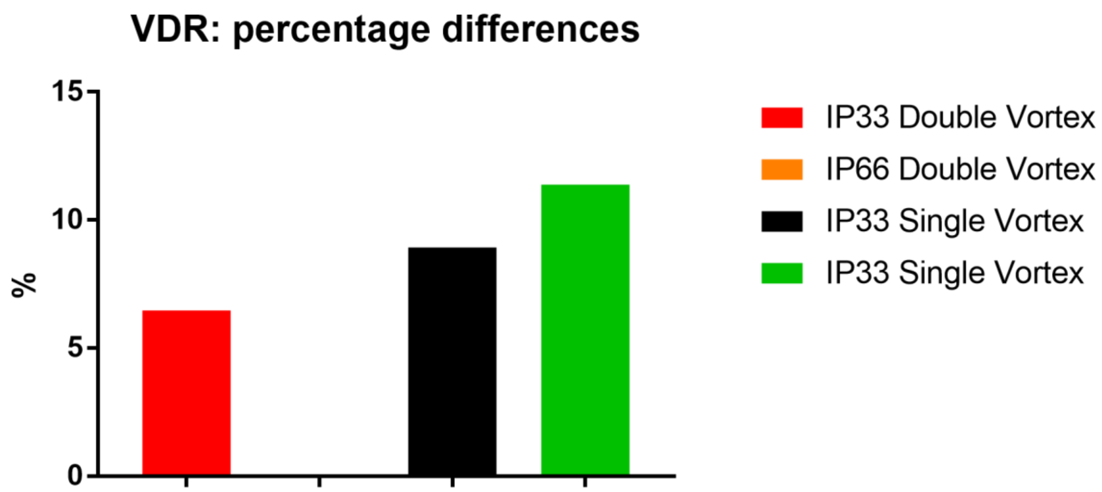

Figure 81 - VDR percentage differences respect to baseline profile

Thanks to a zoom visible in Figure 82 it is possible to observe in a better way the differences between of standard power losses and VDR in terms of energy dissipation.

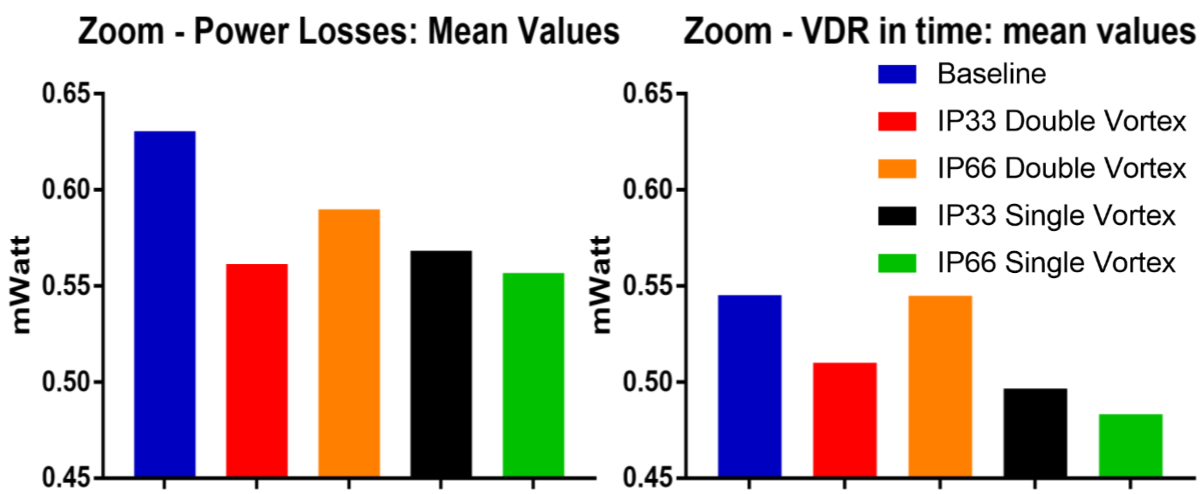

Figure 82 - Power losses and VDR mean values comparison

Here all the differences between these two methods are reported: VDR is a more predictable descriptor because of its punctual volumetric insight, while power losses base on more limiting assumptions focusing their study only on the inlets and outlets sections. Our results show that power losses overestimate the energy dissipation in all velocity patterns, as expected (Wei et al., 2018), because of the different theoretical analysis: power losses method requires more assumption and simplifications. They are statistically equivalent, but VDR has more reliable results because it is able to maintain a relationship between Fontan efficiency and patient outcomes (Wei et al., 2018). In any case, the profile with the lowest power losses and the lowest viscous dissipation rate is IP66 single vortex.

Chapter 5 – Conclusions

Fontan procedure is the most common surgical technique in univentricular heart cases. Its use is important because it allows to avoid the mixing of blood in the ventricle dividing the pulmonary and systemic circulations in a non-physiological way. Without this intervention, this pathological condition brings to death in the first year of patients' life. However, Fontan procedure has many aspects that must be improved in order to reduce the negative long terms outcomes that this alternative vessels' connection produces.

The final aim of this study is to understand what the impact of inlet velocity pattern on computational hemodynamics models of Fontan connection is, and, in particular, the effects of secondary flows on the efficiency of this treatment.

From the WSS-based descriptors analysis, it was observed that the presence of secondary flows reduced the area exposed to atherogenic risk and in particular the profiles with the highest percentage of in-plane velocity (IP66 double vortex and IP66 single vortex) show the lower risk areas and so can be seen as the less dangerous profiles because they have very few zones with low and oscillating WSS. Considering all the WSS-based descriptors, the baseline profile (without secondary flows) is the one which shows the highest values of area exposed to hemodynamic risk.

Energy dissipation was measured with two different indicators: power losses which consider only the hemodynamics at boundaries and viscous dissipation rate which takes into account the whole bulk flow hemodynamics. Both power losses and viscous dissipation rate identify the same best and worst profiles: IP66 single vortex and in general the two profiles with one vortex have the lowest dissipation values. This result can be explained by bulk flow descriptors: these profiles have high quantity of helical structures during the cardiac cycle and probably these flow patterns help to reduce hydraulic losses. On the contrary, baseline seems to have fewer helical structures than the other profiles with the conclusion that both power losses and VDR identify it as the worst case in energy dissipation.

At the end, it is possible to conclude that boundary conditions have a relevant impact on hemodynamics computation: different inlet velocity profiles have significant different results, maintaining all the simulation parameters and outlet conditions unchanged. Moreover, the profile without imposed secondary flows, the so-called baseline, that is normally used in Fontan studies and simulations, brings to an underestimation of this surgical treatment efficiency. So, the use of analytic in-plane component in inlet velocity profiles could be an interesting development in CFD in order to obtain more realistic results. This situation can be investigated in future works, comparing analytic profiles with *in vivo* measured ones using phase contrast magnetic resonance imaging.

The presence of imposed vortices at the inlets, as studied for other parts of the body (e.g. in arteriovenous access grafts), allows to generate a controlled amount of helical structures, which appear to play a beneficial role in terms of hydraulic losses, as well as the acknowledged atheroprotective role by means of suppression of stagnation regions.. Maybe a single vortex is preferable as inflow, but this conclusion needs more hemodynamic validations in future. From results analysis, it is possible to conclude that the presence of secondary flows in the Fontan connection is positive, from both atherogenic and efficiency points of view.

This study can be the first step into a wide discussion concerning the improvement of Fontan surgery and efficiency. However, it is necessary to do other verifications of our results or repeat this work on other patient-specific models, in order to do general conclusions that do not depend on specific geometry and conformation. Then, it will be possible to say if there is a velocity profile that have always the best haemodynamic and atherogenic results and how improve surgical strategy to impose it in real cases.

ACKNOWLEDGMENTS

Innanzitutto, vorrei ringraziare i professori Morbiducci e Gallo che mi hanno dato l'opportunità di lavorare a questo progetto di ricerca estremamente interessante e con importanti risvolti medici. Un enorme grazie va anche a Paola e Maurizio che ho stressato da un anno a questa parte, ma che sono sempre stati estremamente disponibili; hanno sempre avuto fiducia in me e nel mio lavoro e sono stati delle importanti guide durante tutto questo percorso di tesi.

Vorrei ringraziare poi la mia famiglia, che mi ha sostenuto in tutti questi anni di studio e che ha seguito con molto interesse tutti i progressi di questa tesi, incoraggiandomi nei momenti più complicati. Questo importante traguardo è dedicato a voi e ai nostri momenti difficili.

Ringrazio i miei compagni di percorso qui al Politecnico, in particolare Jovana, Chiara e Lorenzo che sono stati dei pilastri insostituibili in questi anni di studio matto e disperatissimo, e hanno reso il tutto un po' più bello.

Grazie anche alle mie bananas, le donne che mi conoscono meglio e da più tempo e che sono sempre state presenti in questi anni, nonostante le diverse università, le diverse città e i diversi impegni. Ognuna di voi mi ha aiutato ad arrivare fino a questo traguardo e sono sicura mi aiuterà anche in futuro. Grazie anche alle mie conoscenze più recenti: ai ragazzi del coro che mi hanno fatto sentire parte di un gruppo eterogeneo e inaspettato, ma sempre più coeso e nel quale ho scoperto dei veri amici; alle mie compagne di squadra che inconsapevolmente mi hanno aiutato a ritrovare quella serenità e quello svago che mi mancava da troppo tempo.

Infine, un grazie speciale va alla persona che mi è stata più vicina in questi due anni e mezzo non facili. Con la sua dolcezza e disponibilità mi ha reso una persona migliore, mi ha aiutato a credere maggiormente in me stessa e nelle mie capacità, nonostante la mia insicurezza e la mia ansia. È anche grazie a lui (e al suo pc!!) se sono arrivata alla fine di questo percorso senza scoraggiarmi quando gli intoppi mi sembravano insormontabili. Grazie di cuore Davide.

References

Anufriev, I. S., Krasinsky, D. V., Shadrin, E. Y., & Sharypov, O. V. (2014). Visualization of flow structure in a vortex furnace. *Technical Physics Letters*, *40*(10), 879–882. https://doi.org/10.1134/s1063785014100022

Boivin, S., Cayré, F., & Hérard, J.-M. (2000). A finite volume method to solve the Navier–Stokes equations for incompressible flows on unstructured meshes. *International Journal of Thermal Sciences*, *39*(8), 806–825. https://doi.org/10.1016/s1290-0729(00)00276-3

Bravo-valenzuela, N. J., Peixoto, A. B., & Araujo Júnior, E. (2018). Prenatal diagnosis of congenital heart disease: A review of current knowledge. *Indian Heart Journal*, *70*(1), 150–164. https://doi.org/10.1016/j.ihj.2017.12.005

Calabrò, R., Pacileo, G., & Russo, M. G. (2012). *Cardiopatie congenite II. Cardiologia*. Turin.

Children's Hospital Colorado. (n.d.). Single Ventricle Surgery. Retrieved from https://www.childrenscolorado.org/doctors-and-departments/departments/heart/programs-and-clinics/single-ventricle-clinic/single-ventricle-surgery/

Chugunova, M., Doyle, M. G., Keener, J. P., & Taranets, R. M. (2019). Use of mathematical modeling to study pressure regimes in normal and Fontan blood flow circulations. *Mathematics-in-Industry Case Studies*, *10*(1). https://doi.org/10.1186/s40929-019-0019-9

Corrosionpedia. (n.d.). Wall Shear Stress.

D'Andrea, C. (2013). *Cuore Univentricolare E Flusso Anterogrado : Outcome Dei Pazienti Sottoposti Ad Intervento Palliativo di Glenn Bidirezionale*.

Das, A., Gottliebson, W. M., Karve, M., Banerjee, R., A., D., W.M., G., … Banerjee, R. (2011). Comparison of hemodynamic endpoints between normal subject and tetralogy patient using Womersley velocity profile and MR based flow measurements. *Molecular & Cellular Biomechanics : MCB*, *8*(1), 21–42.

Dean, W. R. (1928). Fluid Motion in a Curved Channel. *Proceedings of the Royal Society A: Mathematical, Physical and Engineering Sciences*, *121*(787), 402–420. https://doi.org/10.1098/rspa.1928.0205

Dubini, G., De Leval, M. R., Pietrabissa, R., Montevecchi, F. M., & Fumero, R. (1996). A numerical fluid mechanical study of repaired congenital heart defects. Application to the total cavopulmonary connection. *Journal of Biomechanics*, *29*(1), 111–121. https://doi.org/10.1016/0021-9290(95)00021-6

Fontan F, B. E. (1971). Surgical repair of tricuspid atresia. *Thorax*, *26*(3), 240–248.

Frescura, C., & Thiene, G. (2014). The New Concept of Univentricular Heart. *Frontiers in Pediatrics*, *2*. https://doi.org/10.3389/fped.2014.00062

Gallo, D., Steinman, D. A., Bijari, P. B., & Morbiducci, U. (2012). Helical flow in carotid bifurcation as surrogate marker of exposure to disturbed shear. *Journal of Biomechanics*, *45*(14), 2398–2404. https://doi.org/10.1016/j.jbiomech.2012.07.007

Gatzoulis, M. A., Swan, L., Therrien, J., & Pantely, G. A. (2007). Ventricolo unico e circolazione tipo Fontan. In *Cardiopatie congenite dell'adulto* (pp. 122–134). Milan: Springer. https://doi.org/10.1007/978-88-470-0526-6_14

Girola, D. (2003). *Fisiologia applicata al fitness*.

Giunta, R. (2016). *Hydraulic Losses In Fontan Procedure For The Treatment Of The Univentricular Heart In Infants . A Numeric Study*. Polythecnic of Turin.

Glagov, S., Cozzi, P. J., Lyon, R. T., Davis, H. R., Ph, D., Sylora, J., & Zarins, C. K. (1988). susceptibility and resistance to experimental atherosclerosis I Proximal Aorta.

Grigioni, M, Daniele, C., Del Gaudio, C., Morbiducci, U., Balducci, a, D'Avenio, G., … Di Donato, R. (2003). Numerical simulation of a realistic total cavo-pulmonary connection: effect of unbalanced pulmonary resistances on hydrodynamic performance. *The International Journal of Artificial Organs*, *26*(11), 1005–1014.

Grigioni, Mauro, D'Avenio, G., Amodeo, A., & Di Donato, R. M. (2006). Power dissipation associated with surgical operations' hemodynamics: Critical issues and application to the total cavopulmonary connection. *Journal of Biomechanics*, *39*(9), 1583–1594. https://doi.org/10.1016/j.jbiomech.2006.04.008

Günther, T., Schulze, M., & Theisel, H. (2016). Rotation Invariant Vortices for Flow Visualization. *IEEE Transactions on Visualization and Computer Graphics*, *22*(1), 817–826. https://doi.org/10.1109/TVCG.2015.2467200

Günther, T., & Theisel, H. (2018). The State of the Art in Vortex Extraction. *Computer Graphics Forum*, *37*(6), 149–173. https://doi.org/10.1111/cgf.13319

Haggerty, C. M., Restrepo, M., Tang, E., De Zélicourt, D. A., Sundareswaran, K. S., Mirabella, L., … Yoganathan, A. P. (2014). Fontan hemodynamics from 100 patient-specific cardiac magnetic resonance studies: A computational fluid dynamics analysis. *Journal of Thoracic and Cardiovascular Surgery*, *148*(4), 1481–1489. https://doi.org/10.1016/j.jtcvs.2013.11.060

Himburg, H. A., Grzybowski, D. M., Hazel, A. L., LaMack, J. A., Li, X.-M., & Friedman, M. H. (2004). Spatial comparison between wall shear stress measures and porcine arterial endothelial permeability. *American Journal of Physiology-Heart and Circulatory Physiology*, *286*(5), H1916–H1922. https://doi.org/10.1152/ajpheart.00897.2003

Khiabani, R. H., Restrepo, M., Tang, E., De Zélicourt, D., Sotiropoulos, F., Fogel, M., & Yoganathan, A. P. (2012). Effect of flow pulsatility on modeling the hemodynamics in the total cavopulmonary connection. *Journal of Biomechanics*, *45*(14), 2376–2381. https://doi.org/10.1016/j.jbiomech.2012.07.010

Ku, D. N. (1985). Pulsatile flow and atherosclerosis in the human carotid bifurcation. Positive correlation between plaque location and low and oscillating shear stress. https://doi.org/O'Donnell, T. F. (1986). Pulsatile flow and atherosclerosis in the human carotid bifurcation: Positive correlation between plaque location and low and oscillating shear stress. Journal of Vascular Surgery, 3(6), 944. doi:10.1016/0741-5214(86)90448-9

Kuroczynski, W., Senft, D., Elsaesser, A., & Kampmann, C. (2014). Intra- or extracardiac Fontan operation? A simple strategy when to do what. *Archives of Medical Science*, *10*(4), 706–910. https://doi.org/10.5114/aoms.2013.33432

Laganà, K., Dubini, G., Migliavacca, F., Pietrabissa, R., Pennati, G., Veneziani, A., & Quarteroni, A. (2002). Multiscale modelling as a tool to prescribe realistic boundary conditions for the study of surgical procedures. *Biorheology*, *39*(3–4), 359–364.

Lardo, A. C., Webber, S. A., Friehs, I., Del Nido, P. J., & Cape, E. G. (1999). Fluid dynamic comparison of intra-atrial and extracardiac total cavopulmonary connections. *Journal of Thoracic and Cardiovascular Surgery*, *117*(4), 697–704. https://doi.org/10.1016/S0022-

5223(99)70289-8

Lee, S.-W., Antiga, L., & Steinman, D. A. (2009). Correlations Among Indicators of Disturbed Flow at the Normal Carotid Bifurcation. *Journal of Biomechanical Engineering*, *131*(6), 061013. https://doi.org/10.1115/1.3127252

Leefe, S. E., & Gentle, C. R. (1987). Theoretical evaluation of energy loss methods in the analysis of prosthetic heart valves. *Journal of Biomedical Engineering*, *9*(2), 121–127. https://doi.org/10.1016/0141-5425(87)90022-7

Lily's heart warriors. (n.d.). Single ventricle. Retrieved from https://lilysheartwarriors.weebly.com/single-ventricle.html

Liu, Y., Pekkan, K., Jones, S. C., & Yoganathan, A. P. (2004). The Effects of Different Mesh Generation Methods on Computational Fluid Dynamic Analysis and Power Loss Assessment in Total Cavopulmonary Connection. *Journal of Biomechanical Engineering*, *126*(5), 594. https://doi.org/10.1115/1.1800553

Malek, A. M., & Alper, S. L. (1999). Hemodynamic Shear Stress and Its Role in Atherosclerosis. *Stress: The International Journal on the Biology of Stress*, *282*(21), 2035–2042.

Migliavacca, F., Dubini, G., Bove, E. L., & de Leval, M. R. (2003). Computational fluid dynamics simulations in realistic 3-D geometries of the total cavopulmonary anastomosis: the influence of the inferior caval anastomosis. *Journal of Biomechanical Engineering*, *125*(6), 805–813. https://doi.org/10.1115/1.1632523

Migliavacca, F., Kilner, P. J., Pennati, G., Dubini, G., Pietrabissa, R., Fumero, R., & De Levai, M. R. (1999). Computational fluid dynamic and magnetic resonance analyses of flow distribution between the lungs after total cavopulmonary connection. *IEEE Transactions on Biomedical Engineering*, *46*(4), 393–399. https://doi.org/10.1109/10.752936

Moffatt, H. K., & Tsinober, A. (1992). Helicity in Laminar and Turbulent Flow. *Annual Review of Fluid Mechanics*, 281–312. https://doi.org/doi:10.1146/annurev.fl.24.010192.001433

Moore, J. E., Xu, C., Glagov, S., Zarins, C. K., & Ku, D. N. (1994). Fluid wall shear stress measurements in a model of the human abdominal aorta: oscillatory behavior and relationship to atherosclerosis. *Atherosclerosis*, *110*(2), 225–240. https://doi.org/10.1016/0021-9150(94)90207-0

Morbiducci, U. (2017a). *Flow Paradigm*. Turin.

Morbiducci, U. (2017b). HAEMODYNAMIC DESCRIPTORS. Turin.

Morbiducci, U. (2017c). *Il tessuto ematico ovvero della composizione del sangue*.

Morbiducci, U., Gallo, D., Massai, D., Consolo, F., Ponzini, R., Antiga, L., … Redaelli, A. (2010). Outflow Conditions for Image-Based Hemodynamic Models of the Carotid Bifurcation: Implications for Indicators of Abnormal Flow. *Journal of Biomechanical Engineering*, *132*(9), 091005. https://doi.org/10.1115/1.4001886

Morbiducci, U., Gallo, D., Massai, D., Ponzini, R., Deriu, M. A., Antiga, L., … Montevecchi, F. M. (2011). On the importance of blood rheology for bulk flow in hemodynamic models of the carotid bifurcation. *Journal of Biomechanics*, *44*(13), 2427–2438. https://doi.org/10.1016/j.jbiomech.2011.06.028

Morbiducci, U., Ponzini, R., Gallo, D., Bignardi, C., & Rizzo, G. (2013). Inflow boundary conditions for image-based computational hemodynamics: Impact of idealized versus measured velocity profiles in the human aorta. *Journal of Biomechanics*, *46*(1), 102–109. https://doi.org/10.1016/j.jbiomech.2012.10.012

Ohuchi, H. (2016). Adult patients with Fontan circulation: What we know and how to manage adults with Fontan circulation? *Journal of Cardiology*, *68*(3), 181–189. https://doi.org/10.1016/j.jjcc.2016.04.001

Pedersen, E. M., Agerbaek, M., Kristensen, I. B., & Yoganathan, A. P. (1997). Wall shear stress and early atherosclerotic lesions in the abdominal aorta in young adults. *European Journal of Vascular and Endovascular Surgery*, *13*(5), 443–451. https://doi.org/10.1016/S1078-5884(97)80171-2

Pekkan, K., Frakes, D., De Zelicourt, D., Lucas, C. W., Parks, W. J., & Yoganathan, A. P. (2005). Coupling pediatric ventricle assist devices to the Fontan circulation: Simulations with a lumped-parameter model. *ASAIO Journal*, *51*(5), 618–628. https://doi.org/10.1097/01.mat.0000176169.73987.0d

Pietrabissa, R., Jalali, H., Camporini a§, G., Redington b§, A., Migliavacca c§, F., de Leval, M. R., & Dubini, G. (1996). Use of computational fluid dynamics in the design of surgical procedures: Application to the study of competitive flows in cavopulmonary connections. *The Journal of Thoracic and Cardiovascular Surgery*, *111*(3), 502–513. https://doi.org/10.1016/s0022-5223(96)70302-1

Pinto, S. I. S., & Campos, J. B. L. M. (2016). Numerical study of wall shear stress-based descriptors in the human left coronary artery. *Computer Methods in Biomechanics and Biomedical Engineering*, *19*(13), 1443–1455. https://doi.org/10.1080/10255842.2016.1149575

Quarteroni, A., Ragni, S., & Veneziani, A. (2001). Coupling between lumped and distributed models for blood flow problems. *Computing and Visualization in Science*, *4*(2), 111–124. https://doi.org/10.1007/s007910100063

Rychik, J., & Cohen, M. I. (2002). Long-term outcome and complications of patients with single ventricle. *Progress in Pediatric Cardiology*, *16*(1), 89–103. https://doi.org/10.1016/S1058-9813(02)00047-4

Ryu, K., Healy, T. M., Ensley, A. E., Sharma, S., Lucas, C., & Yoganathan, A. P. (2001). Importance of accurate geometry in the study of the total cavopulmonary connection: Computational simulations and in vitro experiments. *Annals of Biomedical Engineering*, *29*(10), 844–853. https://doi.org/10.1114/1.1408930

Ryval, J., Straatman, A. G., & Steinman, D. A. (2004). Two-equation Turbulence Modeling of Pulsatile Flow in a Stenosed Tube. *Journal of Biomechanical Engineering*, *126*(5), 625. https://doi.org/10.1115/1.1798055

Scoville, H. (2019). Evolution of the human heart. Retrieved from https://www.thoughtco.com/evolution-of-the-human-heart-1224781

Shaaban, A. M., & Duerinckx, A. J. (2000). Wall Shear Stress and Early Atherosclerosis. *Review*, *174*(6), 1657–1665. https://doi.org/10.2214/ajr.174.6.1741657

Shah, M. J., Rychik, J., Fogel, M. A., Murphy, J. D., & Jacobs, M. L. (1997). Pulmonary AV malformations after superior cavopulmonary connection: Resolution after inclusion of hepatic veins in the pulmonary circulation. *Annals of Thoracic Surgery*, *63*(4), 960–963. https://doi.org/10.1016/S0003-4975(96)00961-7

SimVascular. (2017). SimVascular. Retrieved from http://simvascular.github.io

United Medical Education. (2012). The human heart. Retrieved from https://www.acls-pals-bls.com/the-human-heart/

University of California San Francisco. (2018). Norwood procedure. Retrieved from https://pediatricct.surgery.ucsf.edu/conditions--procedures/norwood-procedure.aspx

Wei, Z. A., Tree, M., Trusty, P. M., Wu, W., Singh-Gryzbon, S., & Yoganathan, A. (2018). The Advantages of Viscous Dissipation Rate over Simplified Power Loss as a Fontan Hemodynamic Metric. *Annals of Biomedical Engineering*, *46*(3), 404–416. https://doi.org/10.1007/s10439-017-1950-1

Whitehead, K. K., Pekkan, K., Kitajima, H. D., Paridon, S. M., Yoganathan, A. P., & Fogel, M. A. (2007). Nonlinear power loss during exercise in single-ventricle patients after the Fontan: Insights from computational fluid dynamics. *Circulation*, *116*(11 SUPPL. 1). https://doi.org/10.1161/CIRCULATIONAHA.106.680827

Womersley, R. J. (1955). Method for the calculation of velocity, rate of flow and viscous drag in arteries when the pressure gradient is known. *The Journal of Phisiology*, *2*(2), 553–563.

Yoganathan, A. P., Dasi, L. P., & Pekkan, K. (2012). NIH Public Access. *J Biomech*, *40*(6), 1301–1315. https://doi.org/10.1007/s10439-011-0452-9.Engineering